Semi-classical simulation of state-of-the-art toward-terahertz silicon-germanium heterojunction bipolar transistors

Von der Fakultät für Elektrotechnik und Informationstechnik der Rheinisch-Westfälischen Technischen Hochschule Aachen zur Erlangung des akademischen Grades eines Doktors der Ingenieurwissenschaften genehmigte Dissertation

vorgelegt von

Mohammad Hamed Kamrani

aus Tehran

Berichter: Universitätsprofessor Dr. Ing. Christoph Jungemann
Universitätsprofessor Dr. Ing. Vincenzo d'Alessandro

Tag der mündlichen Prüfung: 13.06.2017

Diese Dissertation ist auf den Internetseiten der Hochschulbibliothek online verfügbar.

Contents

Abstract vii

Acknowledgements ix

List of abbreviations xi

1 Introduction 1

1.1 SiGe HBT evolution 1

1.2 Fundamentals of SiGe HBT 2

1.3 The European DOTSEVEN project 4

1.4 TCAD and device simulation 5

2 Semi-classical Simulation Framework 7

2.1 The Boltzmann transport equation 7

2.2 Band structure 10

2.2.1 Band structure modeling for electrons and holes 11

2.2.2 Band edges 13

2.3 Scattering mechanisms 14

2.3.1 Phonon scattering 15
2.3.2 Ionized impurity scattering 17
2.3.3 Alloy scattering 19
2.3.4 Impact ionization 20
2.4 Shockley-Read-Hall recombination/generation 21
2.5 Band-to-band tunneling 24
2.6 Spherical harmonics expansion 25
2.6.1 Free-streaming operator 27
2.6.2 Scattering operator 27
2.6.3 Recombination/generation operator 28
2.7 H-transform 28
2.8 Coupled system of equations 29
2.9 Boundary condition 30
2.10 Discretization 30
2.11 I-V characteristics of SiGe HBTs 31

3 Electrothermal Effects **37**

3.1 Thermal issues in SiGe HBTs 37
3.2 Advanced electrothermal device simulation 38
3.3 BTEs for the coupled carrier-phonon system 41
3.3.1 Coupling term in carrier BTEs 42
3.3.2 BTE for LO phonons 43

3.4 Energy balance equations 46

3.5 Thermal conductivity 47

3.6 Temperature distribution 50

3.7 Effect of hot LO phonons 52

3.8 Thermal resistance extraction 52

3.8.1 V_{BE} temperature coefficient 53

3.8.2 V_{BE}- V_{CB} characteristic 54

3.9 Impact of self-heating 56

4 Hot Carrier Degradation **59**

4.1 HCD in bipolar transistors 59

4.2 Degradation modelling 62

4.2.1 Reaction-diffusion approach 64

4.2.2 Dispersive reaction-limited approach 65

4.3 Stress condition close to the SOA limit 66

4.3.1 Stress conditions and DC measurements 66

4.3.2 Distribution function based analysis 67

4.3.3 Degradation results based on a dispersive reaction-limited model 70

4.3.4 Degradation results based on a reaction-diffusion model . . . 73

4.4 Reverse EB bias stress condition 75

5 Summary and future work **81**

Bibliography 83

Abstract

This work presents a microscopic simulation and modeling framework for the state-of-the-art toward-terahertz silicon-germanium (SiGe) heterojunction bipolar transistors (HBTs). To this goal, a stationary deterministic solver based on a spherical harmonics expansion of the coupled system of Boltzmann transport equations for electrons, holes, and phonons has been developed. The simulation results of this in-house deterministic solver, which includes full band structure and high-field effects, are verified against experimental data. To investigate non-equilibrium effects for the carrier-phonon system, the impact of hot longitudinal optical phonons on steady state carrier transport is discussed. Furthermore, the self-consistent and deterministic solution of the coupled set of equations allows to extract the junction temperature by making use of a method based on the simulated DC characteristics. The resultant junction temperature is compared to the value obtained from the temperature profile within the nanoscale device. Good agreement is obtained for the average temperature in the base-emitter junction verifying the analytical approach used to extract the thermal resistance of the device by experiments. In order to obtain a new insight into the underlying mechanisms of hot-carrier degradation in bipolar transistors, a physics-based model based on the distribution functions of both hot electrons and hot holes is introduced. The full-band transport model provides the energy distribution functions of the charge carriers interacting with the passivated Si-H bonds along the oxide interface. The simulation results assert the dominant role of hot holes along the emitter-base spacer oxide interface in the long-term degradation of an npn SiGe HBT under low and high-current conditions at the border of the safe operating area. The interface trap density, which is calculated

by incorporating a reaction-limited model with dispersive reaction rates, explains the time dependence of the interface trap density and the resulting forward-mode leakage base current for different stress bias conditions.

Acknowledgements

I would like to express my gratitude to all the people who ever gave me help and support during my PhD study period. Particularly, I would like to thank my research advisor Prof. Christoph Jungemann for his continual instruction and encouragements. I would also like to thank my colleague and friend Dominic Jabs who his support during these years was invaluable. I am grateful for the support of the European Community's Seventh Framework Programme (DOTSEVEN). I was fortunate enough to be involved in this great and international research project and have the chance to collaborate with outstanding researchers involved in this project. A special thank is to Prof. Vincenzo d'Alessandro for his unsparing assistances in this project. I am also very grateful to my parents who always supported me throughout my life. Finally, the greatest thank is for my wife, Nina, for her unwavering love and patience. She is my best friend and companion whose understanding and encouragements helped me get through this agonizing period in the most positive way.

Hamed Kamrani

List of abbreviations

AB	antibonding
AI	acceleration integral
BJT	bipolar junction transistor
BTBT	band-to-band tunneling
BTE	Boltzmann transport equation
CB	collector-base
DD	drift-diffusion
DTI	deep trench isolation
EB	emitter-base
EDF	energy distribution function
HBT	heterojunction bipolar transistor
HCD	hot-carrier degradation
HD	hydrodynamic
HH	heavy hole
II	impact ionization
LH	light hole

LO longitudinal optical

MC Monte Carlo

MM mixed-mode

MOSFET metal-oxide-semiconductor field-effect transistor

MVE multiple vibrational excitation

RSi relaxed silicon

SCR space-charge-region

SHE spherical harmonics expansion

SiGe silicon-germanium

SO split-off

SOA safe operating area

SRH Shockley-Read-Hall

STI shallow trench isolation

TAT trap-assisted-tunneling

TCAD technology computer-aided design

Chapter 1

Introduction

1.1 SiGe HBT evolution

The invention of the bipolar junction transistor (BJT) at the Bell laboratories started the solid-state electronics era in 1948. However, in the seventies, the spectacular rise of the metal-oxide-semiconductor field-effect transistors (MOSFETs) removed BJTs from the center of attentions. The desirable properties of MOSFETs allowed them to capture the main market share of semiconductor transistors, specially for all logic circuits, memory and microprocessor chips. Nevertheless, because of superior qualities in terms of high speed, high current density and greater transconductance compared to the MOSFETs, BJTs remained important devices for high-speed design applications and power amplifiers.

To keep competing with MOSFET technologies, a number of trade-offs between contradictory features of bipolar transistors are required. In order to achieve a high value of cut-off frequency, the base width should be as small as possible, whereas decreasing this width has to be stopped, when the emitter-base (EB) space-charge-region (SCR) begins to overlap the collector-base (CB) SCR. Hence, a thinner base width is possible via increasing the doping concentration of the base region with the cost of a reduction in the transistor gain. This compromise between current

gain and the transit time of charge carriers in the base region is the main limiting factor, which determines the maximum achievable cut-off frequency (50 GHz) of a silicon bipolar transistor [1].

The inauguration of silicon-germanium (SiGe) heterojunction bipolar transistor (HBT) in the late eighties [2], as the first successful experience of band gap engineering in silicon, provided an additional degree of freedom leading to vastly improved devices compared to the silicon BJT counterparts. In these transistors, germanium, which has a smaller band gap than silicon, is used in the base region to obtain a reasonable value of current gain with high base doping and reduced base width. As a result, much higher values of cut-off frequency can be achieved with SiGe HBTs. In 2010 and in the framework of the European DOTFIVE project, IHP reported a maximum oscillation frequency, $f_{\max}$, of 500 GHz and a cut-off frequency f_T as high as 350 GHz [3], which was considered as the highest speed SiGe HBT by that time. However, technology computer-aided design (TCAD) simulations show the possibility of designing extremely low noise SiGe HBTs with peak cut-off and maximum oscillation frequencies above 1THz [4]. In recent years, SiGe HBTs are mostly offered commercially in SiGe BiCMOS technology, which combines SiGe bipolar and CMOS transistors in a single integrated circuit. This low cost technology, which benefits from advantages of modern SiGe HBTs, is widely used for high-frequency applications, such as high-speed communication, radar, and THz imaging [5].

1.2 Fundamentals of SiGe HBT

An npn SiGe HBT is made of a heavily n-doped emitter, a p-doped base, and an n-doped collector. In order to reduce the band gap in the base compared to the emitter, a Ge profile is introduced in the base region. The forward-mode device operation refers to the EB junction, which is forward biased ($V_{\mathrm{BE}} > 0$), while the CB junction is reverse biased ($V_{\mathrm{CB}} > 0$). To better understand how a bipolar transistor operates and the corresponding parameters are defined, we consider the energy band diagram of an ideal SiGe HBT with constant doping and graded Ge profiles,

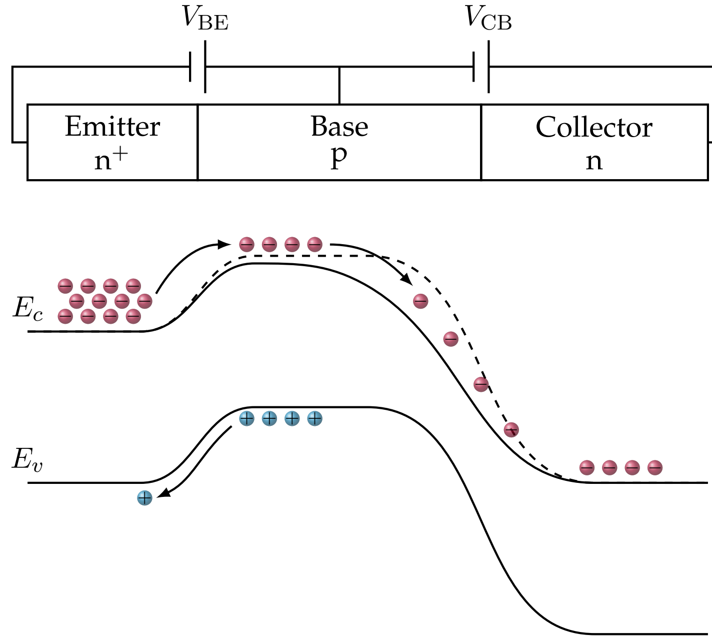

Figure 1.1: Schematic of a forward-biased SiGe HBT and the corresponding band energy diagram. The dashed line shows the conduction band of a Si BJT counterpart.

which is shown in Fig 1.1. With an external forward bias applied over the EB junction, the potential barrier between emitter and base is reduced and electrons are injected from the emitter into the base. Likewise, holes diffuse from base into the emitter. The injected electrons into the base region diffuse towards the CB junction, where they are accelerated in the direction of the collector due to relatively large electric field associated with the reverse bias at the CB junction.

In the forward biased EB junction, electric field is relatively small and the current is determined by the diffusion of carriers. The collector current in the case of constant doping profiles can be expressed as [6]

$$I_C = q_e A_E \frac{D_{nB} n_{iB}^2}{W_B N_B} \left(e^{\frac{q_e V_{\mathrm{BE}}}{k_B T}} - 1\right), \tag{1.1}$$

where q_e is the electron charge, A_E is the emitter area, D_{nB} is the diffusion coefficient of electrons in the base, n_{iB} is the intrinsic carrier concentration in the base, W_B is the base width, N_B is the doping concentration in the base, k_B is the Boltz-

mann constant, and T is the homogenous temperature. In a similar approach, the base current is given by [6]

$$I_B = q_e A_E \frac{D_{pE} n_{iE}^2}{W_E N_E} \left(e^{\frac{q_e V_{\mathrm{BE}}}{k_B T}} - 1\right), \tag{1.2}$$

where D_{pE} is the diffusion coefficient of holes in the emitter, n_{iE} is the intrinsic carrier concentration in the emitter, W_E is the emitter width, and N_E is the doping concentration in the emitter. At the first glance, it might be concluded that these currents would decrease by increasing temperature, but this overlooks the critical role of the intrinsic carrier concentration, which is enhanced with increasing temperature. The increment of the collector current by temperature, which is translated to higher dissipated power and, in turn, to further temperature increase, is known as the positive electrothermal feedback in bipolar transistors [7].

Introduction of Ge content into the base leading to a reduction in the potential energy barrier of the conduction band (Fig 1.1) yields exponentially more electron injection from emitter into the base. Furthermore, a narrower band gap in the base results in a higher intrinsic carrier density, which increases the collector current (Eq. 1.1), whereas it has almost no effect on the base current (Eq. 1.2). On the other hand, it is desired to sweep all of the injected electrons into the collector. However, a small percentage of electrons flowing through the EB junction can recombine with holes, which means more holes have to be supplied from the base terminal. This recombination effect has almost no impact on the collector current, while it increases the base current. Therefore, the current gain, which is given by $\beta = I_C/I_B$, is increased by adding Ge content and reduced by increasing the recombination effects in the base.

1.3 The European DOTSEVEN project

DOTSEVEN was a very ambitious 3.5-year research and development project with the aim of developing SiGe HBT technology, modeling, circuits and systems with maximum oscillation frequencies up to 0.7 THz. Following a successful research

cooperation in the DOTFIVE, which produced the first half-THz SiGe HBTs, the DOTSEVEN project was launched late 2012 by the European Commission. The manufacturability and integration with CMOS as well as the capabilities and benefits of SiGe HBTs with $f_T/f_{\max}$ of 505 GHz/720 GHz were successfully demonstrated during this project [8].

However, a state-of-the-art SiGe HBT suffers from thermal issues and hot-carrier degradation (HCD), which limit safe operating area (SOA) and reliability of these devices. To assist technology development, a reliable physics-based device simulation platform is required to obtain a deep insight into these phenomena in extremely scaled devices. Hence, in the work package #2 of the DOTSEVEN project, advanced simulation tools were provided to support compact modeling and process development.

1.4 TCAD and device simulation

TCAD simulation and modeling can be used to investigate the device performance, to identify operating limits and to predict the behavior of the next-generation devices. These capabilities can significantly reduce the time and cost of technology development. In order to simulate SiGe HBTs, the classical TCAD tools like the drift-diffusion (DD) or the hydrodynamic (HD) models are widely used. However, as the device size approaches the nanometer range, transport can be no longer described accurately by the DD or HD models, which fail even in the linear regime and cannot capture hot-carrier and hot-phonon effects [9]. Therefore, the semi-classical Boltzmann transport equations (BTEs), which consider together both real space and momentum space aspects of charge and thermal transport, have to be solved.

To date, stochastic algorithms, such as the Monte Carlo (MC) method, were mostly applied for the solution of the BTEs in semiconductor devices. These methods involve the simulation of the particle trajectories rather than the direct solution of partial differential equations and have many disadvantages compared to the non-

stochastic solvers [10]. Instead, a direct solution of the BTE based on the spherical harmonics expansion (SHE) method has been pursued for several decades and urged recently a renewed interest in numerical solutions of the BTE due to more powerful computational platforms, which are available.

This thesis work offers a stationary deterministic solver based on a SHE for a coupled system of BTEs for electrons and holes, which is used for device simulation of SiGe HBTs and investigating electrothermal effects and HCD in these devices. This in-house simulation tool has been experimentally verified, enabling the efficient support of the technology development with accurate predictions in the framework of the DOTSEVEN project.

In chapter 2 of this thesis, a coupled system of BTEs for electron and holes and its solution based on the SHE method will be described. This deterministic solver includes full band structure effects, carrier-phonon scattering, impurity scattering, alloy scattering, impact ionization (II), Shockley-Read-Hall (SRH) recombination and band-to-band tunneling (BTBT), the simulation results of which are verified against experimental data. In chapter3, a deterministic and self-consistent solution of a coupled carrier-phonon system is presented to study self-heating in ultra-scaled bipolar transistors. In Chapter 4, a physics-based model is presented and validated to describe the underlying mechanisms of hot-carrier degradation in bipolar transistors.

Chapter 2

Semi-classical Simulation Framework

This chapter is devoted to describe a coupled system of BTEs for electrons and holes with including full band structure effects, which is solved based on the SHE method. The results of the deterministic solver are used to investigate electrical characteristics of state-of-the-art SiGe HBTs.

2.1 The Boltzmann transport equation

In a classical approach, dynamics of a single electron with a particular position $\vec{r}(t)$ and momentum $\vec{p}(t)$ at time t are described by the Newton's laws of motion

$$\frac{d\vec{r}}{dt} = \vec{v}, \qquad \frac{d\vec{p}}{dt} = \vec{F}, \tag{2.1}$$

where $\vec{F} = -e\vec{E}$ is the force acting on the electron, e is the elementary charge, and $\vec{E}$ is the effective electric field. In semiconductors, motion of charge carriers is influenced by the interactions with the crystal lattice potential. The analysis of periodic potentials in a lattice based on quantum mechanics leads to energy bands,

which specify the energies that charge carriers can achieve. The energy of a carrier $\varepsilon(\vec{k})$ in a specific energy band is related to the wave vector $\vec{k}$ of the carrier, and the corresponding carrier group velocity is given by [11]

$$\vec{v}(\vec{k}) = \frac{1}{\hbar}\nabla_k \varepsilon(\vec{k}), \tag{2.2}$$

where $\hbar$ is the reduced Planck constant. The energy bands are material properties and can be obtained from sophisticated numerical simulations, which are discussed in more detail for SiGe in Sec. 2.2.

In order to account for a large number of particles, we consider the distribution function $f(\vec{r}, \vec{k}, t)$ that $2/(2\pi)^3 f(\vec{r}, \vec{k}, t)d^3rd^3k$ gives the number of carriers at a certain time in the phase space volume d^3rd^3k, in which the prefactor $2/(2\pi)^3$ accounts for the spin degeneracy and the minimum phase space volume. The distribution function would tell us how charge carriers are distributed in k-space (or energy-space) at fixed position and time, and from this information all of the transport properties can be evaluated. For example, the electron density can be calculated by an integration over the first Brillouin zone (BZ) and summing over all conduction bands [12]

$$n(\vec{r}, t) = \frac{2}{(2\pi)^3} \sum_C \int_{\text{BZ}} f^C(\vec{r}, \vec{k}, t) d^3k, \tag{2.3}$$

whereas the hole density is obtained by this summation over the valence bands

$$p(\vec{r}, t) = \frac{2}{(2\pi)^3} \sum_V \int_{\text{BZ}} f^V(\vec{r}, \vec{k}, t) d^3k. \tag{2.4}$$

The carrier distribution function can change over time in k-space and r-space due to diffusion, drift and collision. Therefore, the time evolution of the distribution function is written as [13]

$$\frac{\partial f}{\partial t} = \left(\frac{\partial f}{\partial t}\right)_{\text{diffusion}} + \left(\frac{\partial f}{\partial t}\right)_{\text{drift}} + \left(\frac{\partial f}{\partial t}\right)_{\text{collision}}. \tag{2.5}$$

Diffusion is caused by any gradient in the carrier concentration. At a fixed state $\vec{k}$, flow of carriers at time t from $\vec{r}$ to $\vec{r} + dt\vec{v}$ does not change the number of carriers in the new phase space volume at time $t + dt$, i.e. $f(\vec{r}, \vec{k}, t) = f(\vec{r} + dt\vec{v}, \vec{k}, t + dt)$.

Hence, we can write

$$f(\vec{r},\vec{k},t) = f(\vec{r},\vec{k},t) + dt\vec{v}(\vec{k}) \cdot \frac{\partial f}{\partial \vec{r}} + dt\frac{\partial f}{\partial t}. \tag{2.6}$$

As a result, the change of the distribution function due to motion of carriers can be given by

$$\left(\frac{\partial f}{\partial t}\right)_{\text{diffusion}} = -\vec{v}(\vec{k}) \cdot \frac{\partial f}{\partial \vec{r}}. \tag{2.7}$$

Likewise at a fixed position $\vec{r}$, under the influence of the electric field, the wave vector of the carrier at time t can evolve from $\vec{k}$ to $\vec{k} + dt\partial\vec{k}/\partial t$ at time $t + dt$. The continuity of the distribution function $f(\vec{r},\vec{k},t) = f(\vec{r},\vec{k} + dt\partial\vec{k}/\partial t, t + dt)$ can be written as

$$f(\vec{r},\vec{k},t) = f(\vec{r},\vec{k},t) + dt\frac{\partial \vec{k}}{\partial t} \cdot \frac{\partial f}{\partial \vec{k}} + dt\frac{\partial f}{\partial t}, \tag{2.8}$$

which leads to

$$\left(\frac{\partial f}{\partial t}\right)_{\text{drift}} = -\frac{\partial \vec{k}}{\partial t} \cdot \frac{\partial f}{\partial \vec{k}} = -\frac{1}{\hbar}\vec{F} \cdot \frac{\partial f}{\partial \vec{k}}. \tag{2.9}$$

The collision term models the microscopic scattering mechanisms present in the system. We assume that the scattering processes are local and instantaneous, which change the state of the carrier from $\vec{k}$ to $\vec{k}'$ with the transition rate $W(\vec{r},\vec{k}|\vec{k}')$. The rate of change in the distribution function due to scattering is written as [13]

$$\begin{aligned}\left(\frac{\partial f}{\partial t}\right)_{\text{collisions}} = \frac{V_0}{(2\pi)^3} \int_{\text{BZ}} \Big[&\big(1 - f(\vec{r},\vec{k},t)\big) W(\vec{r},\vec{k}|\vec{k}') f(\vec{r},\vec{k}',t) \\ &- \big(1 - f(\vec{r},\vec{k}',t)\big) W(\vec{r},\vec{k}'|\vec{k}) f(\vec{r},\vec{k},t) \Big] d^3k',\end{aligned} \tag{2.10}$$

where V_0 is the system volume, the first term in the integral represents the in-scattering rate at which carriers scatter from an occupied state with the occupation probability $f(\vec{r},\vec{k}',t)$ into an unoccupied state with the probability of $1 - f(\vec{r},\vec{k},t)$, and the second term denotes the corresponding out-scattering rate.

In addition to scattering mechanisms, which can change the distribution function (described in Sec. 2.3), recombination/generation of carriers (Sec. 2.4) and BTBT (Sec. 2.5) can also affect the distribution function. Thus, the final form of the BTE

reads

$$\frac{\partial f}{\partial t} + \vec{v}(\vec{k}) \cdot \frac{\partial f}{\partial \vec{r}} + \frac{1}{\hbar}\vec{F}(\vec{r}) \cdot \frac{\partial f}{\partial \vec{k}} = \frac{V_0}{(2\pi)^3} \int_{\mathrm{BZ}} \Big[\big(1 - f(\vec{r},\vec{k},t)\big) W(\vec{r},\vec{k}|\vec{k}') f(\vec{r},\vec{k}',t) - \big(1 - f(\vec{r},\vec{k}',t)\big) W(\vec{r},\vec{k}'|\vec{k}) f(\vec{r},\vec{k},t)\Big] d^3k' - \Gamma\{f^e, f^h\} + G_{\mathrm{BTBT}}\{n,p\} \tag{2.11}$$

In this thesis work, we consider the stationary solution of the BTE; therefore, the time derivative and time-dependence of the distribution function are neglected.

2.2 Band structure

Discrete energy levels of the atoms, which construct a semiconductor lattice, form near-continuum levels called band energies. The electronic properties of a semiconductor are determined by the highest partially empty band (conduction band) and the lowest partially filled band (valence band). Therefore, only these bands are considered to describe the band structure of a semiconductor. The unoccupied states in the valence band, known as holes, can also accept a new electron, which provide another mechanism for electrons to move and contribute to the current conduction. Hence, to simplify the calculations for the electronic transitions in the almost filled valence band, the concept of holes as positive charge carriers has been introduced.

The electronic band structure of a Si or SiGe, which describes the variation of the kinetic energy with respect to the wave-vector, is commonly calculated with the nonlocal empirical pseudopotential method [14, 15]. However, direct inclusion of the full-band structure into the SHE simulator is practically impossible. Hence, in Sec. 2.2.1, we explain a valley model for the conduction band and a summation model for the valence band, which are used to include full-band effects in our SHE solver.

2.2.1 Band structure modeling for electrons and holes

The band structure close to the conduction band edge can be approximated by ellipsoidal energy surfaces. In the analytical Modena model [16], the conduction band is described by six non-parabolic valleys, in which dispersion relation is given by

$$\varepsilon(1+\alpha_n\varepsilon) = \frac{\hbar^2}{2m_{xx}}k_x'^2 + \frac{\hbar^2}{2m_{yy}}k_y'^2 + \frac{\hbar^2}{2m_{zz}}k_z'^2 \tag{2.12}$$

where α_n is the non-parabolicity factor, and m_{xx}, m_{yy}, and m_{zz} are the effective masses along each direction. In order to simplify SHE of the BTE [17], the elliptical valleys are mapped onto spherical ones by the Herring-Vogt transform [18]

$$\hat{T}^v = \begin{bmatrix} \left(\frac{m_d^v}{m_{xx}^v}\right)^{1/2} & 0 & 0 \\ 0 & \left(\frac{m_d^v}{m_{yy}^v}\right)^{1/2} & 0 \\ 0 & 0 & \left(\frac{m_d^v}{m_{zz}^v}\right)^{1/2} \end{bmatrix} \tag{2.13}$$

where $m_d^v = \left(m_{xx}^v m_{yy}^v m_{zz}^v\right)^{1/3}$ is the density of states effective mass. The wave vector in the Herring-Vogt transformed momentum space is obtained from

$$\vec{k}^v = \hat{T}^v \vec{k}'^v \tag{2.14}$$

where k'^v is the wave vector in the original space. As a consequence, the dispersion relation becomes isotropic

$$\varepsilon(1+\alpha_n\varepsilon) = \frac{\hbar^2 k^2}{2m_d} \tag{2.15}$$

Despite simplicity of this approach, it provides a reasonable approximation only up to an energy of about 1 eV, while charge carriers gain energies up to 4 eV under stress conditions [19]. Thus, to incorporate full-band effects within the framework of the SHE method, we assume an isotropic band structure in the Herring-Vogt transformed momentum space and extract the two first energy-dependent moments of the dispersion relation corresponding to the density of states [15]

$$Z^v(\varepsilon) = \frac{1}{(2\pi)^3}\int_{\mathrm{BZ}} \delta\left[\varepsilon - \varepsilon^v(\vec{k})\right] d^3k \tag{2.16}$$

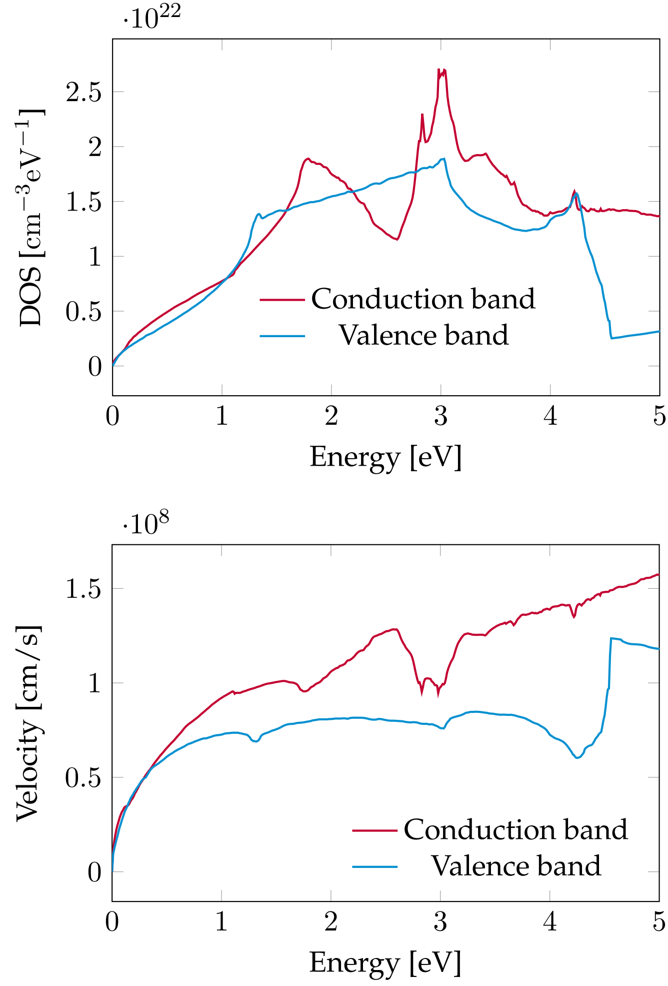

Figure 2.1: The total density of states and group velocity for relaxed silicon in conduction and valence bands.

and the average group velocity

$$v^v(\varepsilon) = \left(\frac{1}{(2\pi)^3} \frac{1}{Z^v(\varepsilon)} \int_{\mathrm{BZ}} \delta\big[\varepsilon - \varepsilon^v(\vec{k})\big] \big|\vec{v}(\vec{k})\big|^2 d^3k \right)^{\frac{1}{2}}, \tag{2.17}$$

from the full-band structure. Fig. 2.1 shows the density of states and group velocity of the conduction and valence bands in relaxed silicon obtained from the empirical pseudopotential method [15].

To consider the anisotropic nature of the conduction band, we adopt a six-valley

model, which consists of three different pairs of valleys in x-,y-, and z-directions and apply the Herring-Vogt transformation [20]. This separation of valleys gives further the possibility of including the impact of Ge content in a simple manner.

For the valence band, we have to consider two degenerate bands, heavy hole (HH) and light hole (LH), and the split-off (SO) band, which is very close to them. Therefore, we consider a summation of the density of states in these three bands and a weighted average of the group velocity given by [12]

$$v_{\mathrm{val}}(\varepsilon) = \frac{v_{\mathrm{HH}}(\varepsilon)Z_{\mathrm{HH}}(\varepsilon) + v_{\mathrm{LH}}(\varepsilon)Z_{\mathrm{LH}}(\varepsilon) + v_{\mathrm{SO}}(\varepsilon)Z_{\mathrm{SO}}(\varepsilon)}{Z_{\mathrm{HH}}(\varepsilon) + Z_{\mathrm{LH}}(\varepsilon) + Z_{\mathrm{SO}}(\varepsilon)}. \tag{2.18}$$

In our nomenclature, v denote the valley indices for the conduction band, which is 1 to 6, while for the valence band it refers to band indices, which is 1, because we consider one single band, which is the summation of all three bands as one single band.

2.2.2 Band edges

In a semiconductor device, the conduction band minimum, E_c, and the valence band maximum, E_v, are shifted due to doping and Ge content; consequently, these band edges are position-dependent. The band shifts due to Ge content $x_{\mathrm{Ge}}(\vec{r})$ in a $\mathrm{Si}_{1-x}\mathrm{Ge}_x$ alloy relative to relaxed Si for the conduction and valence bands, are given by [21]

$$\Delta E_c^{\mathrm{Ge}}(\vec{r}) = -0.196\mathrm{eV}\, x_{\mathrm{Ge}}(\vec{r}) + 0.396\mathrm{eV}\, x_{\mathrm{Ge}}^2(\vec{r}) \tag{2.19}$$

$$\Delta E_v^{\mathrm{Ge}}(\vec{r}) = 0.7\mathrm{eV}\, x_{\mathrm{Ge}}(\vec{r}). \tag{2.20}$$

Furthermore, $\mathrm{Si}_{1-x}\mathrm{Ge}_x$ grown on a relaxed Si substrate is stressed. This effect adds an extra energy shift to the two out-of-plane valleys, which is modeled by

$$E_{c,v=1}^{\mathrm{Ge}}(\vec{r}) - E_{c,v=2,3}^{\mathrm{Ge}}(\vec{r}) = 0.63\mathrm{eV}\, x_{\mathrm{Ge}}(\vec{r}). \tag{2.21}$$

The apparent bandgap narrowing due to doping has been shown to be similar in n-type and p-type silicon and is given by an empirical model [22]

$$\Delta E^{\mathrm{BGN}}(\vec{r}) = E_0\left(\ln\frac{N_a(\vec{r})+N_d(\vec{r})}{N_{\mathrm{Ref}}} + \sqrt{\left(\ln\frac{N_a(\vec{r})+N_d(\vec{r})}{N_{\mathrm{Ref}}}\right)^2 + 0.5}\right), \tag{2.22}$$

where $N_a(\vec{r})$ and $N_d(\vec{r})$ are the position dependent acceptor and donor concentrations, respectively, $E_0 = 6.92\,\mathrm{meV}$ and $N_{\mathrm{Ref}} = 1.3\times10^{17}\mathrm{cm}^{-3}$. The same parameters are used to account for bandgap narrowing due to doping in SiGe alloy [23]. The total band energy shifts are expressed as

$$E_c(\vec{r}) = \Delta E_c^{\mathrm{Ge}}(\vec{r}) - \frac{1}{2}\Delta E^{\mathrm{BGN}}(\vec{r}), \tag{2.23}$$

$$E_v(\vec{r}) = -E_{g0}(\vec{r}) + \Delta E_v^{\mathrm{Ge}}(\vec{r}) + \frac{1}{2}\Delta E^{\mathrm{BGN}}(\vec{r}), \tag{2.24}$$

where $E_{g0}(\vec{r})$ is the band-gap of the intrinsic Si, which is temperature dependent and given by

$$\frac{E_{g0}(\vec{r})}{1\mathrm{eV}} = \begin{cases} 1.1785 - 9.025\times10^{-5}\frac{T_L(\vec{r})}{\mathrm{K}} - 3.05\times10^{-7}\frac{T_L^2(\vec{r})}{\mathrm{K}^2} & : \ 190\mathrm{K} \le T_L(\vec{r}) < 275\mathrm{K} \\ 1.206 - 2.730\times10^{-4}\frac{T_L(\vec{r})}{\mathrm{K}} & : \ 275\mathrm{K} \le T_L(\vec{r}) \end{cases} \tag{2.25}$$

in which $T_L(\vec{r})$ is the lattice temperature.

2.3 Scattering mechanisms

Charge carriers are scattered by various mechanisms in a semiconductor device [24]. They can be scattered by phonons 2.3.1, ionized impurities 2.3.2, alloy disorder in composites 2.3.3, and II 2.3.4. Based on the assumption that scattering events occur instantaneously and only change the wave-vector of the scattered carriers, they are characterized by their respective transition rates calculated with the Fermi's golden rule as [11]

$$W^{v',v}(\vec{r},\vec{k}'|\vec{k}) = \frac{2\pi}{\hbar}\left|M^{v',v}(\vec{r},\vec{k}'|\vec{k})\right|^2\delta\left[\varepsilon^{v'}(\vec{k}') - \varepsilon^{v}(\vec{k}) - \varepsilon^{t}(\vec{k}'|\vec{k})\right], \tag{2.26}$$

	Si	Ge
ρ [g/cm^3]	2.33	5.32
u_l [cm/s]	9.05×10^5	5.40×10^5
κ/κ_0	11.7	16.0
Ξ_e [eV]	8.90	8.79
Ξ_h [eV]	5.12	7.40
a_0 [Å]	5.43	5.66
c_{11} [Mbar]	1.657	1.285
c_{12} [Mbar]	0.639	0.482

Table 2.1: Material parameters for silicon and germanium

where $M^{v',v}(\vec{r},\vec{k}'|\vec{k})$ is the matrix element of the interaction and $\varepsilon^t(\vec{k}'|\vec{k})$ is the transferred energy between two states. Since these transition rates in the general form are very complex, simplified models, which still satisfy fundamental experiments, are used to perform CPU efficient simulations. The scattering rate is calculated as

$$S^v(\vec{r},\vec{k}) = \frac{V_0}{(2\pi)^3}\sum_{v'}\int_{\mathrm{BZ}} W^{v',v}(\vec{r},\vec{k}'|\vec{k})d^3k', \tag{2.27}$$

which is the probability that one carrier scatters via a specific scattering mechanism.

2.3.1 Phonon scattering

The constructing atoms of a crystal lattice vibrate around their fixed equilibrium locations at non-zero temperatures. This vibrational motion can be quantized and phonons are the quasiparticles attributed to the different modes of lattice vibrations. The coherent movements of atoms out of their equilibrium positions lead to acoustic phonons, while the out-of-phase movements of them result in optical phonons. These phonons, which carry energy, might scatter carriers and either increase or decrease the energy of them.

By assuming a constant matrix element and a constant energy for each phonon mode, the transition rate for the inelastic interactions with optical and intervalley

acoustic phonons in SiGe alloy is given by [11]

$$\begin{aligned} W^{v',v}(\vec{r},\vec{k}'|\vec{k}) = \big[1{-}x_{\mathrm{Ge}}(\vec{r})\big] & \frac{\pi (D_\eta^{\mathrm{Si}})^2}{V_0 \rho^{\mathrm{Si}} \omega_\eta^{\mathrm{Si}}} \Big[n_{\mathrm{eq}}(\hbar\omega_\eta^{\mathrm{Si}}, T_L) + \frac{1}{2} \pm \frac{1}{2}\Big] \\ & \delta\big[\varepsilon^{v'}(\vec{k}') - \varepsilon^{v}(\vec{k}) \pm \hbar\omega_\eta^{\mathrm{Si}}\big] r(\eta, v', v) \\ + x_{\mathrm{Ge}}(\vec{r}) & \frac{\pi (D_\eta^{\mathrm{Ge}})^2}{V_0 \rho^{\mathrm{Ge}} \omega_\eta^{\mathrm{Ge}}} \Big[n_{\mathrm{eq}}(\hbar\omega_\eta^{\mathrm{Ge}}, T_L) + \frac{1}{2} \pm \frac{1}{2}\Big] \\ & \delta\big[\varepsilon^{v'}(\vec{k}') - \varepsilon^{v}(\vec{k}) \pm \hbar\omega_\eta^{\mathrm{Ge}}\big] r(\eta, v', v), \end{aligned} \tag{2.28}$$

where ρ is the mass density (Tab. 2.1), D_η is the coupling constant, ω_η is the phonon frequency, r is the selection rule of the phonon mode η (Tab. 2.2) that in the case of a g-phonon refers to scattering of the electron into the opposite valley on the same principal axis, while in the case of an f-phonon denotes scattering to one of the four equivalent valleys on the principal axes perpendicular to the initial one, and $n_{\mathrm{eq}}(\hbar\omega_\eta, T_L)$ is the equilibrium distribution function of phonons given by the Bose-Einstein statistics

$$n_{\mathrm{eq}}(\hbar\omega_\eta, T_L) = \frac{1}{\exp\left(\frac{\hbar\omega_\eta}{k_B T_L}\right) - 1}. \tag{2.29}$$

where k_B is the Boltzmann constant. However, under high electric fields the distribution function of phonons can deviate considerably from the equilibrium value. Hence, we study separately the impact of non-equilibrium phonons on the carrier transport in chapter 3.

The transition rate for intravalley scattering with acoustic phonons in SiGe is given by elastic approximation [13]

$$\begin{aligned} W^{v',v}(\vec{r},\vec{k}'|\vec{k}) = \big[1 - x_{\mathrm{Ge}}(\vec{r})\big] & \frac{2\pi k_B T_L(\vec{r}) (\Xi^{\mathrm{Si}})^2}{V_0 \hbar \rho^{\mathrm{Si}} (u_l^{\mathrm{Si}})^2} \delta\big[\varepsilon^{v'}(\vec{k}') - \varepsilon^{v}(\vec{k})\big] \delta_{v',v} \\ + x_{\mathrm{Ge}}(\vec{r}) & \frac{2\pi k_B T_L(\vec{r}) (\Xi^{\mathrm{Ge}})^2}{V_0 \hbar \rho^{\mathrm{Ge}} (u_l^{\mathrm{Ge}})^2} \delta\big[\varepsilon^{v'}(\vec{k}') - \varepsilon^{v}(\vec{k})\big] \delta_{v',v}, \end{aligned} \tag{2.30}$$

where Ξ is the acoustic deformation potential, and u_l is the longitudinal sound velocity.

η	Mode	r	D_η [10^8eV/cm]	$\hbar\omega_\eta$ [meV]	D_η [10^8eV/cm]	$\hbar\omega_\eta$ [meV]
			Si		Ge	
Electrons						
1	TA	g	0.470	12.1	0.479	5.60
2	LA	g	0.740	18.5	0.772	8.60
3	LO	g	10.23	62.0	9.280	37.0
4	TA	f	0.280	19.0	0.283	9.90
5	LA	f	1.860	47.4	1.940	28.0
6	TO	f	1.860	58.6	1.690	32.5
Holes						
1			9.910	63.3	3.500	37.0

Table 2.2: Inelastic carrier-phonon scattering parameters

2.3.2 Ionized impurity scattering

Impurities, which are foreign atoms in the crystal lattice of semiconductors, have small ionization energies relative to the band gap energy. Hence, they are all ionized at typical operation temperatures. Ionized donors and acceptors are a common example of such impurities in a semiconductor. Coulombic interaction of charge carriers with an ionized impurity deviates the trajectory of these carriers, leading to a change in their momentum. Since the mass of a dopant atom is much larger than that of a charge carrier, energy exchange is negligible during this scattering event. The transition rate due to ionized impurities is modeled based on the Brooks and Herring approach by neglecting Umpklapp and interband processes as [25]

$$W^{v',v}(\vec{r},\vec{k}'|\vec{k}) = \frac{2\pi e^4\big(N_a(\vec{r}) + N_d(\vec{r})\big)}{V_0\hbar\kappa^2(\vec{r})\Big(\beta_{\rm sc}^2(\vec{r}) + \big(\vec{k}' - \vec{k}\big)^2\Big)^2}\delta\big[\varepsilon^{v'}(\vec{k}') - \varepsilon^{v}(\vec{k})\big]\delta_{v',v}, \tag{2.31}$$

where $\kappa(\vec{r})$ is the dielectric constant, which is obtained by linear interpolation in a SiGe alloy

$$\kappa(\vec{r}) = \big(1 - x_{\rm Ge}(\vec{r})\big)\kappa_{\rm Si} + x_{\rm Ge}(\vec{r})\kappa_{\rm Ge}, \tag{2.32}$$

in which $\kappa_{\rm Si}$ and $\kappa_{\rm Ge}$ are the dielectric constants of pure silicon and germanium, respectively, reported in Tab. 2.1, and the inverse screening length $\beta_{\rm sc}(\vec{r})$ is given

Type	$\mu_{\max}[\mathrm{cm}^2/\mathrm{Vs}]$	$\mu_{\min}[\mathrm{cm}^2/\mathrm{Vs}]$	$N_{\mathrm{ref}}[\mathrm{cm}^{-3}]$	α
E	1430	74.5	8.6×10^{16}	0.77
e	1430	200	5.3×10^{16}	0.68
H	480	47.0	1.7×10^{17}	0.79
h	480	122.3	1.4×10^{17}	0.70

Table 2.3: Mobility parameters of the Caughey-Thomas analytical expression for electrons/holes as majority carriers (E/H) and as minority carriers (e/h) in relaxed silicon at 300 K.

by

$$\beta^2_{\mathrm{sc}}(\vec{r}) = \frac{e^2\big(N_a(\vec{r})+N_d(\vec{r})\big)}{\kappa(\vec{r})k_BT_0}. \tag{2.33}$$

Due to the dependence on the momentum transfer $\vec{k}'-\vec{k}$ in Eq. 2.31, calculation of impurity scattering is computationally demanding. Therefore, we use a transition rate, which is approximated by velocity-randomizing assumption and isotropic-elastic process

$$W^{v',v}_{\mathrm{rel}}(\vec{r},\vec{k}'|\vec{k}) = \frac{1}{\tau\big(\varepsilon^v(\vec{k})\big)}\frac{\delta\big[\varepsilon^{v'}(\vec{k}')-\varepsilon^v(\vec{k})\big]\delta_{v',v}}{\frac{V_0}{(2\pi)^3}\sum_{v''}\int\delta\big[\varepsilon^{v''}(\vec{k}'')-\varepsilon^v(\vec{k})\big]d^3k''}. \tag{2.34}$$

where the relaxation time $\tau\big(\varepsilon^v(\vec{k})\big)$ is calculated by equating scattering rates obtained from Eq. 2.31 and Eq. 2.34. Hence, the approximated transition rate for impurity scattering under relaxation time approximation is expressed as

$$W^{v',v}_{\mathrm{rel}}(\vec{r},\vec{k}'|\vec{k}) = \frac{4\pi e^4\big(N_a(\vec{r})+N_d(\vec{r})\big)}{V_0\hbar\kappa^2(\vec{r})\beta^4_{\mathrm{sc}}(\vec{r})}\Theta_{\mathrm{imp}}\big(\eta(\varepsilon^v)\big)\delta\big[\varepsilon^{v'}(\vec{k}')-\varepsilon^v(\vec{k})\big]\delta_{v',v}, \tag{2.35}$$

where $\eta(\varepsilon)=4k^2(\varepsilon)/\beta^2_{\mathrm{sc}}$, and the function $\Theta_{\mathrm{imp}}(\eta)$ is introduced as

$$\Theta_{\mathrm{imp}}(\eta) = \begin{cases} \frac{1}{\eta^2}\big[\ln(1+\eta)-\frac{\eta}{1+\eta}\big] & \text{for } \eta\geq10^{-8} \\ \frac{1}{2}-\frac{2}{3}\eta & \text{for } \eta<10^{-8} \end{cases}. \tag{2.36}$$

Impurity scattering reduces the mobility of charge carriers, specially in highly doped semiconductors. However, the Brooks-Hering approach, which our transition rate is based on (Eq. 2.31), cannot accurately model the mobility at high doping concentrations. Thus, for the final transition rate of impurity scattering, we use

empirical fit factors as

$$W^{v',v}(\vec{r},\vec{k}'|\vec{k}) = \xi\big(N_a(\vec{r}),N_d(\vec{r})\big)W_{\text{rel}}^{v',v}(\vec{r},\vec{k}'|\vec{k}), \tag{2.37}$$

where the values of the fit factor $\xi\big(N_a(\vec{r}),N_d(\vec{r})\big)$ are selected to reproduce the Caughey-Thomas expressions for the mobility of electrons and holes as both majority and minority carriers in bulk silicon. This expression in general form is given by [26]

$$\mu(\vec{r}) = \mu_{\text{min}} + \frac{\mu_{\text{max}} - \mu_{\text{min}}}{1 + \left(\frac{N_a(\vec{r})+N_d(\vec{r})}{N_{\text{ref}}}\right)^{\alpha}}, \tag{2.38}$$

where the parameters of this model are determined by matching experimental data and reported in Tab. 2.3. Fig. 2.2 shows the simulated mobilities of electrons and holes compared with empirical data obtained from Eq. 2.38. Moreover, the fit factors $\xi\big(N_a(\vec{r}),N_d(\vec{r})\big)$ for different cases are shown in this figure. The same fit factors are used for SiGe material.

2.3.3 Alloy scattering

Randomized disorder in the SiGe alloy gives rise to an additional scattering process. Including intravalley and intervalley scattering, the transition rate of alloy scattering reads [27]

$$W^{v',v}(\vec{r},\vec{k}'|\vec{k}) = \big[1 - x_{\text{Ge}}(\vec{r})\big]x_{\text{Ge}}(\vec{r})\frac{\pi a_{\perp}(x_{\text{Ge}})a_{\parallel}^2U^2}{4V_0\hbar}\delta\big[\varepsilon^{v'}(\vec{k}') - \varepsilon^{v}(\vec{k})\big], \tag{2.39}$$

where the alloy scattering potential U is $0.75\,\text{eV}$ for electrons and $0.7\,\text{eV}$ for holes, $a_{\parallel}$ is the lattice constant parallel to the SiGe layer, which is assumed to be the bulk lattice constant of pure Si, $a_{0,\text{Si}}$, and $a_{\perp}(x_{\text{Ge}})$ is the lattice constant in growth direction, which is calculated from [15]

$$a_{\perp}(x_{\text{Ge}}) = a_0(x_{\text{Ge}})\left[1 - 2\frac{c_{12}(x_{\text{Ge}})}{c_{11}(x_{\text{Ge}})}\frac{a_{0,\text{Si}} - a_0(x_{\text{Ge}})}{a_0(x_{\text{Ge}})}\right], \tag{2.40}$$

where $c_{11}(x_{\text{Ge}})$ and $c_{12}(x_{\text{Ge}})$ are the elastic constants, which are obtained by a linear interpolation of the values for pure Si and Ge (Tab. 2.1), and $a_0(x_{\text{Ge}})$ is the lattice

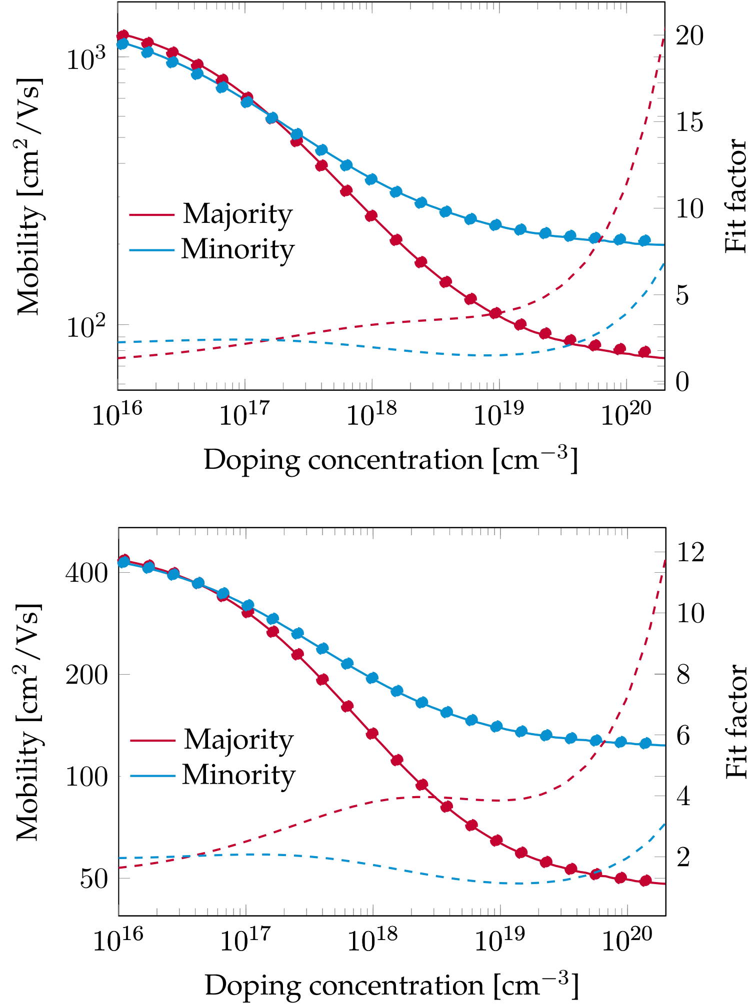

Figure 2.2: Electron (top) and hole (bottom) majority and minority mobilities (solid lines) and their corresponding fit factors (dashed lines).

constant for the bulk $Si_{1-x}Ge_x$ alloy given by

$$a_0(x_{\mathrm{Ge}}) = a_{0,\mathrm{Si}} + 0.200326\mathring{A}x_{\mathrm{Ge}}(\vec{r})\left[1 - x_{\mathrm{Ge}}(\vec{r})\right] + (a_{0,\mathrm{Ge}} - a_{0,\mathrm{Si}})x^2_{\mathrm{Ge}}(\vec{r}). \quad (2.41)$$

2.3.4 Impact ionization

One energetic carrier can generate a new pair of electron and hole via II. In the process of II due to primary electrons, one electron with enough energy in the con-

duction band interacts via Coulomb forces with another electron in the valence band and loses energy. Consequently, the latter electron gains energy and is transferred to the conduction band resulting in a secondary hole in the valence band. Since three particles are involved in this process, direct evaluation of the transition rate is very difficult and needs different levels of approximation. Therefore, we use a fully energy dependent scattering rate, determined by basic experimental data. The scattering rate due to II of primary electrons in relaxed silicon is given by [28]

$$S_{\mathrm{II}}(\varepsilon) = \begin{cases} 1.49 \times 10^{11} \frac{1}{\mathrm{s}} (\frac{\varepsilon}{\mathrm{eV}} - 1.128)^3 & 1.128\mathrm{eV} < \varepsilon < 1.750\mathrm{eV} \\ 1.13 \times 10^{12} \frac{1}{\mathrm{s}} (\frac{\varepsilon}{\mathrm{eV}} - 1.572)^2 & 1.750\mathrm{eV} \leq \varepsilon \end{cases}, \tag{2.42}$$

and for primary holes is written as

$$S_{\mathrm{II}}(\varepsilon) = 6 \times 10^{13} \frac{1}{\mathrm{s}} (\frac{\varepsilon}{\mathrm{eV}} - 1.49)^{3.4}, \quad \text{for} \quad \varepsilon > 1.49\,\mathrm{eV}. \tag{2.43}$$

The final energy of all three carriers after scattering is assumed to be similar as

$$\varepsilon^{\mathrm{II}}(\varepsilon) = \frac{\varepsilon - E_{\mathrm{gap}}}{3}, \tag{2.44}$$

where ε is the energy of the primary carrier, and E_{gap} is the energy of the band gap. As a result, a transition rate of the form

$$W^{v',v}(\varepsilon'|\varepsilon) = \frac{S_{\mathrm{II}}(\varepsilon)}{\sum_{v'} Z^{v'}\big(\varepsilon^{\mathrm{II}}(\varepsilon)\big)} \delta\big[\varepsilon' - \varepsilon^{\mathrm{II}}(\varepsilon)\big] \tag{2.45}$$

can reproduce the scattering rates of II.

2.4 Shockley-Read-Hall recombination/generation

The transition of an electron from the conduction band to the valence band through one or multiple steps, leading to annihilation of an electron-hole pair, is known as the recombination process, whereas the reverse transition is referred to generation. In a trap-assisted recombination process, described by the SRH recombination model, an electron in the conduction band or a hole in the valence band is trapped

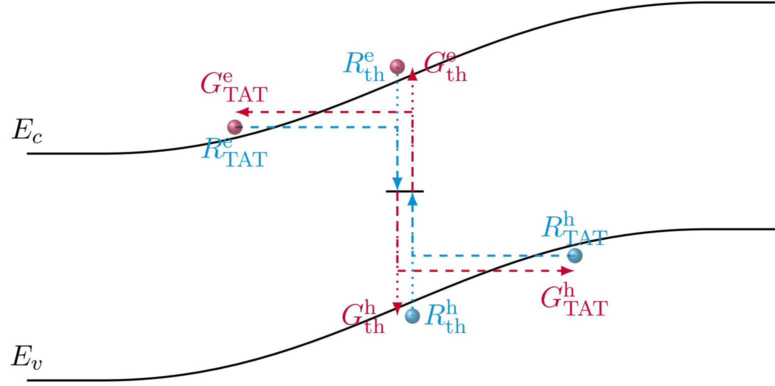

Figure 2.3: Energy-band diagram of a depletion region with thermally-induced and trap-assisted-tunneling recombination/generation.

by an energy state within the bandgap of the semiconductor with the corresponding rates of $R^e_{\rm th}$ and $R^h_{\rm th}$, respectively (Fig. 2.4). This trap state, which is caused by the presence of a guest atom or a structural defect, exchanges energy with carriers via phonons; therefore, this process is known as thermally-induced trap-assisted SRH recombination. In addition, an electron in the conduction band can firstly tunnel through the band gap, and then transit to the trap state ($R^e_{\rm TAT}$). This field-enhanced recombination process, which is known as trap-assisted-tunneling (TAT), can increase the recombination rate in high electric field domains dramatically. A superposition of these two processes is modeled as a field-enhanced SRH recombination [29], in which the recombination rate is given by

$$R^{e/h}(\vec{r},k) = \sigma_T^{e/h}(\vec{r}) v_g^{e/h}(k) \tag{2.46}$$

and the generation rate is obtained from the principle of detailed balance as

$$G^{e/h}(\vec{r},k) = \sigma_T^{e/h}(\vec{r}) v_g^{e/h}(k) \exp\left(\frac{\pm\big(E_T(\vec{r}) - \varepsilon\big)}{k_B T_0}\right) \tag{2.47}$$

where $E_T(\vec{r})$ is the trap state energy level, and $\sigma_T^{e/h}(\vec{r})$ is the field-enhanced capture cross section of the traps, which is defined as

$$\sigma_T^{e/h}(\vec{r}) = \sigma_0^{e/h}\big(1 + \gamma_{\rm TAT}^{e/h}(\vec{r})\big) \tag{2.48}$$

where the field-effect function $\gamma^{e/h}_{\mathrm{TAT}}(\vec{r})$ is given by [29]

$$\gamma^{e/h}_{\mathrm{TAT}}(\vec{r}) = \frac{\Delta E_{e/h}(\vec{r})}{k_B T_0} \int_0^1 \exp\left[\frac{\Delta E_{e/h}(\vec{r})}{k_B T_0} u - K_{e/h}(\vec{r}) u^{3/2}\right] du \tag{2.49}$$

with

$$K_{e/h}(\vec{r}) = \frac{4}{3} \frac{\sqrt{2 m^*_{e/h} \Delta E^3_{e/h}(\vec{r})}}{q\hbar |\vec{E}(\vec{r})|} \tag{2.50}$$

where the integration intervals $\Delta E_{e/h}(\vec{r})$ are defined based on the electrostatics of the device, as

$$\Delta E_e(\vec{r}) = \begin{cases} E_c(\vec{r}) + q\phi_n(\vec{r}) & \text{for } E_T(\vec{r}) \leq -q\phi_n(\vec{r}) \\ E_c(\vec{r}) - E_T(\vec{r}) & \text{for } E_T(\vec{r}) > -q\phi_n(\vec{r}) \end{cases} \tag{2.51}$$

and

$$\Delta E_h(\vec{r}) = \begin{cases} -q\phi_p(\vec{r}) - E_v(\vec{r}) & \text{for } E_T(\vec{r}) > -q\phi_p(\vec{r}) \\ E_T(\vec{r}) - E_v(\vec{r}) & \text{for } E_T(\vec{r}) \leq -q\phi_p(\vec{r}) \end{cases} \tag{2.52}$$

where ϕ_n and ϕ_p are the local quasi-Fermi levels of electrons and holes, respectively. The required parameters for field-enhanced SRH recombination is obtained from [30], while a scaling factor is used for the the total rate to reproduce measurement data. The trap-assisted SRH process can be described by the local occupation probability of the trap states $f_T(\vec{r})$. Therefore, the rate equation for the occupancy of the trap states is given by

$$\begin{aligned} \frac{\partial f_T(\vec{r})}{\partial t} = \frac{1}{(2\pi)^3} \int \Big[& f_T(\vec{r}) \big[R^h(\vec{r}, k') f^h(\vec{r}, \vec{k}') - G^e(\vec{r}, k') \big] \\ & + \big(1 - f_T(\vec{r})\big) \big[R^e(\vec{r}, k') f^e(\vec{r}, \vec{k}') - G^h(\vec{r}, k') \big] \Big] d^3k'. \end{aligned} \tag{2.53}$$

In order to include recombination/generation processes, a coupled system of BTEs for electrons and holes (will be introduced in Sec. 2.8) has to be considered. The SRH recombination operators for the BTEs of electrons and holes 2.1 are defined, respectively, as

$$\Gamma^e\{f^e, f^h\} = N_T(\vec{r}) \Big[R^e(\vec{r}, k) \big(1 - f_T(\vec{r})\big) f^e(\vec{r}, \vec{k}) - G^e(\vec{r}, k) f_T(\vec{r}) \Big] \tag{2.54}$$

	Direct BTBT		Indirect BTBT	
x_{Ge}	$A_{\mathrm{dir}}[\mathrm{cm}^{-3}\mathrm{s}^{-1}]$	$B_{\mathrm{dir}}[\mathrm{MVcm}^{-1}]$	$A_{\mathrm{ind}}[\mathrm{cm}^{-3}\mathrm{s}^{-1}]$	$B_{\mathrm{ind}}[\mathrm{MVcm}^{-1}]$
0.0	1.35×10^{20}	101	3.29×10^{15}	23.8
0.3	1.33×10^{20}	66.5	2.61×10^{15}	18.1

Table 2.4: Direct and indirect BTBT parameters for two different Ge contents

$$\Gamma^h\{f^e, f^h\} = N_T(\vec{r})\Big[R^h(\vec{r}, k) f_T(\vec{r}) f^h(\vec{r}, \vec{k}) - G^h(\vec{r}, k)\big(1 - f_T(\vec{r})\big)\Big] \tag{2.55}$$

where $N_T(\vec{r})$ is the density of trap states.

2.5 Band-to-band tunneling

Under very high electric field, an electron in the valence band can directly tunnel through the semiconductor gap and reach to the conduction band. A local model for this phenomena, which is based on the electric field, considers a generated electron-hole pair at the same place. The local generation operator due to both direct and indirect BTBT can be written as [29]

$$G^{\mathrm{BTBT}}\{f^e, f^h\} = (G_{\mathrm{dir}} + G_{\mathrm{ind}})\left(\frac{n_i^2 - n(\vec{r})p(\vec{r})}{\big(n(\vec{r}) + n_i(\vec{r})\big)\big(p(\vec{r}) + n_i(\vec{r})\big)}\right)\left(\frac{N_{c/v}(\vec{r}) f_{\mathrm{eq}}^{e/h}(\varepsilon)}{n_0(\vec{r})}\right) \tag{2.56}$$

where $n_i(\vec{r})$ is the intrinsic carrier density, $N_c(\vec{r})$ and $N_v(\vec{r})$ are the effective density of states for the conduction and valence bands, respectively, $n_0(\vec{r})$ is the density of electrons at thermal equilibrium, and f_{eq}^e is the equilibrium distribution function. The direct and indirect BTBT generation rates can be written as

$$G_{\mathrm{dir/ind}}(\vec{r}) = A_{\mathrm{dir/ind}}\left(\frac{|\vec{E}(\vec{r})|}{F_0}\right)^{p_{\mathrm{dir/ind}}} \exp\left(-\frac{B_{\mathrm{dir/ind}}}{|\vec{E}(\vec{r})|}\right) \tag{2.57}$$

where F_0 = 1 V/cm, p_{dir} = 2 and p_{ind} = 2.5 for the direct and indirect BTBT, respectively, and $A_{\mathrm{dir/ind}}$ and $B_{\mathrm{dir/ind}}$ are the Kane factors, which are calculated for the direct and indirect BTBT based on the given germanium content [31]. Tab. 2.4 shows these parameters for two different Ge contents, while it is observed that in our desired range of Ge content ($X_{\mathrm{Ge}} < 0.3$) indirect BTBT is dominant. Further-

more, to match experimental results, a global scaling factor is multiplied to this generation rate.

2.6 Spherical harmonics expansion

The SHE method is the most sophisticated approach to solve the BTE in a deterministic manner without stochastic errors. The main idea of this method is to use spherical coordinates for the k-space and expand the dependence on the two angles with spherical harmonics, which are defined as

$$Y_{l,m}(\theta,\phi) = \begin{cases} c_{l,m}\cos(m\phi)P_l^m(\cos\theta) & \text{for } m \geq 0 \\ c_{l,m}\sin(-m\phi)P_l^{-m}(\cos\theta) & \text{for } m < 0 \end{cases}, \tag{2.58}$$

where θ and ϕ are angles in the spherical coordinate system, $l \geq 0$ is the spherical harmonics order and m is the sub-order index, which is bounded by $-l \leq m \leq l$. The normalization factor $c_{l,m}$ is given by

$$c_{l,m} = \begin{cases} \sqrt{\frac{(2l+1)}{4\pi}} & \text{for } m = 0 \\ \sqrt{\frac{(2l+1)(l-|m|)!}{2\pi(l+|m|)!}} & \text{for } m \neq 0 \end{cases}. \tag{2.59}$$

$P_l^m(x)$ is the associated Legendre polynomials

$$P_l^m(x) = (1-x^2)^{\frac{m}{2}}\frac{d^m}{dx^m}P_l(x), \tag{2.60}$$

with the Legendre polynomials defined as

$$P_l(x) = \frac{1}{2^l l!}\frac{d^l}{dx^l}(x^2-1)^l. \tag{2.61}$$

The spherical harmonics up to first order are obtained as

$$Y_{0,0}(\theta,\phi) = \frac{1}{\sqrt{4\pi}}, \tag{2.62}$$

$$Y_{1,-1}(\theta,\phi) = \sqrt{\frac{3}{4\pi}}\sin\theta\sin\phi, \tag{2.63}$$

$$Y_{1,0}(\theta,\phi) = \sqrt{\frac{3}{4\pi}}\cos\theta, \tag{2.64}$$

$$Y_{1,1}(\theta,\phi) = \sqrt{\frac{3}{4\pi}}\sin\theta\cos\phi. \tag{2.65}$$

The spherical harmonics are orthonormal and form a complete set of basis functions

$$\underbrace{\int_{\theta=0}^{\pi}\int_{\phi=0}^{2\pi}}_{\equiv\oint} Y_{l,m}(\theta,\phi)Y_{l',m'}(\theta,\phi)\underbrace{\sin\theta d\phi d\theta}_{\equiv d\Omega} = \delta_{l,l'}\delta_{m,m'}, \tag{2.66}$$

where the Kronecker delta $\delta_{l,l'} = 1$ only if $l = l'$, otherwise it is equal to zero. A quantity $X(\theta,\phi)$ is expanded with these basis functions as

$$X_{l,m} = \oint X(\theta,\phi)Y_{l,m},(\theta,\phi)d\Omega \tag{2.67}$$

and the original quantity can be recovered by a truncated expansion, leading to a finite number of unknowns for the angular dependence, as

$$X(\theta,\phi) = \underbrace{\sum_{l=0}^{L_{\max}}\sum_{m=-l}^{l}}_{\sum_{l,m}} X_{l,m}Y_{l,m}(\theta,\phi), \tag{2.68}$$

where $L_{\max}$ is the maximum expansion order.

Since it has been demonstrated that expansion of the distribution function on an equienergy surface has many advantages over an expansion with respect to the modulus of the wave-vector [32], we exploit the expansion coefficients for the distribution function on equienergy surfaces given by [12]

$$f^v_{l,m}(\vec{r},\varepsilon) = \frac{1}{(2\pi)^3}\int_{\mathrm{BZ}}\delta\big(\varepsilon-\varepsilon(\vec{k})\big)Y_{l,m}(\theta,\phi)f^v(\vec{r},\vec{k})d^3k, \tag{2.69}$$

where the following conventional relation

$$\frac{1}{(2\pi)^3}d^3k = Z^v(\varepsilon)d\varepsilon d\Omega, \tag{2.70}$$

is used to transform the integral over the k-space to an integral over energy. In a similar manner, the BTE is projected onto spherical harmonics

$$\frac{1}{(2\pi)^3}\int_{\mathrm{BZ}}\delta\big(\varepsilon-\varepsilon(\vec{k})\big)Y_{l,m}(\theta,\phi)\{\mathrm{BTE}\}d^3k, \tag{2.71}$$

in which the expansion of each term is discussed separately in the following subsections.

2.6.1 Free-streaming operator

The expansion of the diffusion term evaluates to

$$\frac{1}{(2\pi)^3}\int_{\mathrm{BZ}}\delta\big(\varepsilon-\varepsilon(\vec{k})\big)Y_{l,m}(\theta,\phi)\Big[\vec{v}(\vec{k})\cdot\nabla_r f(\vec{r},\vec{k})\Big]d^3k=\nabla_r\cdot\vec{j}_{l,m}(\vec{r},\varepsilon), \tag{2.72}$$

where the projected current density $\vec{j}_{l,m}(\vec{r},\varepsilon)$ is introduced as

$$\vec{j}_{l,m}(\vec{r},\varepsilon)=\oint\vec{v}(\vec{k})f(\vec{r},\vec{k})Y_{l,m}(\theta,\phi)Z(\varepsilon)d\Omega. \tag{2.73}$$

The drift term is expanded into spherical harmonics by

$$\begin{aligned}\frac{1}{(2\pi)^3}\int_{\mathrm{BZ}}\delta\big(\varepsilon-\varepsilon(\vec{k})\big)Y_{l,m}(\theta,\phi)\Big[\frac{1}{\hbar}\vec{F}(\vec{r})\cdot\nabla_k f(\vec{r},\vec{k})\Big]d^3k=&\\ \vec{F}(\vec{r})\cdot\Big\{\frac{\partial j_{l,m}(\vec{r},\varepsilon)}{\partial\varepsilon}-A_{l,m}(\vec{r},\varepsilon)\Big\},&\end{aligned} \tag{2.74}$$

where the drift coefficient is defined as

$$A_{l,m}(\vec{r},\varepsilon)=\frac{1}{\hbar k}\oint\left(\frac{\partial Y_{l,m}(\theta,\phi)}{\partial\theta}\vec{e_\theta}+\frac{1}{\sin\theta}\frac{\partial Y_{l,m}(\theta,\phi)}{\partial\phi}\vec{e_\phi}\right)f(\vec{r},\vec{k})d\Omega. \tag{2.75}$$

2.6.2 Scattering operator

The scattering operator is split into in- and out-scattering terms as

$$S\{f\}=S^{\mathrm{in}}\{f\}-S^{\mathrm{out}}\{f\}. \tag{2.76}$$

Based on the fact that our transition rates are assumed to be velocity randomizing, i.e. these rates do not depend on the scattering angles and by neglecting the Pauli's principle, projection of the in- and out-scattering terms yield, respectively [12]

$$S^{\text{in}}_{l,m}(\vec{r},\varepsilon) = \frac{V_0}{Y^2_{0,0}} \sum_{v'} \int W^{v',v}(\vec{r},\varepsilon'|\varepsilon) f^{v'}_{0,0}(\vec{r},\varepsilon') Z(\varepsilon) Z(\varepsilon') d\varepsilon', \tag{2.77}$$

$$S^{\text{out}}_{l,m}(\vec{r},\varepsilon) = \frac{V_0}{Y^2_{0,0}} \sum_{v'} \int W^{v,v'}(\vec{r},\varepsilon|\varepsilon') f^{v}_{l,m}(\vec{r},\varepsilon) Z(\varepsilon) Z(\varepsilon') d\varepsilon'. \tag{2.78}$$

2.6.3 Recombination/generation operator

The coupling terms due to recombination and generation in the BTEs of electrons and holes, which are defined in Eq. 2.54 and Eq. 2.54, are projected into spherical harmonics, respectively, as

$$\Gamma^e_{l,m}(\vec{r},\varepsilon) = N_T(\vec{r}) Z^e(\varepsilon) \Big[R^e(\vec{r},\varepsilon)\big(1 - f_T(\vec{r})\big) f^e_{l,m}(\vec{r},\varepsilon) - \frac{1}{Y_{0,0}} G^e(\vec{r},\varepsilon) f_T(\vec{r}) \Big], \tag{2.79}$$

$$\Gamma^h_{l,m}(\vec{r},\varepsilon) = N_T(\vec{r}) Z^h(\varepsilon) \Big[R^h(\vec{r},\varepsilon) f_T(\vec{r}) f^h_{l,m}(\vec{r},\varepsilon) - \frac{1}{Y_{0,0}} G^h(\vec{r},\varepsilon)\big(1 - f_T(\vec{r})\big) \Big], \tag{2.80}$$

where $f_T(\vec{r})$ is the solution of the Eq. 2.53, which has to be solved self-consistently.

2.7 H-transform

The coupling between the spatial derivative and the derivative w.r.t energy, which are introduced in the projection of the Free-streaming operator, can make instabilities in the solution. To avoid these numerical problems, we use a variable transformation from energy-space to H-space, which is given by

$$H(\vec{r}) = \begin{cases} \varepsilon - e\Psi(\vec{r}) + E_c(\vec{r}) & \text{for electrons} \\ \varepsilon + e\Psi(\vec{r}) - E_v(\vec{r}) & \text{for holes} \end{cases}, \tag{2.81}$$

where $\Psi(\vec{r})$ is the electrostatic potential. By using this specific choice of H-transform, projection of the Free-streaming operator simplifies to

$$\nabla_r \cdot \vec{j}_{l,m}(\vec{r},\varepsilon) + \vec{F}(\vec{r}) \cdot \left\{ \frac{\partial j_{l,m}(\vec{r},\varepsilon)}{\partial \varepsilon} - A_{l,m}(\vec{r},\varepsilon) \right\} = \nabla_r \cdot \vec{j}_{l,m}(\vec{r},H) - \vec{F}(\vec{r}) \cdot A_{l,m}(\vec{r},H). \tag{2.82}$$

As a result, the projection of the Free-streaming operator only contains differentials w.r.t the position. However, it results in a potential-dependent energy grid.

2.8 Coupled system of equations

In order to investigate bipolar effects in SiGe HBTs, a coupled system of BTEs for electrons and holes has to be considered. These BTEs for electrons and holes under stationary conditions can be expressed, respectively, as

$$L^e\{f^e\} = S\{f^e\} + Q\{f^e, f^h\} - \Gamma^e\{f^e, f^h\} + G^e_{\mathrm{BTBT}}\{n,p\}, \tag{2.83}$$

$$L^h\{f^h\} = S\{f^h\} + Q\{f^e, f^h\} - \Gamma^h\{f^e, f^h\} + G^h_{\mathrm{BTBT}}\{n,p\}, \tag{2.84}$$

where $L^{e/h}\{f^{e/h}\}$ is the free-streaming operator, $S\{f^{e/h}\}$ is the scattering operator, which accounts for carrier-phonon scattering, impurity scattering, alloy scattering, and II scattering of primary particles, $Q\{f^e, f^h\}$ is the generation operator of secondary particles due to II, $\Gamma^{e/h}\{f^e, f^h\}$ is the SRH recombination operator, and $G^{e/h}_{\mathrm{BTBT}}\{n,p\}$ is the BTBT generation operator. To obtain the electrostatic potential, the Poisson's equation has to be solved, which reads [33]

$$\nabla \cdot \big(\kappa(\vec{r})\nabla\psi\big) = e\big(n(\vec{r}) - p(\vec{r}) + N_a(\vec{r}) - N_d(\vec{r}) - C_T(\vec{r})\big), \tag{2.85}$$

where $C_T(\vec{r})$ is the density of the trapped charges. At the artificial boundaries of the simulation domain, we consider Neumann boundary condition for this equation, which is fulfilled directly as a consequence of the box integration method. For the

terminal contacts, the Dirichlet boundary condition is used, which is given by

$$\psi_{\text{cont}}(\vec{r}) = V_{\text{ap}} + \frac{k_B T_L}{e} \operatorname{arcsinh}\Big(\frac{N_d(\vec{r}) - N_a(\vec{r})}{2n_i(\vec{r})}\Big) - \Phi_h(\vec{r}), \tag{2.86}$$

where V_{ap} is the applied bias voltage, and $\Phi_h(\vec{r})$ is the workfunction difference relative to relaxed silicon (RSi) defined as

$$\Phi_h(\vec{r}) = \frac{1}{2}\Bigg(- \frac{E_c(\vec{r}) - E_c^{\text{RSi}} + E_v(\vec{r}) - E_v^{\text{RSi}}}{e} + \frac{k_B T_L(\vec{r})}{e} \ln\Big(\frac{N_c(\vec{r}) N_v^{\text{RSi}}}{N_v(\vec{r}) N_c^{\text{RSi}}}\Big)\Bigg). \tag{2.87}$$

A solution of this Boltzmann-Poisson system is needed and often referred to as self-consistent solution of the BTE.

2.9 Boundary condition

The Robin boundary condition for the BTEs defined in Eq. 2.83 and Eq. 2.84, is applied by an interface generation rate, given by

$$\gamma^v(\vec{r}, \vec{k}) = v_r \big[f^v(\vec{r}, \vec{k}) - f_{\text{eq}}^{e/h}(\varepsilon)\big], \tag{2.88}$$

which is added to the right hand side of these equations for the direct nodes at the terminal contacts. In this manner, the interface recombination velocity v_r determines the number of injected carriers from the terminal contact.

2.10 Discretization

To numerically solve the coupled system of equations introduced in Sec. 2.8, they have to be discretized in real- and energy-spaces. The box integration method [34] is employed for discretization of the real space based on a 2-D Delaunay grid. In this method, the surrounding box volume for the direct grid node i_d (shown in Fig. 2.4), which contains all points closest to the corresponding grid node, is used as the unit cell for discretization, and the middle points along the lines between two

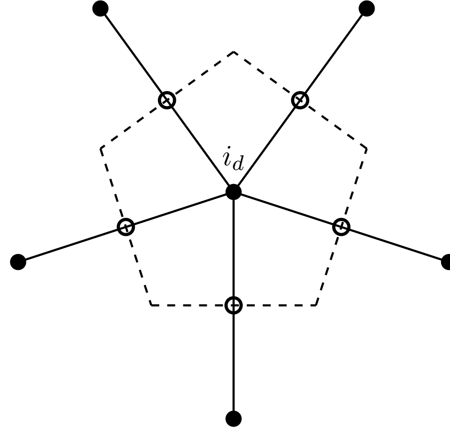

Figure 2.4: Direct node i_d (filled circle) and its surrounding box volume. Adjoint nodes are shown by open circles.

neighboring direct nodes are defined as the adjoint nodes. The carrier distribution functions are split into even and odd parts, where the even part defined on the direct grid nodes yields carrier densities, and the odd part assigned to the adjoint nodes yields fluxes, such as the current density.

To discretize the energy-space, an equidistant grid with energy distance ΔH is used. The total energy range for the n-th energy point H_n is defined as $(H_n - \Delta H/2, H_n + \Delta H/2)$. However, if this range includes the valley minimum, the integral over the energy space is calculated from that value. Therefore, the minimum of the total energy at each energy box in general case is given by

$$H_n^{\min}(\vec{r}) = \min\Big\{H_n + \frac{\Delta H}{2}, \max\big\{H_n - \frac{\Delta H}{2}, \pm\big(E_{c,v}(\vec{r}) - q_e\Psi(\vec{r})\big)\big\}\Big\}, \qquad (2.89)$$

where the upper (lower) sign is for electrons (holes). Since $H_n^{\min}(\vec{r})$ depends on the electrostatic potential, it has to be updated at each iteration step.

2.11 I-V characteristics of SiGe HBTs

In order to validate the results of the SHE solver, we compare simulation results with measurement data from state-of-the-art SiGe HBTs. A 2-D real space struc-

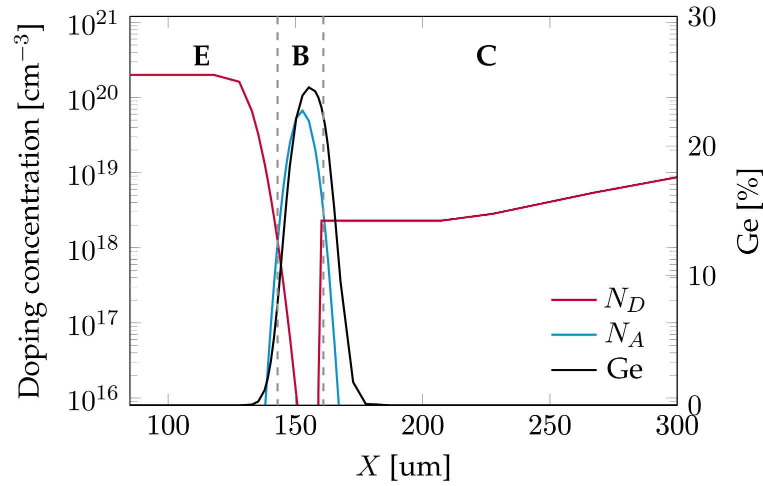

Figure 2.5: Doping concentrations and Ge content profiles of the investigated SiGe HBT along the symmetry axis.

ture was generated, the doping profiles of which were extracted by secondary ion mass spectrometry from a toward-terahertz SiGe npn HBT fabricated by Infineon Technologies AG. Fig. 2.5 shows the donor concentration, acceptor concentration, and Ge content profiles along the symmetry axis of the investigated SiGe HBT. The electrostatic potential, which is obtained from a self-consistent solution of the BTEs of electrons and holes and the Poisson's equation, is shown for different forward-mode bias conditions in Fig. 2.6. The energy barrier at the EB junction is strongly reduced by increasing the corresponding bias leading to an exponentially increase in the injected charge carriers and resulting currents. Fig. 2.7 shows the electron and hole densities at $V_{\mathrm{BE}} = 0.8\mathrm{V}$.

As the first step for the characterization of the device, we obtain the Gummel plot, which is the combined plot of the collector current I_C and base current I_B versus the base-emitter voltage while the collector-base bias is set to zero ($V_{\mathrm{CB}} = 0\mathrm{V}$). In order to perform CPU efficient simulations, a third-order SHE with including full band structure effects is used, while higher harmonics do not have a considerable impact on the electrical characteristics. The described band gap narrowing, carrier-phonon scattering, impurity scattering and alloy scattering models with the reported parameters are used in this simulation.

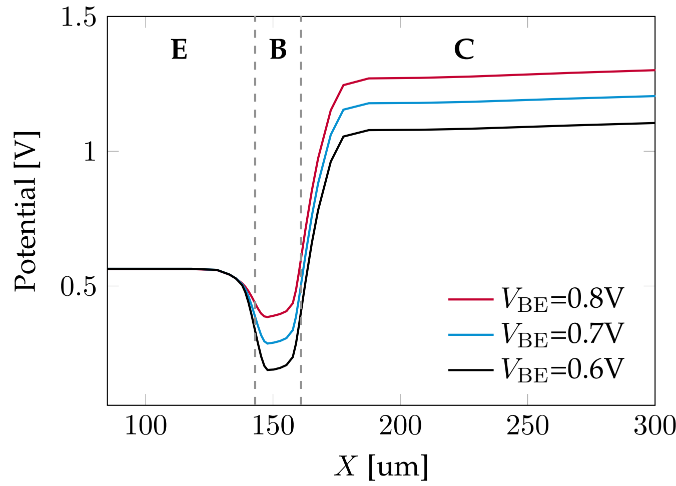

Figure 2.6: Electrostatic potential at $V_{CB} = 0$V along the symmetry axis of the investigated SiGe HBT.

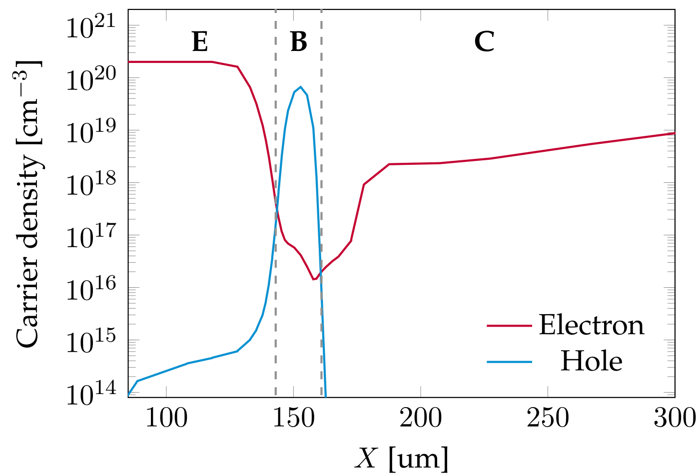

Figure 2.7: Electron and hole densities at $V_{BE} = 0.8$ V and $V_{CB} = 0$ V, along the symmetry axis of the SiGe HBT.

Fig. 2.8 represents the Gummel plot for the investigated SiGe HBT compared with measurements. Due to minor uncertainty in the extracted Ge profile, we are allowed to change Ge content by a few percent to reproduce our measured I_C at $T_0 = 300$ K from simulation. Moreover, the peak of the doping concentration at the emitter region is 1.6×10^{21}cm^{-3}, while the maximum dose that can be electrically activated and used in our numerical simulations is 2×10^{20}cm^{-3}. However, band

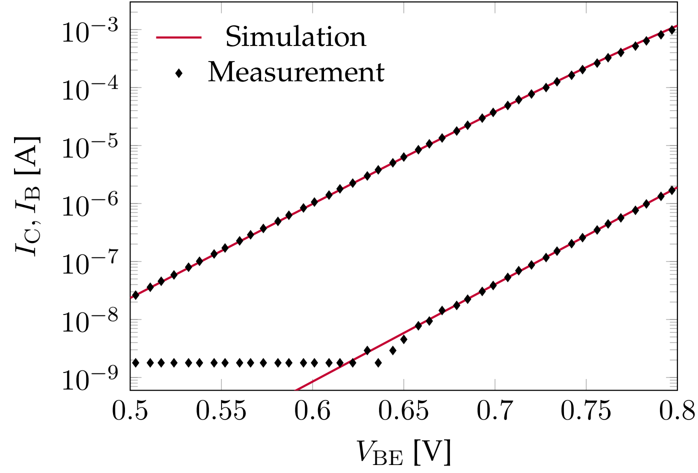

Figure 2.8: Gummel characteristics of the SiGe HBT in comparison to measurement data. The leakage currents observed for the fresh device are due to packaging and are not taken into account in our simulation.

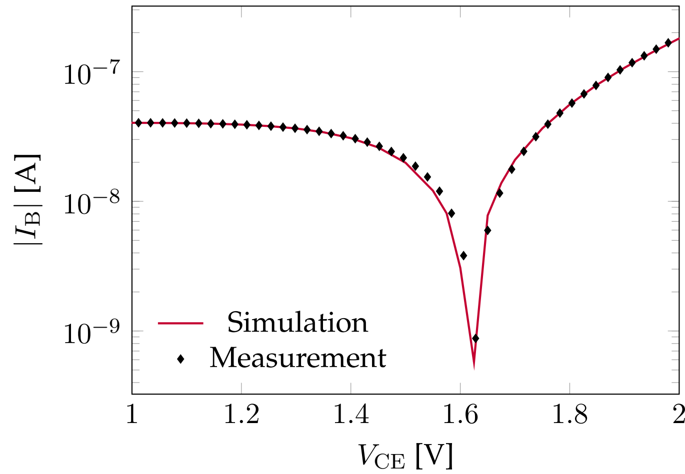

Figure 2.9: I_B-V_{CE} characteristic at V_{BE}=0.7V

gap narrowing might have a bigger parameter proportional to the real value of the doping concentration ($1.6 \times 10^{21}\,\mathrm{cm}^{-3}$) at the emitter. Therefore, a scaling parameter for the band gap narrowing at the emitter region was defined and used as a calibration parameter to reproduce the measured base current. It is noteworthy that in our simulations, the degeneracy effects due to high doping concentrations in the emitter and collector regions are captured by the modified impurity scattering rate and bandgap narrowing [35, 36].

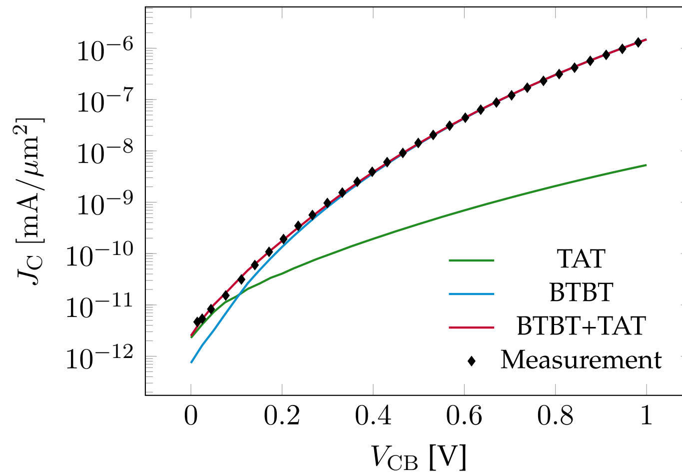

Figure 2.10: Simulated tunneling currents at V_{BE}=0V compared to measurement.

In a common-emitter configuration, increasing the collector-emitter voltage induces II. The avalanche multiplication of carriers, which happens at V_{CE}>BV_{CEO}, makes the II current prominent and reverses the base current direction. Therefore, the base current reversal in I_B-V_{CE} characteristic is used as a basis to calibrate the global scaling parameter of the II rates initiated by primary electrons and holes. Fig. 2.9 shows the I_B-V_{CE} curve obtained from SHE simulation in comparison to measurement data, which both report $BV_{CEO} = 1.6$ V.

If the base-emitter junction is not forward biased, we expect very small number of charge carriers that enter the base and move to the collector. However, increasing V_{CB} can enhance electric field in the collector-base junction leading to tunneling currents. Fig. 2.10 shows the J_C-V_{CB} curve at $V_{BE} = 0$ V from 1D SHE simulation compared to measurements. These results show that at $V_{CB} < 0.15$ V, TAT has the main share of the tunneling current, whereas for higher V_{CB} the current due to BTBT becomes dominant.

Chapter 3

Electrothermal Effects

3.1 Thermal issues in SiGe HBTs

To continue the trend in frequency performance improvement, SiGe HBTs have to be operated at higher current densities. This inevitable increase in operating current together with continuous lateral and vertical downscaling, leading to stronger internal electric fields, has remarkably increased heat generation inside the devices. Therefore, self-heating effects in bipolar transistors, which cause an increase of the collector current, may lead to thermal instability. This positive current-temperature feedback sets an upper limit on the current density, which limits the SOA of bipolar transistors [37].

In addition, adding germanium to silicon and using shallow/deep trench isolation schemes to reduce the parasitic capacitances [38] result in a large reduction of the thermal conduction, which restricts the spreading of the generated heat. Hence, a deeper insight into the microscopic mechanisms of heat generation and dissipation inside the SiGe HBTs as well as their impact on the electrical characteristics is necessary.

In order to study electrothermal effects in bipolar transistors, a state-of-the-art

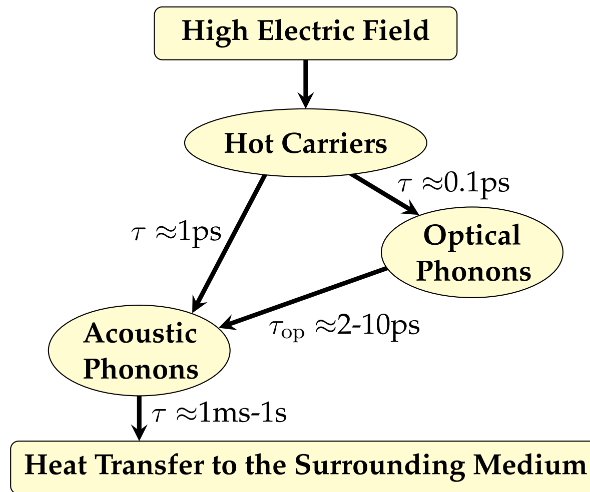

Figure 3.1: Diagram of thermal energy transport in semiconductors.

toward-terahertz SiGe HBT fabricated by Infineon Technologies AG with an emitter width $W_{\rm E} = 0.13\,\mu$m and length $L_{\rm E} = 2.73\,\mu$m, and belonging to a technology development stage referred to as set #3 in [39], was used to extract the thermal resistance based on simple DC measurements. Our simulation results are validated against electrical and thermal characteristics of this device.

3.2 Advanced electrothermal device simulation

High electric fields in semiconductor devices accelerate charge carriers and increase their kinetic energy. Carriers with energies greater than 60 meV scatter mainly with optical phonons, which have a negligible group velocity and cannot participate in heat transport. Instead, optical phonons decay into long wavelength acoustic phonons, which dominate heat transport in semiconductors. However, this decay is relatively slow compared to the carrier-phonon interactions and as a result, a bottleneck for energy dissipation can occur, which leads to a large number of optical phonons in high-field domains. Fig. 3.1 illustrates symbolically the carrier-phonon and phonon-phonon interaction processes with their corresponding scattering time constants [40]. In order to precisely investigate self-heating in nanoscale bipolar transistors, a coupled system of transport equations for carriers and phonons has

to be considered. For this purpose, the coupling term in the phonon equations, which describes carrier-phonon interactions, has to be modeled properly.

In fact, hot carriers do not release their energy to the lattice exactly at the same position where they receive it and they diffuse several mean free paths (10-50 nm) before they lose the energy. Therefore, the so-called Joule-heating term, which is widely used in thermal simulation of bipolar transistors [41], just represents the energy that carriers gain from the electric field and is not appropriate for calculating the spatial distribution of heat generation. To tackle this problem, an advanced hydrodynamic model describing heat generation and transport in submicron silicon devices has been proposed in [42]. However, this approach is still based on a single averaged carrier temperature within the relaxation time approximation and also does not account for the spectral information regarding the emitted phonons.

Since lattice heating is due to inelastic carrier-phonon scattering, which is described in detail by the scattering integral of the BTE, the BTE is the most accurate approach for a comprehensive investigation of the carrier-phonon interactions [43]. The energy loss rate due to inelastic carrier-phonon scattering can be calculated from the corresponding scattering rate as

$$E_{\mathrm{loss}} = \frac{2V_0}{(2\pi)^6} \sum_{v} \sum_{v'} \sum_{\eta} \int \int \hbar\omega_{\eta} f^{v}(\vec{r},\vec{k}) \Big[W^{v,v'}_{\eta,\mathrm{em}}(\vec{r},\vec{k}|\vec{k}') - W^{v,v'}_{\eta,\mathrm{ab}}(\vec{r},\vec{k}|\vec{k}') \Big] d^3k d^3k', \quad (3.1)$$

where $W^{v,v'}_{\eta,\mathrm{em}}$ and $W^{v,v'}_{\eta,\mathrm{ab}}$ refer to the transition rate for phonon emission and absorption, respectively. Fig. 3.2 shows the power densities calculated from Joule-heating and energy loss rate due to inelastic phonon scattering along the symmetry axis of the investigated SiGe HBT. In fact, carriers receive energy from the high electric field at the collector-base junction, which can be described by the Joule-heating term, while they lose their energy via net phonon generation deep in the collector region. This result shows the spatial shift that carriers experience before releasing their energy to the lattice and clarifies the importance of longitudinal optical (LO) phonons in carrier-phonon interactions.

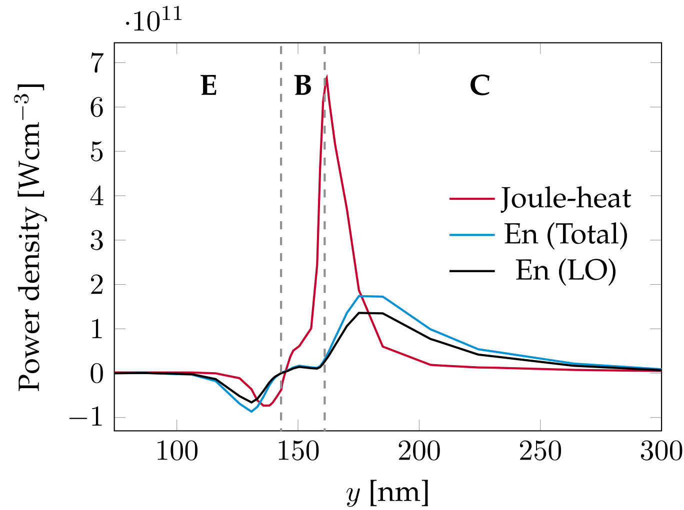

Figure 3.2: Spatial distribution of the power densities received and dissipated by carriers, which are calculated from Joule-heating and energy loss rate due to inelastic phonon scattering, respectively, across the symmetry axis of the HBT at $V_{\mathrm{BE}} = 0.9\,\mathrm{V}$ and $V_{\mathrm{CE}} = 1\,\mathrm{V}$.

In several previous works, the MC method was used to solve the BTE for electrons coupled with heat transport equations. The most elementary approach to consider heat conduction is the Fourier heat equation [44, 45], which is not valid in the submicron regime. Raleva *et al.* [46] and Vasileska *et al.* [47] used a system of energy balance equations for both optical and acoustic phonons derived from the corresponding phonon BTEs and coupled them with their electron MC simulator to investigate self-heating in silicon-on-insulator devices. Although this time-efficient approach can model the phonon bottleneck in thermal energy transport by distinguishing between optical and acoustic phonon temperatures, it cannot capture all microscopic features of non-equilibrium phonon transport due to the averaged phonon temperatures. More recently, Nghiêm *et al.* [48] introduced a more detailed electrothermal simulator, which solves the BTE for both electrons and phonons self-consistently while the feedback to the electron system is the effective temperature extracted from the phonon distribution function.

Despite remarkable advances in understanding physics of phonon transport with the aid of the MC method, the stochastic nature of this method can impede the calculation of parameters with very small or slow variations. To overcome this

problem, the BTE can be solved deterministically based on the SHE method [49]. In this regard, Ramonas *et al.* [50] have presented recently a deterministic approach for transport and noise calculations in a non-equilibrium bulk electron-phonon system.

In this work, we present a SHE method for the coupled BTEs of carriers and phonons under stationary conditions in a SiGe HBT. Since carriers lose their energy mainly by scattering with LO phonons, we solve phonon BTE only for the LO phonons (Sec. 3.3). In addition, energy balance equations for the averaged phonon temperatures are used and introduced in Sec. 3.4 for the other optical and acoustic phonon modes. The lattice thermal conductivity, which models heat conduction by acoustic phonons, is limited by alloy, impurity and size effects in nanoscale SiGe HBTs [51, 52]. These effects are also captured by analytical models for the lattice thermal conductivity, which are discussed in Sec. 3.5. With this electrothermal device simulator, temperature distribution in the 2-D SiGe HBT is calculated and junction temperature is calibrated to match with measurement data (Sec. 3.6). Consistency of the extracted junction temperature from the simulated DC characteristics with the value obtained from the temperature profile around the EB junction is a verification for the analytical approach used to extract the thermal resistance of the device by experiments (Sec. 3.8). Furthermore, the impacts of hot LO phonons and self-heating on steady-state carrier transport are shown in Sec. 3.7 and Sec. 3.9, respectively.

3.3 BTEs for the coupled carrier-phonon system

To investigate non-equilibrium effects for the carrier-phonon system in bipolar transistors, a coupled set of BTEs for electrons, holes, and phonons, has to be solved self-consistently. Since the projection of the full-band carrier BTE onto spherical harmonics has been discussed in chapter 2, here, we just describe the expansion of the coupling terms in the carrier and phonon BTEs.

3.3.1 Coupling term in carrier BTEs

We consider a non-equilibrium phonon distribution function $n(\vec{r},\vec{q})$, defined on the phonon wave vector $\vec{q}$, only for LO phonons. For the other phonon modes, equilibrium distribution functions, which are evaluated at averaged phonon temperatures of the optical $T_{\mathrm{op}}(\vec{r})$ and acoustic $T_{\mathrm{ac}}(\vec{r})$ phonon branches, are assumed. Under these assumptions, the BTE for the carrier distribution function is written as

$$L\{f\} = Q^{LO}\{f,n\} + S\{f,T_{\mathrm{op}},T_{\mathrm{ac}}\}, \tag{3.2}$$

where $Q^{LO}\{f,n\}$ denotes the scattering operator for inelastic interactions of carriers with LO phonons, and $S\{f,T_{\mathrm{op}},T_{\mathrm{ac}}\}$ stands for the scattering operator of all other scattering mechanisms. The momentum dependent transition rate for the inelastic carrier-LO phonon scattering is given by

$$W^{v,v'}(\vec{r},\vec{k},\vec{k}',n) = C_0(\vec{r})\Big[n(\vec{r},\vec{q}) + \frac{1}{2} \mp \frac{1}{2}\Big]\delta\big(\varepsilon(\vec{k}) - \varepsilon(\vec{k}') \mp \hbar\omega\big), \tag{3.3}$$

where $C_0(\vec{r})$ is the interaction constant, and the upper sign refers to phonon absorption and the lower one to phonon emission. After expansion of the phonon distribution function with spherical harmonics, $n(\vec{r},\vec{q}) = \sum_{s,p} n_{s,p}(\vec{r},q)Y_{s,p}(\theta_q,\phi_q)$, the projection of the in- and out-scattering terms on an equienergy surface for the absorption of LO phonon yields

$$Q_{\mathrm{in}}^{l,m}(\vec{r},\varepsilon) = V_0C_0(\vec{r})\sum_{v'}\sum_{l',m'}\sum_{s,p} n_{s,p}(\vec{r},q)f_{l',m'}^{v'}(\vec{r},\varepsilon-\hbar\omega)Z(\varepsilon-\hbar\omega)Z(\varepsilon)$$
$$\int\!\!\int Y_{l,m}(\theta,\phi)Y_{l',m'}(\theta',\phi')Y_{s,p}(\theta_q,\phi_q)d\Omega' d\Omega, \tag{3.4}$$

$$Q_{\mathrm{out}}^{l,m}(\vec{r},\varepsilon) = V_0C_0(\vec{r})\sum_{v'}\sum_{l',m'}\sum_{s,p} n_{s,p}(\vec{r},q)f_{l',m'}^{v}(\vec{r},\varepsilon)Z(\varepsilon+\hbar\omega)Z(\varepsilon)$$
$$\int\!\!\int Y_{l,m}(\theta,\phi)Y_{l',m'}(\theta',\phi')Y_{s,p}(\theta_q,\phi_q)d\Omega' d\Omega. \tag{3.5}$$

The spherical coordinates in the q-space have to be expressed based on the modulus of the wave vector and the angles of the initial and final carrier states by exploit-

ing the momentum conservation rule, $\vec{k}' = \vec{k} \pm \vec{q}$. Therefore, we use the addition theorem for spherical harmonics, which can be reformulated as [53]

$$M(q) = M(\varepsilon, \varepsilon', \theta_{kk'}) = \sum_{i,h} M_i(\varepsilon, \varepsilon') Y_{i,h}(\theta_k, \varphi_k) Y_{i,h}(\theta_{k'}, \varphi_{k'}), \tag{3.6}$$

in which

$$M_i(\varepsilon, \varepsilon') = 2\pi \int_{-1}^{1} M^{\gamma}(\varepsilon, \varepsilon', \theta_{kk'}) P_i(\cos\theta_{kk'}) d(\cos\theta_{kk'}). \tag{3.7}$$

As a result, by assuming $M(q) = n_{0,0}(\vec{r}, q)$ for the zero-th spherical harmonic of the phonon distribution function, we obtain

$$Q_{\text{in}}^{l,m}(\vec{r}, \varepsilon) = V_0 C_0(\vec{r}) Y_{0,0} \sum_{v'} M_l(\vec{r}, \varepsilon, \varepsilon') f_{l,m}^{v'}(\vec{r}, \varepsilon - \hbar\omega) Z(\varepsilon - \hbar\omega) Z(\varepsilon), \tag{3.8}$$

$$Q_{\text{out}}^{l,m}(\vec{r}, \varepsilon) = V_0 C_0(\vec{r}) Y_{0,0} \sum_{v'} M_0(\vec{r}, \varepsilon, \varepsilon') f_{l,m}^{v}(\vec{r}, \varepsilon) Z(\varepsilon + \hbar\omega) Z(\varepsilon), \tag{3.9}$$

where $M_l(\vec{r}, \varepsilon, \varepsilon')$ is expressed as

$$M_l(\vec{r}, \varepsilon, \varepsilon') = 2\pi \int_{-1}^{1} n_{0,0}\Big(\vec{r}, \sqrt{k^2(\varepsilon) + k^2(\varepsilon') - 2k(\varepsilon)k(\varepsilon')\cos(x)}\Big) P_l(x) dx. \tag{3.10}$$

These expansions result in a balance equation for the coefficients of the carrier distribution function, which is discretized over energy and real space as described in 2.10.

3.3.2 BTE for LO phonons

The strong carrier-LO phonon scattering can lead to a significant deviation in the distribution function of the LO phonons from the Bose-Einstein distribution function at equilibrium. The kinetic equation for the LO phonons is given by

$$G^c\{n, f\} + \left(\frac{\partial n}{\partial t}\right)_{\text{col}} = 0, \tag{3.11}$$

where $G^c\{n,f\}$ is the phonon generation term, and $\left(\frac{\partial n}{\partial t}\right)_{\mathrm{col}}$ represents the phonon-phonon scattering term, which is modeled within the relaxation time approximation as

$$\left(\frac{\partial n}{\partial t}\right)_{\mathrm{col}} = \frac{n(\vec{r},\vec{q}) - n_{\mathrm{eq}}(T_L)}{\tau_{\mathrm{op}}}, \tag{3.12}$$

where τ_{op} is the relaxation time attributed to the interaction between optical and acoustic phonons, and $n_{\mathrm{eq}}(T_L)$ is the equilibrium phonon distribution function evaluated at the lattice temperature $T_L(\vec{r})$. Expansion into spherical harmonics for the phonon-phonon scattering term yields

$$\left(\frac{\partial n}{\partial t}\right)^{s,p}_{\mathrm{col}}(\vec{r},q) = \frac{n_{s,p}(\vec{r},q) - Y^{-1}_{0,0}\delta_{s,0}\delta_{p,0}n_{\mathrm{eq}}(T_L)}{\tau_{\mathrm{op}}}. \tag{3.13}$$

The generation term, which models the energy exchange with carriers via either phonon creation (emission) or annihilation (absorption), is given by

$$G^c\{n,f\} = \frac{2V_0}{(2\pi)^3}\sum_v \int \Big[W^{v,v}_{ab}(\vec{r},\vec{k},\vec{q},n) - W^{v,v}_{em}(\vec{r},\vec{k},\vec{q},n)\Big] f^v(\vec{r},\vec{k})d^3k. \tag{3.14}$$

To eliminate the delta function in the transition rate (eq. 3.3), we have to establish a relation between ε and q. In the case of the full-band structure, which is used in this work, we apply the invertible dispersion relation and perform linear interpolation for the modulus of the carrier wave vectors at each energy step ε_i as

$$k(\varepsilon) = a_i\big(\varepsilon - \varepsilon_i\big) + b_i, \tag{3.15}$$

$$k'(\varepsilon') = a'_i\big(\varepsilon' - (\varepsilon_i \pm \hbar\omega)\big) + b'_i. \tag{3.16}$$

Consequently, the spherical expansion for the absorption part of the generation term yields

$$G^{s,p}_{ab}(\vec{r},q) = 2V_0C_0(\vec{r})\sum_v\sum_{s',p'}\sum_{l,m}\int_{\varepsilon_{\min}} f^v_{l,m}(\vec{r},\varepsilon)Z^v(\varepsilon)Z_{ph}(q)I_{l,m,s,p,s',p'}(\vec{r},\varepsilon,q)d\varepsilon, \tag{3.17}$$

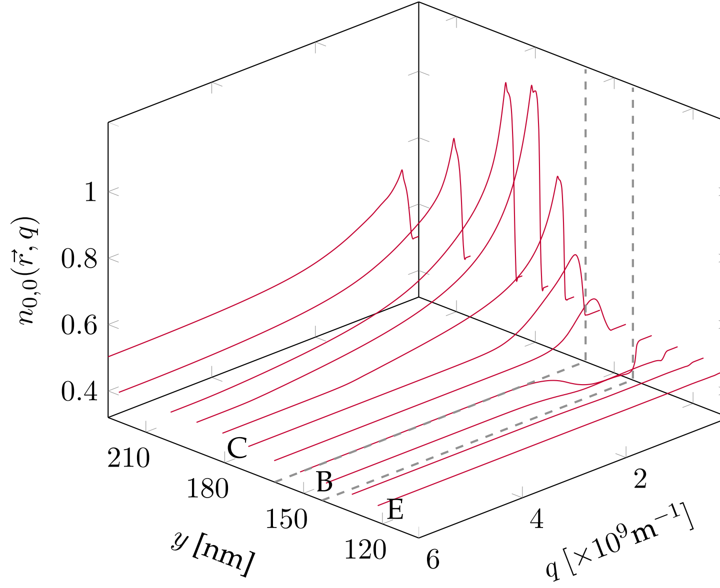

Figure 3.3: Zeroth order harmonic of the LO phonon distribution function along the symmetry axis of the investigated HBT at $V_{\text{BE}} = 0.9\,\text{V}$ and $V_{\text{CE}} = 1\,\text{V}$.

with

$$I_{l,m,s,p,s',p'}(\vec{r}, \varepsilon, q) = 2\pi \frac{a_i' k'}{kq} n_{s',p'}(\vec{r}, q) P_l\left(\frac{k'^2 - (k^2 + q^2)}{2kq}\right)$$
$$\int Y_{l,m}(\theta_q, \varphi_q) Y_{s,p}(\theta_q, \phi_q) Y_{s',p'}(\theta_q, \phi_q) d\Omega_q, \tag{3.18}$$

in which $Z_{ph}(q) = q^2/(2\pi)^3$ is the density of states for phonons, and $\varepsilon_{\min}$ is determined at each q value from the condition of $|\cos\theta_{kq}| \leq 1$. Similar expressions are obtained for the emission term, which provide a direct solution for the phonon BTE coupled with the BTEs of carriers. Fig. 3.3 shows the zeroth-order harmonic of the LO phonon distribution function along the symmetry axis of the SiGe HBT. The high rate of LO phonon generation in the collector region (Fig. 3.2) leads to a strong deviation in the LO phonon distribution function with respect to the equilibrium value evaluated at the lattice temperature.

3.4 Energy balance equations

Using the first law of thermodynamics, equations of phonon energy conservation can be derived from the corresponding phonon BTEs. These energy balance equations for the optical and acoustic phonon branches are written, respectively, as [54, 46]

$$\frac{\partial W_{\mathrm{op}}}{\partial t} = \left(\frac{\partial W_{c-\mathrm{op}}}{\partial t}\right)_{\mathrm{col}} - \left(\frac{\partial W_{\mathrm{op-ac}}}{\partial t}\right)_{\mathrm{col}}, \tag{3.19}$$

$$\frac{\partial W_{\mathrm{ac}}}{\partial t} = \nabla \cdot (k_{\mathrm{ac}} \nabla T_{\mathrm{ac}}) + \left(\frac{\partial W_{c-\mathrm{ac}}}{\partial t}\right)_{\mathrm{col}} + \left(\frac{\partial W_{\mathrm{op-ac}}}{\partial t}\right)_{\mathrm{col}}, \tag{3.20}$$

where k_{ac} is the lattice thermal conductivity, W_{op} and W_{ac} are the optical and acoustic phonon energy densities, respectively, which are related to their corresponding temperatures with optical phonon heat capacity C_{op}, and acoustic phonon heat capacity C_{ac}, as

$$dW_{\mathrm{op}} = C_{\mathrm{op}} dT_{\mathrm{op}}, \quad dW_{\mathrm{ac}} = C_{\mathrm{ac}} dT_{\mathrm{ac}}. \tag{3.21}$$

The phonon-phonon interaction term, which describes the decay of optical to acoustic phonons, is written in the relaxation time approximation

$$\left(\frac{\partial W_{\mathrm{op-ac}}}{\partial t}\right)_{\mathrm{col}} = C_{\mathrm{op}} \left(\frac{T_{\mathrm{op}} - T_{\mathrm{ac}}}{\tau_{\mathrm{op}}}\right). \tag{3.22}$$

To model heat generation accurately, carrier-phonon interactions are written as the energy loss rate due to inelastic phonon scattering separately for the optical and acoustic modes as

$$\left(\frac{\partial W_{c-\mathrm{op}}}{\partial t}\right)_{\mathrm{col}} = \frac{2}{(2\pi)^3} \sum_{v} \sum_{\eta:\mathrm{op}} \int \hbar\omega_\eta f^v(r,\vec{k}) \big[S^v_{\eta,\mathrm{em}}(r,\vec{k},T_{\mathrm{op}}) - S^v_{\eta,\mathrm{ab}}(r,\vec{k},T_{\mathrm{op}})\big] d^3k, \tag{3.23}$$

$$\left(\frac{\partial W_{c-\mathrm{ac}}}{\partial t}\right)_{\mathrm{col}} = \frac{2}{(2\pi)^3} \sum_{v} \sum_{\eta:\mathrm{ac}} \int \hbar\omega_\eta f^v(r,\vec{k}) \big[S^v_{\eta,\mathrm{em}}(r,\vec{k},T_{\mathrm{ac}}) - S^v_{\eta,\mathrm{ab}}(r,\vec{k},T_{\mathrm{ac}})\big] d^3k. \tag{3.24}$$

In this simulation approach, non-equilibrium effects for the other optical phonon modes are described by the average phonon temperature $T_{\mathrm{op}}(\vec{r})$. Furthermore, the acoustic phonon temperature $T_{\mathrm{ac}}(\vec{r})$ is a good approximation of the lattice temperature [46], which is required for the equilibrium distribution function of the LO phonons in equation (3.12).

3.5 Thermal conductivity

Heat conduction in silicon is dominated by acoustic phonon transport and the lattice thermal conductivity is the main parameter that models this effect. Using the relaxation time approximation, an analytical expression for the thermal conductivity can be derived from the BTE of the acoustic phonons. By assumption of a linear dispersion relation for the acoustic phonon modes, $\omega_q = \nu_g q$, and an average group velocity $\nu_g^{-2} = (2/3)c_T^{-2} + (1/3)c_L^{-2}$ based on the sound velocities of the transverse and longitudinal acoustic phonons, c_T and c_L, the thermal conductivity is written as [55, 51, 52]:

$$k = \frac{\hbar^2 \nu_g^4}{2\pi^2 k_B T_L^2} \int_0^{\frac{\omega_c}{\nu_g}} \tau(q, T_L) q^4 \frac{\exp(X_q)}{\left[\exp(X_q) - 1\right]^2} dq, \tag{3.25}$$

where $X_q = \hbar \nu_g q / k_B T_L$, ω_c is the phonon cut-off frequency, and $\tau(q, T_L)$ is the total relaxation time for acoustic phonons. The bulk thermal conductivities of pure Si and Ge is calculated by accounting for the umklapp scattering mechanism as k_{Si} = 148 $\mathrm{Wm}^{-1}\mathrm{K}^{-1}$ and k_{Ge} = 60 $\mathrm{Wm}^{-1}\mathrm{K}^{-1}$, respectively.

The thermal conductivity of each layer in a semiconductor device is degraded compared to the bulk value due to phonon scattering mechanisms [56], which are illustrated in Fig 3.4. In a SiGe HBT, heat conduction is dramatically reduced due to Ge content, doping profile, and size effects. The thermal conductivity of a SiGe alloy as a function of the Ge mole fraction is given by [57]

$$k_{\mathrm{SiGe}}(\vec{r}) = \left[\frac{1 - x_{\mathrm{Ge}}(\vec{r})}{k_{\mathrm{Si}}} + \frac{x_{\mathrm{Ge}}(\vec{r})}{k_{\mathrm{Ge}}} + \frac{\left(1 - x_{\mathrm{Ge}}(\vec{r})\right) x_{\mathrm{Ge}}(\vec{r})}{C_k}\right]^{-1}, \tag{3.26}$$

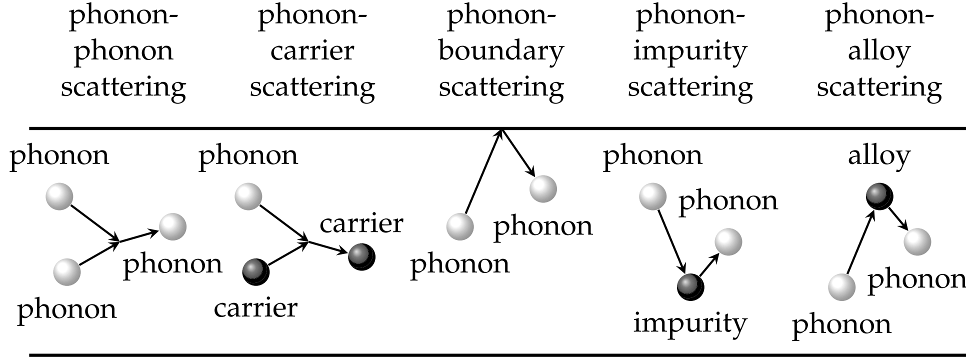

Figure 3.4: Acoustic phonon scattering mechanisms result in a thermal conductivity reduction in device layers.

where C_k = 2.8 $\mathrm{Wm^{-1}K^{-1}}$ is an empirical bowing factor.

A further reduction of the thermal conductivity in doped Si/SiGe is attributed to the enhanced phonon-impurity scattering. The variation of the thermal conductivity as a function of the dopant concentration is modeled using molecular dynamics results as [58]

$$k_{\mathrm{SiGe,doped}}(\vec{r}) = \frac{k_{\mathrm{SiGe}}(\vec{r})}{1 + A(N_{\mathrm{dop}(\vec{r})}/N_{\mathrm{norm}})^{\alpha}}, \tag{3.27}$$

where $N_{\mathrm{dop}}(\vec{r})$ is the doping concentration, N_{norm} = 10^{20} $\mathrm{cm^{-3}}$, and the fitting parameters are obtained as $A = 0.74186$, $\alpha = 0.7411$ for boron, and A = 1.698, α = 0.8251 for arsenic.

The heat propagation through narrow layers is also degraded due to phonon-boundary scattering. Therefore, the thermal conductivity of a narrow layer of width W, with the assumptions that the x-axis is perpendicular to the main heat flow and the confining surfaces of the layer are located at $x = 0$ and $x = W$, is given by [59]

$$k_{\mathrm{ac}}(\vec{r}) = k_{\mathrm{SiGe,doped}}(\vec{r}) \int_0^{\pi/2} \frac{3}{2} \sin^3\theta \Big[1 - \exp\big(\frac{-W}{2\lambda\cos\theta}\big) \times \cosh\big(\frac{W - 2x}{2\lambda\cos\theta}\big)\Big] d\theta, \tag{3.28}$$

where $\lambda = 290\,\mathrm{nm}$ is the mean free path for phonons, and $k_{\mathrm{ac}}(\vec{r})$ is the position

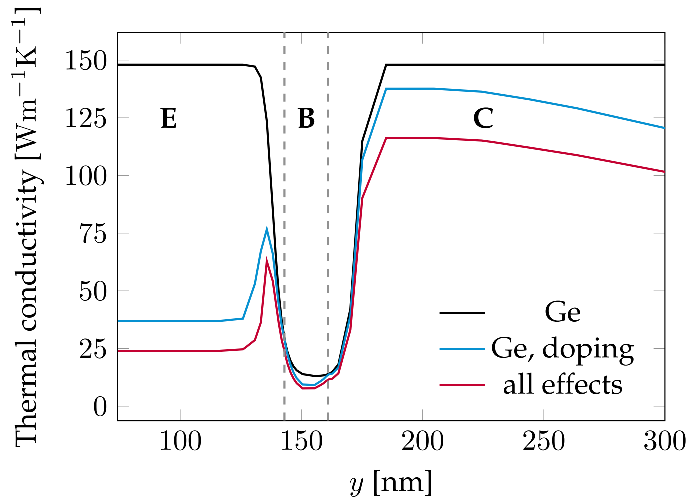

Figure 3.5: The effects of the Ge content, doping concentration, and boundary scattering in the reduction of the thermal conductivity along the symmetry axis of the investigated HBT at 300 K.

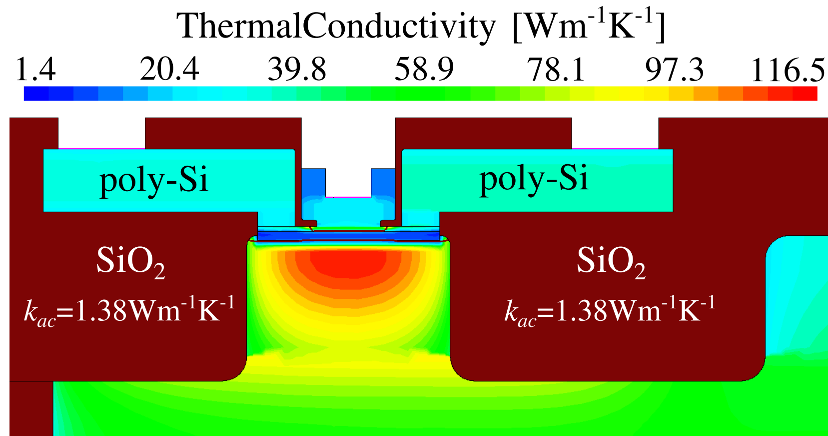

Figure 3.6: Thermal conductivity in the 2D SiGe HBT structure by considering the effect of Ge content, doping concentration, and boundary scattering at 300 K.

dependent lattice thermal conductivity, which takes all the suppressing effects into account.

Since the heat flow is mostly vertical in SiGe HBTs, the thermal conductivity reduction due to size effects is ascribed to the phonon scattering along the vertical boundaries of the Si layers confined by the shallow trench and EB spacer oxides. Instead, the horizontal heat spreading in the poly-silicon base regions is hampered

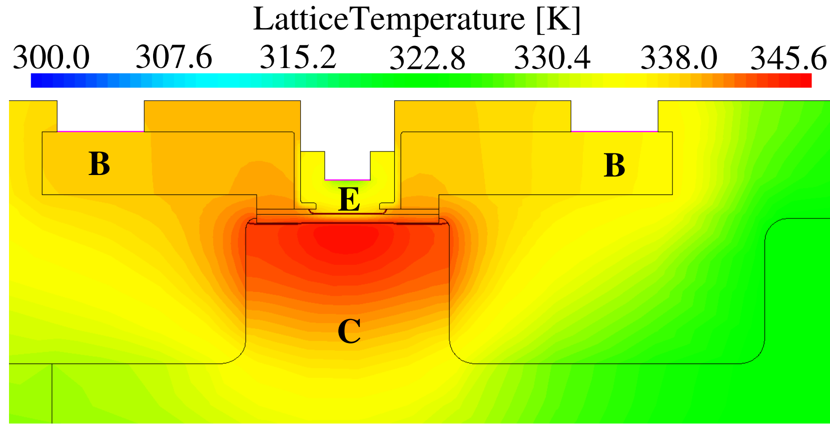

Figure 3.7: Self-consistent lattice temperature at $V_{\mathrm{BE}} = 0.9\,\mathrm{V}$ and $V_{\mathrm{CE}} = 1\,\mathrm{V}$.

by the scattering along the lateral boundaries. Fig. 3.5 shows the thermal conductivity along the symmetry axis of the investigated HBT, as obtained by only considering the impact of the Ge content, by accounting for both Ge and doping, and by concurrently including all the degrading effects. Fig. 3.6 depicts the thermal conductivity over the 2-D SiGe HBT by taking into account the effect of Ge content, doping concentration and boundary scattering at 300 K.

3.6 Temperature distribution

Since simulation of a 3-D real space is too CPU intensive for the SHE solver, only a 2-D real space is used and some important parts of the structure, such as metal layers, are neglected. In order to account for these 3-D effects in our 2-D simulation, the thermal boundary conditions have to be modified to get a simulated average lattice temperature increase over the EB junction equal to the junction temperature extracted from measurements [60]. The extracted thermal resistance from measurements $R_{\mathrm{TH}} = 6800\,\mathrm{K/W}$ [41] leads to an increase of the corresponding junction temperature $\Delta T_j = 38.5\,\mathrm{K}$ at $V_{\mathrm{BE}} = 0.9\,\mathrm{V}$ and $V_{\mathrm{CE}} = 1\,\mathrm{V}$ with $I_C = 5.66\,\mathrm{mA}$. Therefore, a convective (Robin) boundary condition is applied at the emitter contact, which is defined as

$$\nabla T_{\mathrm{ac}}(\vec{r}) \cdot \vec{n} = \alpha\big(T_{\mathrm{ac}}(\vec{r}) - T_B\big), \tag{3.29}$$

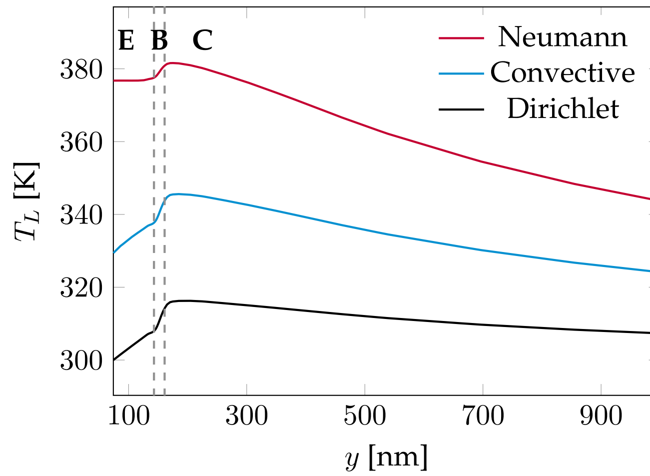

Figure 3.8: Lattice temperature profiles along the symmetry axis of the SiGe HBT with different temperature boundary conditions for the emitter contact at $V_{\mathrm{BE}} = 0.9\,\mathrm{V}$ and $V_{\mathrm{CE}} = 1\,\mathrm{V}$.

where $\vec{n}$ is the outward-pointing unit vector normal to the boundary, α is the heat transfer coefficient, and T_B is the ambient temperature. The heat transfer coefficient was tuned to obtain an average junction temperature increase of 38.5 K from the temperature distribution of simulations at the corresponding bias conditions. The self-consistent lattice temperature resulting from the energy balance equations is shown in Fig. 3.7. In this simulation, Neumann (adiabatic) boundary conditions are considered for artificial boundaries, the base and collector contacts, whereas the bulk contact at the bottom of the substrate is set to a constant temperature of 300 K.

It is noteworthy that choosing a Neumann boundary condition at the emitter contact disregards cooling effects due to the upward heat removal from the emitter [41] and overestimates the junction temperature by 80%. Fig. 3.8 shows the lattice temperature profiles along the symmetry axis of the HBT, with unrealistic Dirichlet boundary condition set to 300 K, overestimating Neumann boundary condition and calibrated convective boundary condition at the emitter contact.

3.7 Effect of hot LO phonons

In order to evaluate the impact of hot LO phonons and compare with the lattice temperature, an effective temperature is extracted from the non-equilibrium LO phonon distribution function. The high effective temperature for LO phonons shown in Fig. 3.9 refers to the so-called phonon energy bottleneck in thermal conduction. Since the temperature around the EB junction dominantly determines the impact of self-heating on the collector current [61], the equality of the lattice temperature and the effective LO phonon temperature at this junction clarifies the negligible effect of hot LO phonons on the collector current.

The large difference of the lattice and effective LO temperatures in the collector region might influence some electrical phenomena, such as II due to hot electrons, which occurs mainly deep in the collector region. To investigate this possibility, in a simulation with $V_{\mathrm{CB}} = 2\,\mathrm{V}$, which leads to a junction temperature increase of 50 K, the injected current due to electron impact ionization I_{II} was calculated. Although stronger phonon scattering due to hot LO phonons, which is obtained from the full electrothermal simulation, leads to a lower number of hot electrons, the reduction of the I_{II} at the same collector current due to temperature is just a few percents. Consequently, the impact of hot LO phonons on electron II is not very strong.

3.8 Thermal resistance extraction

In general, the experimental characterization of self-heating in bipolar transistors is performed indirectly, because the temperature within the nanoscale device cannot be measured (e.g. extraction of the thermal resistance based on DC measurements [39]). In order to assess the accuracy of this approach, we extend our thermal analysis to extract the thermal resistance from the simulated DC characteristics similar to the experimental extraction method. In a bipolar transistor operating in forward active mode, if the CB voltage V_{CB} and the emitter current I_E are limited to values sufficiently low to disregard II and high injection effects, the thermal

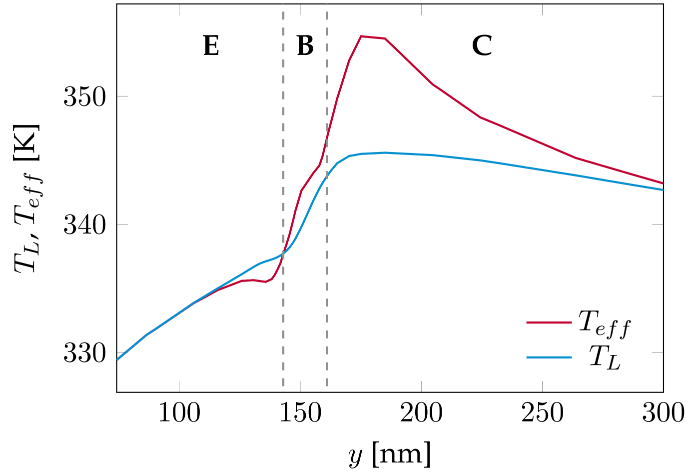

Figure 3.9: Lattice temperature and effective temperature for LO phonons across the symmetry axis of the HBT at $V_{\mathrm{BE}} = 0.9\,\mathrm{V}$ and $V_{\mathrm{CE}} = 1\,\mathrm{V}$.

resistance R_{TH} can be extracted from [39]

$$R_{\mathrm{TH}} = -\frac{\gamma}{(\gamma+1)I_E\phi}, \tag{3.30}$$

where ϕ is the temperature coefficient of the emitter-base voltage, and γ is the slope of the V_{BE}-V_{CB} characteristics at constant collector current. Therefore, using the thermal equivalent of the Ohm's law, the average temperature increase above ambient over the EB junction of the HBT is calculated as

$$\Delta T_j = R_{\mathrm{TH}} \times P_D, \tag{3.31}$$

where P_D is the total dissipated power through the device.

3.8.1 V_{BE} temperature coefficient

The base-emitter voltage temperature coefficient is a parameter, which describes the effect of temperature on the collector current. This coefficient is defined as the change of V_{BE} required to keep the collector current constant as the junction

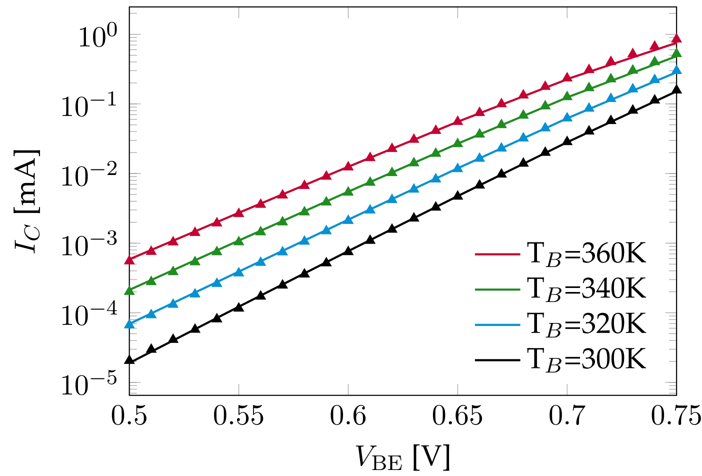

Figure 3.10: I_C-V_{BE} characteristics at $V_{\mathrm{CE}} = 0.6\,\mathrm{V}$ for different homogeneous temperatures. Solid lines show the isothermal simulation results at $T_B = 300,\ 320,\ 340,\ 360\,\mathrm{K}$ and the corresponding measurement results are shown by the symbols.

temperature changes

$$\phi = -\frac{\partial V_{\mathrm{BE}}}{\partial T_B}|_{I_C}. \tag{3.32}$$

Since in bipolar transistors I_C increases with temperature, ϕ is positive, where such a positive current-temperature feedback is easily explained by the increase of the intrinsic carrier concentration in the emitter with temperature [7].

Fig. 3.10 shows the collector current I_C calculated versus the base-emitter voltage V_{BE} of the HBT at different homogeneous temperatures, in comparison with experimental data measured under DC conditions at various thermo-chuck temperatures. In these voltage/current ranges self-heating can be disregarded, and the data were used for the calculation of the temperature coefficient.

3.8.2 V_{BE}- V_{CB} characteristic

It has been shown that the temperature rise of a forward-mode operating bipolar transistor at the EB junction is determined by the V_{BE}-V_{CB} characteristic [62]. In this regime, concurrent mechanisms of the Early effect (electrical feedback) and

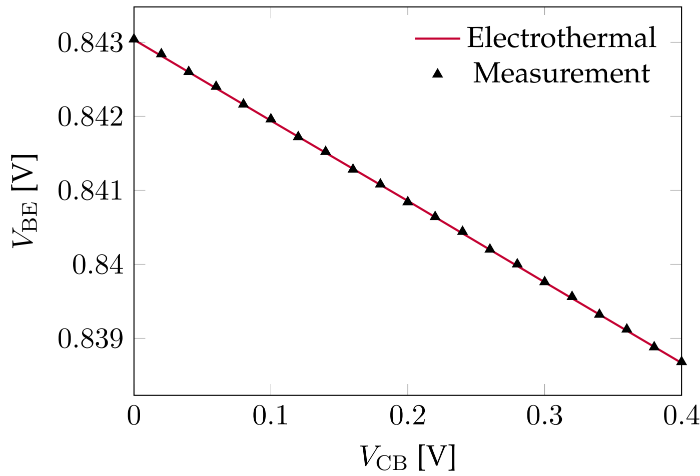

Figure 3.11: V_{BE}-V_{CB} characteristics at $I_E = 2\,\text{mA}$ from electrothermal simulation and measurement.

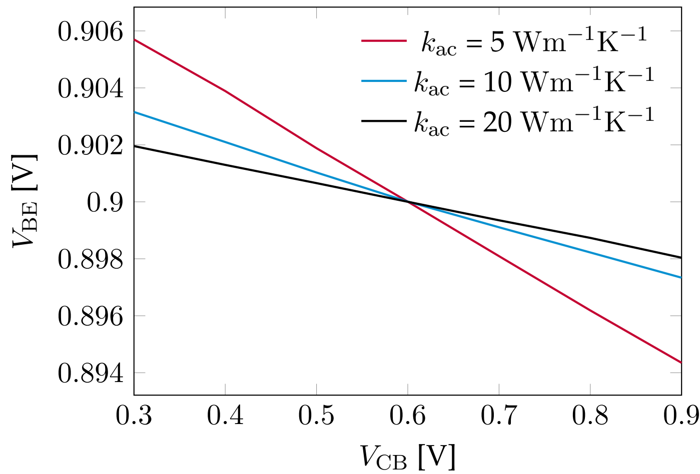

Figure 3.12: V_{BE}-V_{CB} characteristics at constant emitter current for different constant values of thermal conductivity in a 1-D SiGe HBT.

self-heating (thermal feedback) lead to an increase in I_C for increasing V_{CB} at fixed V_{BE}. If I_E is chosen high enough to have a dominant thermal feedback and still sufficiently low to avoid high injection and II, it can be shown that V_{BE} is a linear function of V_{CB} and the slope of the corresponding characteristic is given by

$$\gamma = \frac{\partial V_{BE}}{\partial V_{CB}}|_{I_E}. \tag{3.33}$$

Fig. 3.11 shows the V_{BE}-V_{CB} characteristics obtained from electrothermal SHE simulations in comparison to measurement data. Since the variation of V_{BE} with respect to V_{CB} for a constant I_{E} is very small, the extraction of the γ parameter could be troublesome with the MC method. Furthermore, we have shown that the slope of the V_{BE}-V_{CB} curve is determined by the thermal parameters of the device (Fig. 3.12); therefore, a self-consistent and deterministic electrothermal simulation is needed to evaluate the slope of this curve consistent with the lattice temperature distribution of the device.

Consequently, the extracted thermal resistance from electrothermal simulations matches with the value obtained from measurements, which confirms the consistency of the extracted junction temperature from the simulated DC characteristics with the average lattice temperature over the EB junction observed in the temperature profile shown in Fig. 3.9. This result asserts the accuracy of the analytical model on which the experimental procedure is based.

3.9 Impact of self-heating

Fig. 3.13 shows the effect of self-heating on the I_C-V_{BE} characteristics of the investigated SiGe HBT. The current increase due to self-heating obtained from electrothermal simulation is in a very good agreement with measurement results. Therefore, it is observed that the calibration of the heat transfer coefficient at the emitter contact for matching ΔT_j to measurement data at a certain bias point was enough to reach a good agreement in the operating regions, where self-heating plays an important role.

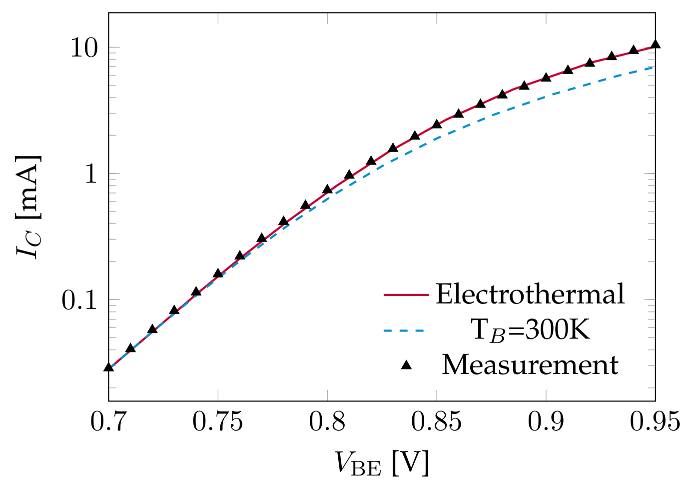

Figure 3.13: I_C-V_{BE} characteristics at $V_{\mathrm{CE}} = 1\,\mathrm{V}$ with and without including self-heating in comparison with measurement results.

Chapter 4

Hot Carrier Degradation

4.1 HCD in bipolar transistors

The evolutionary trend in frequency and noise performance of the SiGe HBTs has increased operating current density levels, while their breakdown occurs at lower voltages [63]. Due to these inevitable trade-offs for the performance optimization, devices are operated closer and even beyond the classical SOA boundaries. This might cause serious reliability issues for SiGe HBTs, which offer multiple applications ranging from high-performance analog circuits to high frequency applications and are exposed to electrical, thermal, and even irradiative stress [64].

HCD is the main reliability concern that strongly limits the lifetime of a SiGe HBT operated close to the SOA limit [65]. This degradation happens due to trap states generated by hot-carriers along the Si/SiO_2 interfaces. In general, imperfections at the oxide interface lead to silicon dangling bonds, which act as trap states and can capture electrons and holes. Thus, these dangling bonds are intentionally passivated by incorporating hydrogen atoms at the post-oxidation step (Fig. 4.1). However, hot carriers can supply enough energy to break the passivated Si-H bonds.A hot-carrier is a normal charge carrier, which is accelerated under a high electric field inside the device and attains significant kinetic energy (higher than 1.5 eV).

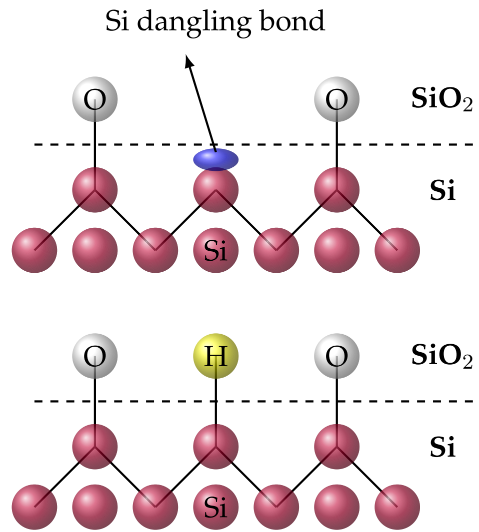

Figure 4.1: (top) Creation of Si dangling bonds at the Si/SiO_2 interface. (bottom) Passivation of the dangling bonds by incorporating hydrogen atoms and forming Si-H bonds.

Therefore, devices operating under high voltage bias conditions, which produce large electric fields, are susceptible to HCD phenomenon.

To sufficiently evaluate reliability, one has to stress the device under common operating conditions for a given length of time, and then measure the variations, which occur in the relevant device performance metrics. However, since degradation is a long-term process, conventional reliability stress tests for bipolar transistors are conducted under accelerated conditions consisting of high voltages, currents and temperatures, to invoke worst-case of stress and achieve significant hot-carrier effects in reasonable stress time. These standard techniques include three different scenarios: (1) high forward current stress [66], (2) reverse EB bias stress [67], and (3) mixed-mode (MM) stress [68]. High forward current stress is usually conducted under a current density near peak cut-off frequency at high temperatures (e.g., 140 C); in this case, degradation is generally associated with the electromigration-induced changes in the emitter contact and affects the collector current as well. In the reverse EB bias stress, the EB junction is reverse biased and carriers, which are injected due to BTBT, are further accelerated by high electric field at the CB junction and redirected to the oxide interfaces. The MM stress damage results from

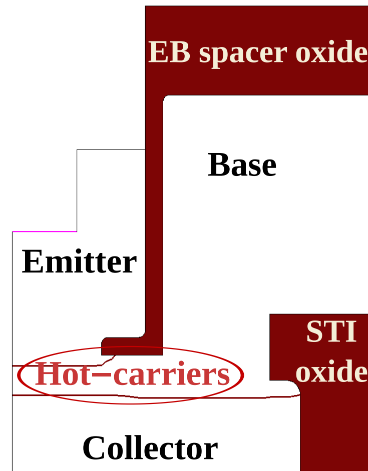

Figure 4.2: Schematic of a state-of-the-art SiGe HBT with the corresponding EB spacer and STI oxides.

the simultaneous application of high collector current density and high CB voltage which leads to interface traps formation at the oxide interfaces.

In high-performance HBTs, shallow trench isolation (STI) and deep trench isolation (DTI) schemes together with the EB spacer oxide have been used to reduce parasitics and leakage [38]. However, trap states resulting from the Si-H bond dissociation at the EB spacer oxide interface and STI oxide interface produce excess non-ideal base current via SRH recombination in the forward mode and reverse mode, respectively (Fig. 4.2). As a result, traps generated due to hot carriers along the EB spacer oxide interface degrade the main parameters of the device, such as current gain and noise figure [69]. Hence, a deeper insight into the microscopic mechanisms of trap generation and annihilation along the oxide interfaces of SiGe HBTs as well as their impact on the electrical characteristics is essential. In this work, to investigate HCD effects in bipolar transistors, we extend the distribution function based degradation model to account for both hot electrons and hot holes. Therefore, we use the solution of the coupled system of BTEs for electrons and holes to obtain the required energy distribution functions (EDFs) [70, 19].

In order to represent the complex dynamics of the trap generation and annihilation in HCD of bipolar transistors and negative-bias temperature-instability degrada-

tion of MOSFETs, two classes of models can be applied [71]: (1) the dispersive reaction-limited model, which proposes this idea that degradation is controlled by first-order reactions with widely distributed reaction rates, and (2) the reaction-diffusion model, which is based on this idea that diffusion of released hydrogen controls both degradation and resulting time-dependence. Therefore, we use a distribution function based degradation model to calculate the bond-breakage rate associated with both reaction-limited and reaction-diffusion models to describe HCD effects in a SiGe HBT (Sec. 4.2). Then, we show and discuss necessity and advantages of using a dispersive reaction-limited model. Simulation results for devices biased under stress conditions close to the SOA limit and reverse EB bias are presented in Sec. 4.3 and Sec. 4.4, respectively.

4.2 Degradation modelling

Hot-carrier-induced degradation in SiGe HBTs is ascribed to Si-H bond dissociation events along the oxide interfaces. Conventional approaches for physics-based modeling of HCD in bipolar transistors, which are based on the lucky electron model, are electric field driven [72, 73, 74, 75]. However, it has been demonstrated that the trap generation rate at the oxide interface depends only on the energy of the interacting charge carriers and is not determined by the electric field [76, 77]. Instead, another quantity called the acceleration integral (AI) has been identified, which can describe accurately the spatial distribution of the generated interface traps obtained from charge pumping measurement data [78, 79]. As a consequence, an energy driven paradigm based on the AI, which is calculated from the EDF of the carriers, has been developed to include both single- and multiple-carrier processes of the bond dissociation in the degradation analysis of the n-channel MOSFETs [80, 81, 82].

In the energy driven framework, the bond-breakage rate is determined by the interaction of the incident carriers with the passivated Si-H bond. The Si-H bond is modeled as a truncated harmonic oscillator characterized by a system of eigenstate energies [83], which is depicted in Fig. 4.3. Due to the large difference between

Figure 4.3: The energy configuration of the Si-H bond modeled as a truncated harmonic oscillator.

electron and proton masses, only a small portion of the carrier energy can be transferred directly to the hydrogen atom, which is not sufficient for hydrogen release. Instead, bond dissociation occurs via excitation of one of the bonding electrons to the transport state, which is known as the antibonding (AB) process. Consequently, an induced repulsive force detaches the hydrogen atom. The dissociation rate from the ith state of the Si-H bond with the energy E_i, which can be triggered by either a hot electron or a hot hole, is written as

$$R_{\mathrm{AB},i} = I^e_{\mathrm{AB},i} + I^h_{\mathrm{AB},i} + v_r \exp\Big(- \frac{E_a - d \cdot E_{\mathrm{ox}} - E_i}{k_B T_0} \Big), \tag{4.1}$$

where $I^e_{\mathrm{AB},i}$ and $I^h_{\mathrm{AB},i}$ are the AB AIs due to electrons and holes, respectively, v_r is an attempt frequency, and E_a is the bond-breakage activation energy, which is reduced due to the interaction of the bond dipole moment d with the oxide electric field E_{ox}. Moreover, to account for the fluctuations of the activation energy, we consider a Gaussian distribution with a mean value and standard deviation of $\langle E_a \rangle$ and σ_E, respectively. The AI for the AB process is given by [80]

$$I^{e/h}_{\mathrm{AB},i} = \sigma_0^{\mathrm{AB}} \int_{E_{\mathrm{th},i}}^{\infty} g^{e/h}(\vec{r}, E) v_g^{e/h}(E) [(E - E_{\mathrm{th},i})/E_{\mathrm{ref}}]^{p_{\mathrm{it}}} dE, \tag{4.2}$$

where $E_{\mathrm{th},i} = E_a - d \cdot E_{\mathrm{ox}} - E_i$ is the threshold energy for the ith level, σ_0^{AB} is the AB reaction cross section, $g^{e/h}(\vec{r}, E) = f^{e/h}(\vec{r}, E) \times Z^{\mathrm{e/h}}(E)$ is the EDF of the

carriers, $v_g^{e/h}(E)$ is the carrier group velocity, $p_{\text{it}} = 11$ is an empirical parameter, and $E_{\text{ref}} = 1\,\text{eV}$. Carriers with energies smaller than the threshold energy of the AB process still can cooperate in the bond-breakage procedure via multiple vibrational excitation (MVE) of the bond. The bond excitation and deexcitation rates between energy levels of a Si-H bond are written as

$$P_u = I^e_{\text{MVE}} + I^h_{\text{MVE}} + \omega_e \exp\Big(-\frac{\hbar\omega}{k_B T_0}\Big), \tag{4.3}$$

$$P_d = I^e_{\text{MVE}} + I^h_{\text{MVE}} + \omega_e, \tag{4.4}$$

where ω_e is the reciprocal phonon life-time, $\hbar\omega$ is the energy distance between oscillator energy levels, and the AI for the MVE process is defined as

$$I^{e/h}_{\text{MVE}} = \sigma_0^{\text{MVE}} \int_{\hbar\omega}^{\infty} g^{e/h}(\vec{r}, E) v_g^{e/h}(E)[(E - \hbar\omega)/E_{\text{ref}}]dE. \tag{4.5}$$

In an accumulative consideration of the MVE and AB mechanisms, one bonding electron can be firstly excited by several colder particles to an intermediate energy level, and then dissociated by a carrier with a relatively high energy. The total bond-breakage rate, which accounts for all possible superpositions of the AB and MVE mechanisms, is calculated as

$$R_a = \frac{1}{k} \sum_i R_{\text{AB},i} \left(\frac{P_u}{P_d}\right)^i, \tag{4.6}$$

where k is a normalization prefactor given by

$$k = \sum_i \left(\frac{P_u}{P_d}\right)^i. \tag{4.7}$$

4.2.1 Reaction-diffusion approach

In the reaction-diffusion approach, the rate equation for the generation and annihilation of the interface trap states is written as [84]

$$\frac{\partial N_{\text{it}}}{\partial t} = R_a(N_0 - N_{\text{it}}) - R_p N_{\text{it}} H_{\text{it}}, \tag{4.8}$$

where $N_{\rm it}$ is the interface trap density, N_0 is the initial density of the passivated Si-H bonds, R_p is the recovery rate, and $H_{\rm it}$ is the density of hydrogen at the oxide interface. The hydrogen released from the bond-breakage will diffuse away from the interface to the oxide, which can be described by a diffusion equation [84]. If the creation of trap states reaches quasi-equilibrium with the recovery of them, the time evolution of the trap states is controlled by diffusion of hydrogen. Therefore, the solution for the interface trap density, far below the saturation value N_0, can be approximated as [84, 74, 75]

$$N_{\rm it} \approx 1.16\sqrt{\frac{R_a N_0}{R_p}}\left(Dt\right)^{0.25}, \tag{4.9}$$

where D is the diffusion coefficient of hydrogen in oxide, and t is the stress time.

4.2.2 Dispersive reaction-limited approach

The rate equation for the interface trap states, which is used in the reaction-limited approach, reads

$$\frac{\partial N_{\rm it}}{\partial t} = R_a(N_0 - N_{\rm it}) - R_p N_{\rm it}^2. \tag{4.10}$$

In the reaction-limited approach, the power-law time dependence of the HCD results is attributed to the dispersion of the bond-breakage energy. The dispersive effect of E_a is incorporated by considering an energy grid in the range of $[\langle E_a\rangle - 3\sigma_E, \langle E_a\rangle + 3\sigma_E]$ and evaluating $N_{\rm it}$ for each discretization point. The interface trap density profile results from the combination of every single defect and is calculated by taking the average of $N_{\rm it}$ at each energy point weighted by the Gaussian distribution [80]. As a result, the activation energy parameters determine the fractional time-exponents observed in the excess base current degradation results [85].

	P1	P2	P3
$V_{\mathrm{CE}}[V]$	$1\ (< \mathrm{BV_{CEO}})$	$2\ (> \mathrm{BV_{CEO}})$	$3\ (> \mathrm{BV_{CEO}})$
$J_{\mathrm{C}}[\mathrm{mA}/\mu\mathrm{m}^2]$	10	5	1
$\Delta T_j[K]$	37	37	11

Table 4.1: Stress bias conditions and corresponding junction temperatures.

4.3 Stress condition close to the SOA limit

4.3.1 Stress conditions and DC measurements

The state-of-the-art toward-THz SiGe npn HBT fabricated by Infineon Technologies AG, which was studied in chapter 2, is used to perform long-term degradation analysis. The investigated device has a double collector configuration (CBEBC) with an effective emitter area $\mathrm{A_E} = 0.13{\times}9.93\ \mu\mathrm{m}^2$, and features peak cut-off/oscillation frequencies of $240/380$ GHz and breakdown voltages $\mathrm{BV_{CEO}}/\mathrm{BV_{CBO}} = 1.6/5.5$ V [86]. The test structure has ground-signal-ground pads configuration with emitter and substrate shorted. The transistors are biased in a common-emitter configuration. During the aging test, the packaged HBTs are fastened by a press system. To avoid parasitic oscillations on this specific press system, a π-type low-pass filter was added to the base and a choke coil to the collector.

The concurrent applications of a high CB voltage and a high collector current density, known as the accelerated MM stress conditions [68], represent an upper limit for degradation of the SiGe HBTs during RF operation [65]. However, as the main drawback they are far from typical operating conditions. Hence, to study the physics behind the long-term base current degradation under more practical operating conditions, three stress bias conditions P1, P2 and P3, along the border of the SOA as highlighted in Fig. 4.4 with respect to the output characteristics, have been designed to degrade the device up to 1000 h at 300 K.

The stress test was periodically interrupted to monitor the degradation by probing currents. For this purpose, a forward-mode Gummel plot is measured immediately

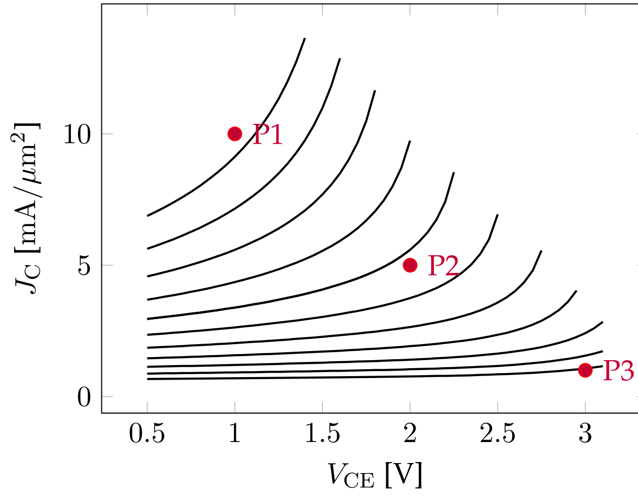

Figure 4.4: Output characteristics at given V_{BE} (lines) and chosen aging bias points (symbols) along the SOA limit.

after aging tests at 1, 3, 7, 24, 36, 48, 72, 120, 250, 500, 750, and 1000 h. The corresponding collector-emitter voltage V_{CE}, collector current density J_C, and junction-to-ambient temperature increase ΔT_j, which is obtained from the extracted thermal resistance $R_{TH} = 2850\,K/W$ [39], are summarized in Table I. It was observed that the device is negligibly affected by stress at P1, and P3 exhibits a higher base current degradation over time in comparison to P2.

4.3.2 Distribution function based analysis

As a first step of our analysis, the simulator was calibrated to reproduce the measured Gummel plot and I_B-V_{CE} characteristics of the fresh device (Sec. 2.11). The II generation rates at P3 due to electrons and holes are shown in Fig. 4.5. Under this stress condition, the injected electrons gain enough energy from the high electric field within the CB depletion region to initiate avalanche generation of electron-hole pairs via II. Fig. 4.5 shows that hot electrons, which cause II, are deep in the collector region, while hot holes responsible for II are mainly found in the base region. In addition, EDFs provide accurate information about the energy of the carriers, which participate in the degradation process. Fig. 4.6 depicts the EDFs for electrons and holes along the symmetry axis of the HBT with respect to kinetic

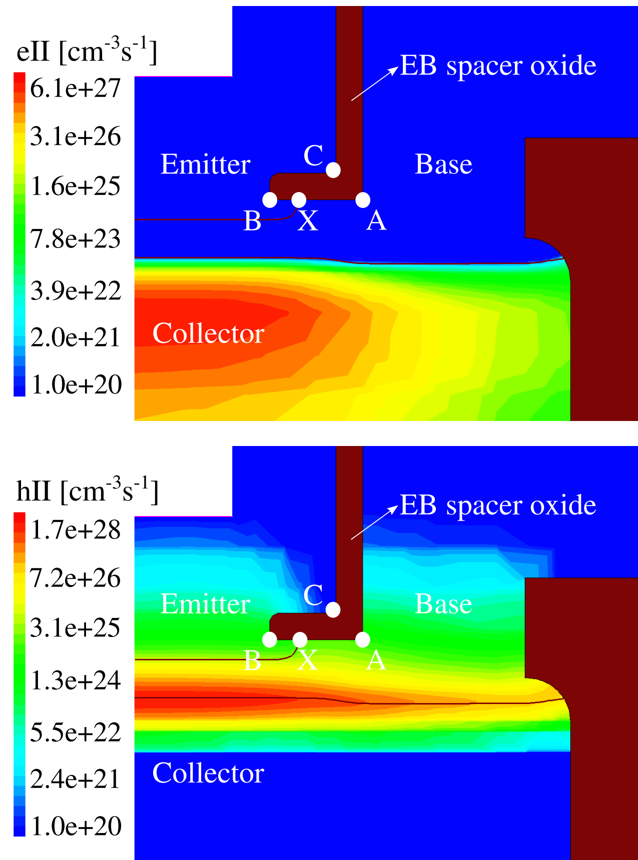

Figure 4.5: II generation rates in the SiGe HBT due to electrons (top), and holes (bottom) at P3.

energies. Due to the large electric field at the CB junction, electrons move to the collector region and become sufficiently energetic to initiate II. While primary holes, which move to the thin base layer, do not receive high energies, the holes generated by II due to hot electrons in the collector (Fig. 4.5 top) are further accelerated toward the base and gain a lot of energy. Owing to this high energy, some of the holes can shoot through the base into the emitter, where they still have a relatively large energy (Fig. 4.6 bottom). A certain fraction of these hot holes hits the EB spacer oxide interface finally leading to the Si-H bond-breakage.

It is only possible to capture this effect by a model, which resolves the dependence of the carriers on energy. Therefore, a DD or an HD model, in which the hole gas in the base is assumed to be close to equilibrium, can not directly describe

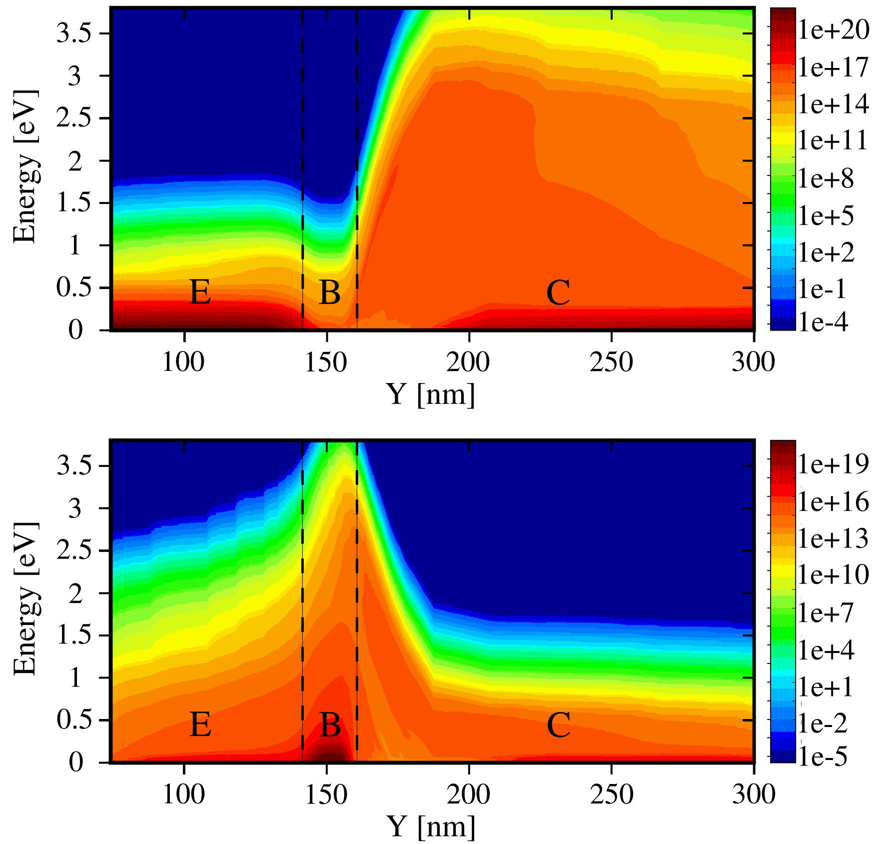

Figure 4.6: EDFs [$\mathrm{eV}^{-1}\mathrm{cm}^{-3}$] of electrons (top) and holes (bottom) along the symmetry axis of the HBT at P3.

the behavior of the hot holes, which are far from equilibrium. Inevitably, for a physics-based degradation analysis relying on these models, one has to calculate the probability of hot carrier creation via the lucky electron model. This calculation, which is based on the effective electric field, shows inaccurately that hot holes are accumulated at the CB junction. Then, the possibility that a hot carrier will traverse the entire distance to the oxide interface without any scattering has to be separately estimated [74].

Since the interface traps located within the EB SCR have the highest impact on the base current degradation due to recombination, the EDFs at the intersection of the EB junction and the oxide interface are compared in Fig. 4.7 for different stress conditions. The EDFs for electrons at P1 and P2, which exactly follow the

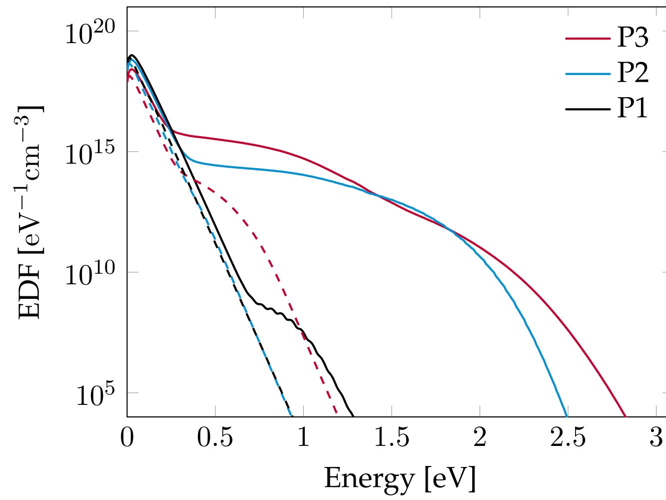

Figure 4.7: EDFs of electrons (dashed lines) and holes (solid lines) at the intersection of the EB junction and the EB spacer oxide interface (denoted by node X in Fig. 4.5).

equilibrium EDF, and at P3, with a low-energy hump, show the negligible role of electrons in the degradation process. Due to small V_{CE} in P1, even holes do not reach high energies, which explains the negligible degradation rate observed at P1. Moreover, the non-equilibrium tails of the hole EDFs at high energies for P2 and P3 reveal the significant role of hot holes in the degradation process under these biases, which was previously shown for conventional MM stress conditions in [87, 70]. However, our deterministic solver provides the possibility to accurately describe the microscopic effects of hot carriers along the EB spacer oxide interface in a realistic 2-D device structure and develop a practical physics-based degradation model to predict the resulting variation in the I-V characteristics.

4.3.3 Degradation results based on a dispersive reaction-limited model

Although cold carriers might also participate in the MVE process of the bond-breakage, hot carriers with energies greater than 1.5 eV have a much higher chance to dissociate the Si-H bonds directly [82]. Hence, we considered $\langle E_{\mathrm{a}}\rangle = 1.6\,\mathrm{eV}$ and a standard deviation of $\sigma_E = 0.2\,\mathrm{eV}$ for the activation energies of the bond-breakage to obtain the power-law time dependence of our measurement data under different

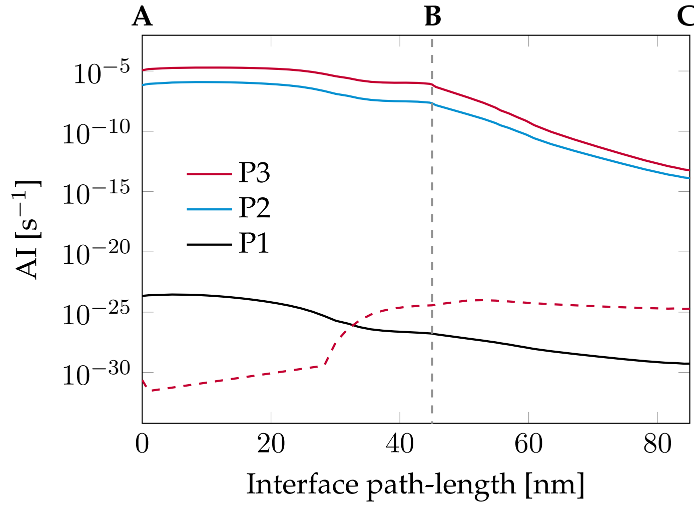

Figure 4.8: AB AIs for electrons (dashed lines) and holes (solid lines) along the EB spacer oxide interface from node A to C denoted in Fig. 4.5.

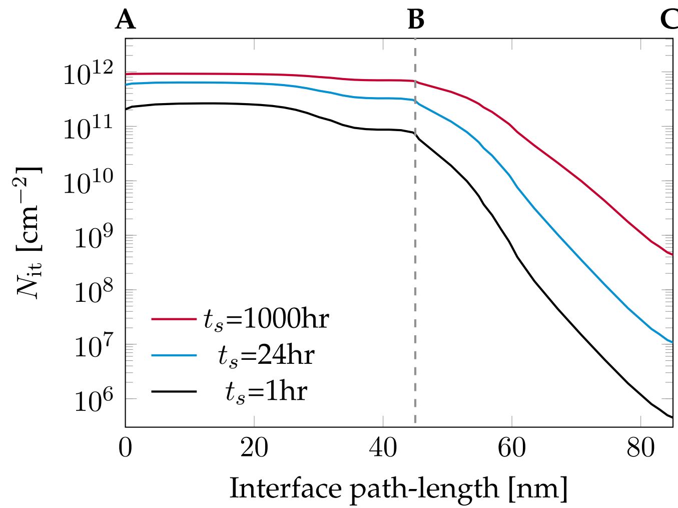

Figure 4.9: Trap densities generated at different stress time steps along the EB spacer oxide interface from node A to C denoted in Fig. 4.5 at P3.

stress bias conditions. The resulting AB AIs along the EB spacer oxide interface are shown in Fig. 4.8. As expected, the equilibrium electron EDFs at P1 and P2 lead to corresponding AIs, which are almost zero along the oxide interface. Furthermore, due to the low-energy humps in the EDFs of electrons at P3 and holes at P1, we obtain very small AIs for them. Consequently, the observed degradation currents at

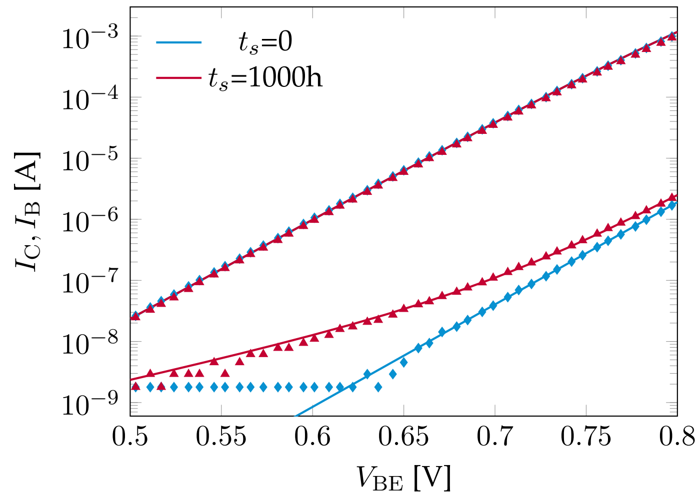

Figure 4.10: Gummel characteristics of the fresh and degraded SiGe HBT after 1000 h at P3 obtained from simulation (lines) and measurement (symbols).

P2 and P3 have to be attributed to hot holes with relatively high AB rates, in which the bigger AI at P3 compared to P2 explicitly explains the higher degradation rate under this stress condition.

The trap densities along the EB spacer oxide interface, which are dominantly generated by the AB process due to hot holes, are shown in Fig. 4.9 for several stress time steps. These results, calculated for $N_0 = 10^{12}\,\mathrm{cm}^{-2}$, show that the large variation of the AB AIs along the EB spacer oxide interface leads to a strong spatial non-uniformity in the N_{it} profile. Since we do not fit any charge pumping measurement data to extract the magnitude of the interface trap density, here we neglect any discussion about the parameters, which have identical impact on the base current degradation under different stress conditions. Hence, our reported parameters for the activation energy of the bond-breakage, which are in good agreement with those experimentally obtained [88, 89], are considered as the determining parameters to reproduce the dependence of the excess base current on the stress conditions and stress time.

These generated interface traps at the EB spacer oxide cause a non-ideal increase in the forward-mode base current via field-enhanced SRH recombination, which was described in Sec. 2.4. Fig. 4.10 represents the Gummel characteristics of the

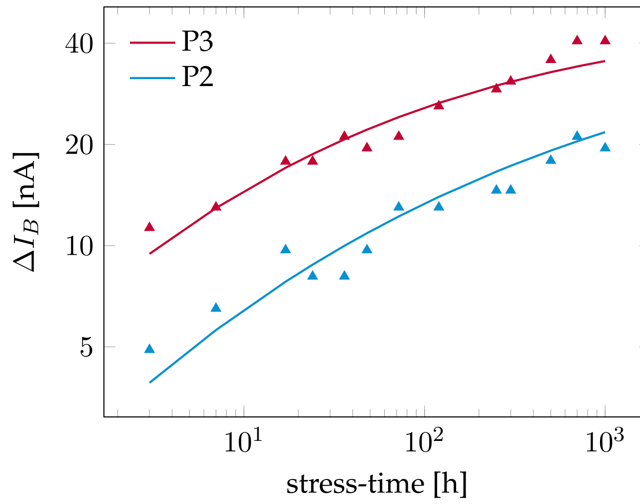

Figure 4.11: Excess base currents versus stress time obtained from simulation (lines) and measurement (symbols) at $V_{\mathrm{BE}} = 0.67\,\mathrm{V}$ and $V_{\mathrm{CB}} = 0\,\mathrm{V}$.

investigated SiGe HBT before and after 1000 h stress application at P3. Since the recombination process has no remarkable impact on the collector current, the resulting increase in the base current degrades the current gain of the transistor.

In order to evaluate the time dependence of the HCD effects, the excess base current $\Delta I_{\mathrm{B}}(t) = I_{\mathrm{B}}(t) - I_{\mathrm{B}}(0)$ at $V_{\mathrm{BE}} = 0.67\,\mathrm{V}$ has been extracted over stress time (Fig. 4.11). Although a wider range of measurement data is required for a general characterization of the HCD effects in bipolar transistors, a good agreement between our simulation results and measurements proves that our EDF-based degradation model can directly explain the time dynamics of the HCD results together with their dependence on the stress bias conditions.

4.3.4 Degradation results based on a reaction-diffusion model

To capture the dependence of the HCD results on the stress bias conditions with a reaction-diffusion approach, we obtained $\langle E_{\mathrm{a}} \rangle = 1.5\,\mathrm{eV}$ and a standard deviation of $\sigma_E = 0.05\,\mathrm{eV}$ for the activation energies, and calculated the corresponding bond-breakage rates. Fig. 4.12 shows the interface trap densities, the peak value of which is much smaller than our assumed saturation value $N_0 = 10^{-12}\,\mathrm{cm}^{-2}$; hence,

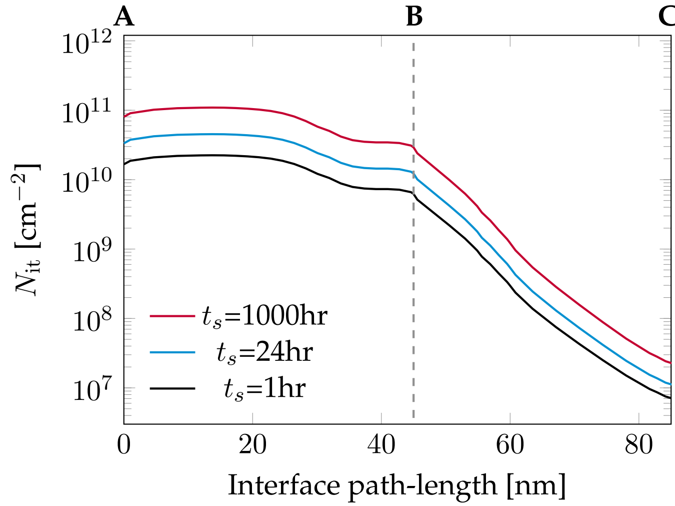

Figure 4.12: Trap densities obtained from the reaction-diffusion approach at different stress time steps along the EB spacer oxide interface from node A to C denoted in Fig. 4.5 at P3.

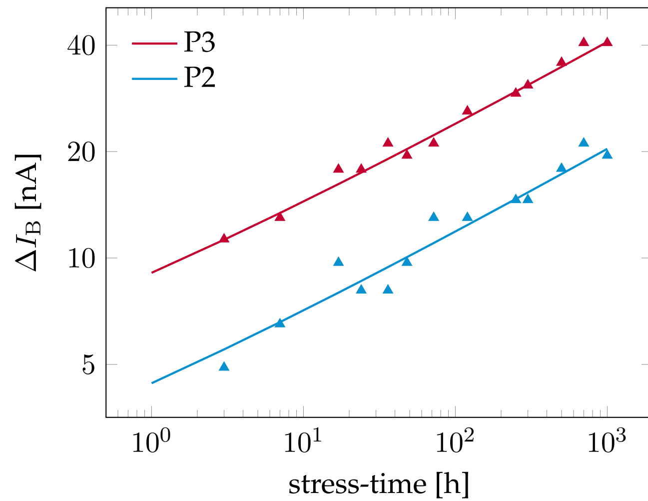

Figure 4.13: Excess base currents versus stress time obtained from the reaction-diffsusion approach (lines) and measurement (symbols) at $V_{\mathrm{BE}} = 0.67\,\mathrm{V}$ and $V_{\mathrm{CB}} = 0\,\mathrm{V}$.

we could safely apply the approximation in Eq. 4.9. Since our excess base currents from measurement grow exactly with $t^{0.25}$, we just consider the conventional approach for the hydrogen diffusion-controlled mechanism which leads to Eq. 4.9. A very good agreement with measurements proves that our EDF-based degradation

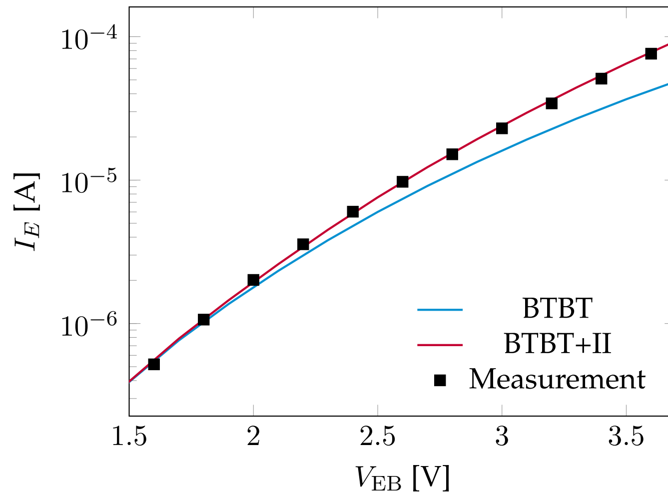

Figure 4.14: I_E-V_{EB} characteristic of a SiGe HBT obtained from simulations (lines) with only considering BTBT and considering both BTBT and II, and measurement (symbols).

is also capable to be applied in the commonly used reaction-diffusion approach to explain macroscopic HCD results. However, this approach has two main problems: (1) it has been shown that this approach cannot explain the measurement data in MOSFETs at the microscopic level [71], (2) although there are some discussions about generalization [90] of the reaction-diffusion approach, one has to be always aware of the time-slope of measurements and then decide for the selection of the process and the model of the hydrogen diffusion. Hence, this approach can only empirically explain the time-dependence of the HCD results, while the dispersive reaction-limited method could explain it based on some physical parameters, which have been experimentally verified.

4.4 Reverse EB bias stress condition

Very high reverse bias application, specially at the EB junction, can generate electrons and holes due to BTBT. These generated charge carriers gain high energies from the very high electric field and produce secondary electrons and holes due to impact ionization. Fig. 4.14 shows the reverse I_E-V_{EB} characteristic of a SiGe HBT

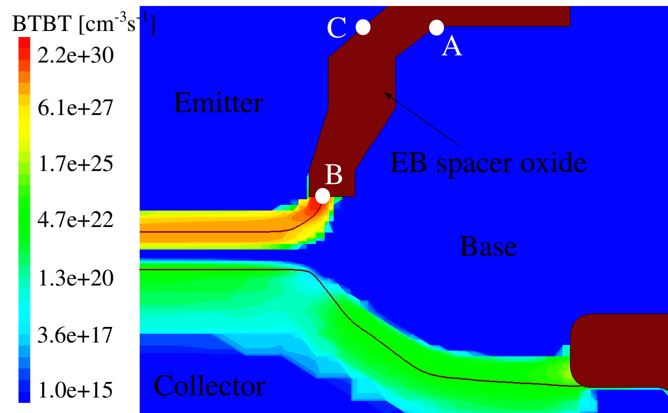

Figure 4.15: BTBT generation rates in the SiGe HBT at $V_{\text{EB}} = 3\,\text{V}$ and $V_{\text{CB}} = 3\,\text{V}$.

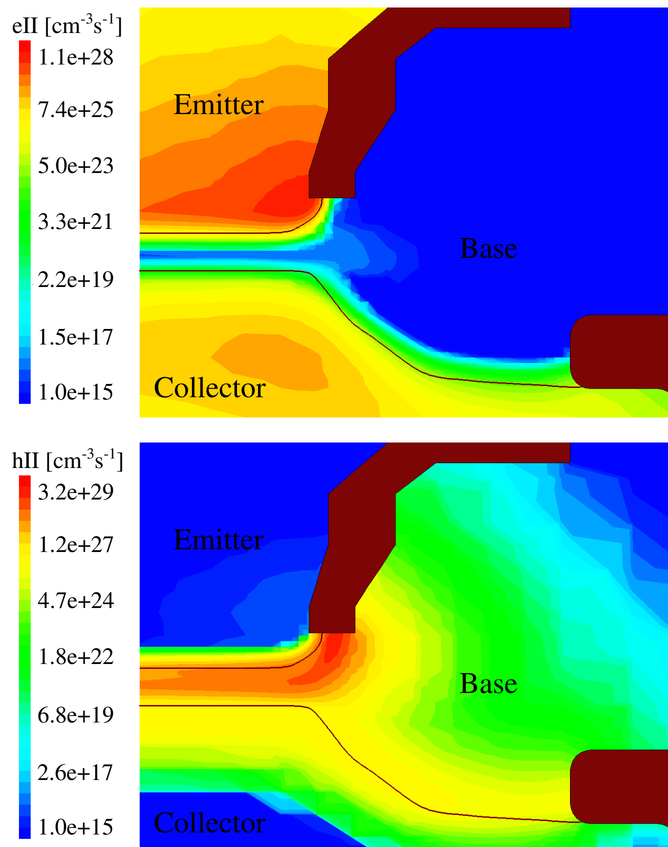

Figure 4.16: II generation rates in the SiGe HBT due to electrons (top), and holes (bottom) at $V_{\text{EB}} = 3\,\text{V}$ and $V_{\text{CB}} = 3\,\text{V}$.

compared to measurement data. The corresponding generation rate due to local

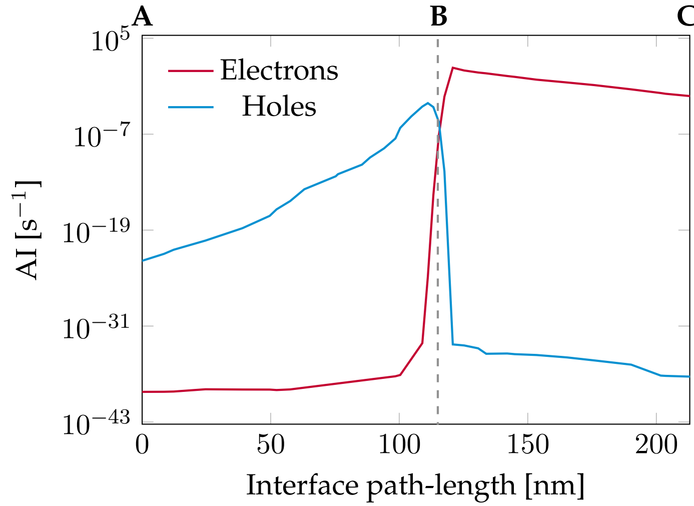

Figure 4.17: AB AIs for electrons and holes along the EB spacer oxide interface from node A to C denoted in Fig. 4.15 at $V_{\text{EB}} = 3\,\text{V}$ and $V_{\text{CB}} = 3\,\text{V}$.

BTBT is shown in Fig. 4.15, and Fig. 4.16 shows II rates due to high energy electrons and holes, separately. The generated electrons due to BTBT are accelerated toward the emitter, whereas generated holes move in parallel with and adjacent to the oxide interface toward the base region. These high energy carriers generate secondary electron-hole pair due to II (Fig. 4.16).

The AB AIs shown in Fig. 4.17 give us a quantitative description of the hot carriers, which participate in the reverse EB bias degradation procedure. These AIs show that despite a much higher rate of electrons impinging on the interface, around the EB junction (node B), where the trap generation has the highest impact, hot holes are also important. Therefore, it is concluded that in reverse EB bias stress mode, there is a competition between hot electrons and hot holes to damage the oxide interface and the effect of both of them has to be taken into account. The resulting trap densities along the EB spacer oxide interface are shown in Fig. 4.18 for different stress time steps. The Gummel plot of this degraded SiGe HBT after 100 h of stress at $V_{\text{EB}} = 3\,\text{V}$ is shown in Fig. 4.19.

Although we could get a very good matching for the base current degradation under reverse EB bias stress compared to measurements, it has to be mentioned

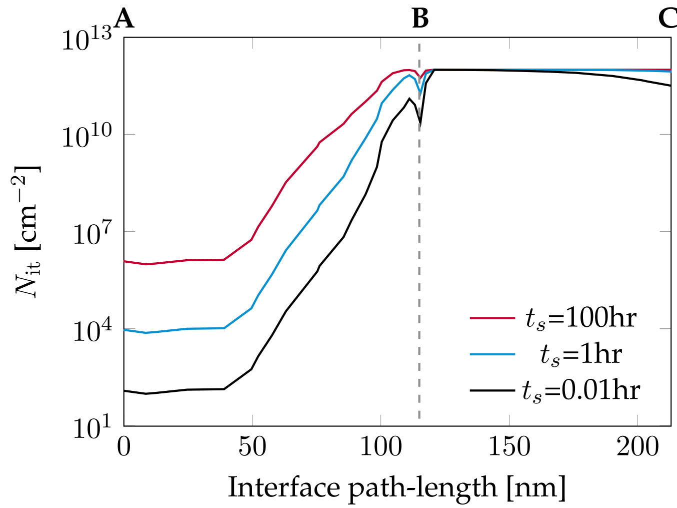

Figure 4.18: Trap densities generated at different stress time steps along the EB spacer oxide interface from node A to C denoted in Fig. 4.15 at $V_{\text{EB}} = 3\,\text{V}$ and $V_{\text{CB}} = 3\,\text{V}$.

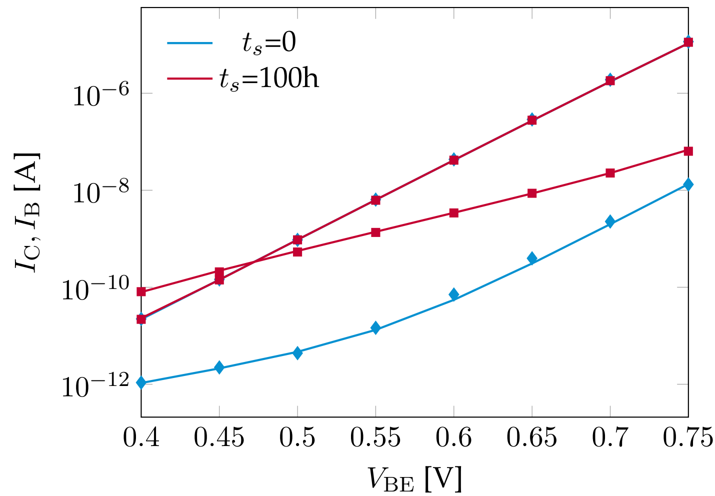

Figure 4.19: Gummel characteristics of the fresh and degraded SiGe HBT after 100 h at $V_{\text{EB}} = 3\,\text{V}$ and $V_{\text{CB}} = 3\,\text{V}$ obtained from simulation (lines) and measurement (symbols).

that our tunneling current has been verified just by a macroscopic data (Fig. 4.14). Therefore, our local BTBT model might miss some microscopic effects of the BTBT process. Fig. 4.20 shows that the highest electric field, which predominantly determines BTBT, is located in the emitter part of the SCR of the EB junction. In a local

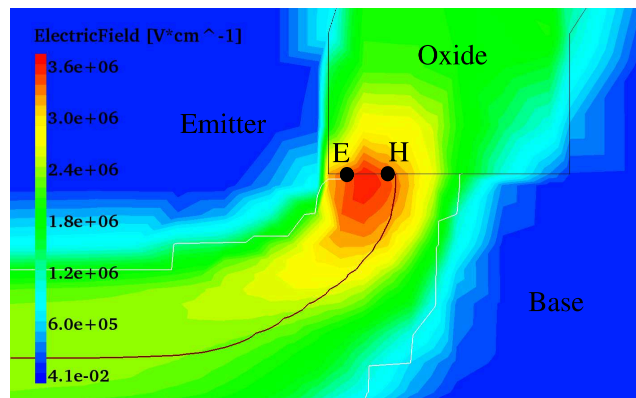

Figure 4.20: Electric field in the SiGe HBT at $V_{\mathrm{EB}} = 3\,\mathrm{V}$ and $V_{\mathrm{CB}} = 3\,\mathrm{V}$. The possible locations of the generated electron (E) and hole (H) due to non-local BTBT have been marked.

BTBT model, the generated electron and hole due to BTBT, are both considered at the same location; therefore, they are both accelerated by the large electric field and gain high energies. However, if a non-local BTBT model is applied, holes are generated in the valence band of SCR in the base region and electrons are generated in the conduction band close to the boundary of the SCR (shown in Fig. 4.20). Therefore, electrons are generated in a position that cannot be accelerated by the high electric field. Consequently, it is expected that by using a non-local BTBT model, we obtain less number of hot electrons and dominance of hot holes [91].

Chapter 5

Summary and future work

This thesis work presented a semi-classical simulation framework for the state-of-the-art toward-terahertz SiGe HBTs. The stationary results of this deterministic simulator, which solves a coupled set of BTEs for electrons and holes based on the SHE method, were validated by comparison to measurement data. A BTE for LO phonons coupled with energy balance equations for the other phonon modes were used to investigate the effect of self-heating in a 2-D SiGe HBT. This electrothermal simulator, which models heat generation accurately and accounts for the thermal conductivity reduction mainly due to Ge content, doping concentration and size effects, showed a negligible effect of hot LO phonons on the collector current and electron II. Moreover, the deterministic and self-consistent solution of the carrier BTEs made it possible to calculate the required parameters for the thermal resistance extraction from the DC characteristics of the device, which can be problematic with stochastic algorithms. It was shown that the junction temperature extracted from the DC characteristics of the device is consistent with the average temperature increase over the EB junction in the investigated HBT, which verifies the experimental procedure for thermal resistance extraction.

In order to obtain a microscopic simulation platform for HCD in bipolar transistors, an energy-driven paradigm relying on the carrier EDF was incorporated into the SHE solver. In this approach, the deterministic solver provides the EDFs of the

carriers impinging on the EB spacer oxide interface up to high energies, which are required for the calculation of the AIs. By investigating the AB AIs along the EB spacer oxide interface, it was shown that HCD in SiGe HBTs under stress conditions near the SOA limit of the device occurs dominantly due to hot holes, and the impact of stress bias conditions on the degradation rate was explained. These results are obtained by a model, which accounts for the dependence of the carriers on energy. Therefore, classical transport models, in which carriers are assumed in thermal equilibrium with the lattice, are unsuited to explain non-equilibrium behavior of hot-carriers. The total bond-breakage rate, calculated by accounting for superposition of the AB and MVE processes for both electrons and holes, was used in a dispersive reaction-limited model to explain the time dependence of the interface trap density and the resulting forward-mode leakage base current. The simulation results for different stress conditions at the common-emitter SOA edge are in a very good agreement with measurement data. As a result, a reaction-limited method with dispersive reaction rates is strongly recommended as the suitable approach to model HCD results in bipolar transistors rather than the commonly used reaction-diffusion model, which is not consistent with the measurement data in the microscopic level.

The results of this work provided a new insight into the microscopic mechanisms of hot-phonon and hot-carrier effects in bipolar transistors. However, it would be beneficial to also solve BTE for acoustic phonons. This topic, which can provide more information regarding the phonon transport, is worth considering for further study. Furthermore, although degradation results based on a local BTBT model could explain the measurement data in the reverse EB bias stress mode, it is expected that the effect of hot electrons has been overestimated. Therefore, to capture all microscopic effects in the reverse EB bias degradation process, a non-local BTBT model has to be implemented in the SHE solver.

Bibliography

[1] D. V. Morgan and R. H. Williams, *Physics and technology of heterojunction devices*. Institution of Electrical Engineers (IET), Series 8, 1991.

[2] G. L. Patton, S. S. Iyer, S. Delage, S. Tiwari, and J. Stork, "Silicon-germanium base heterojunction bipolar transistors by molecular beam epitaxy," *IEEE Electron Device Lett.*, vol. 9, pp. 165–167, Apr. 1988.

[3] B. Heinemann, R. Barth, D. Bolze, J. Drews, G. Fischer, A. Fox, O. Fursenko, T. Grabolla, U. Haak, D. Knoll, *et al.*, "SiGe HBT technology with f_T/f_{max} of 300GHz/500GHz and 2.0 ps CML gate delay," in *International Electron Devices Meeting (IEDM)*, pp. 688–691, Dec. 2010.

[4] C. Jungemann and S.-M. Hong, "Investigation of electronic noise in THz SiGe HBTs by microscopic simulation," in *Bipolar/BiCMOS Circuits and Technology Meeting (BCTM), 2013 IEEE*, pp. 1–8, Oct. 2013.

[5] J. D. Cressler, "Emerging application opportunities for SiGe technology," in *Custom Integrated Circuits Conference, 2008. CICC 2008. IEEE*, pp. 57–64, Sep. 2008.

[6] C. Hu, *Modern semiconductor devices for integrated circuits*. Prentice Hall, 2010.

[7] R. H. Winkler, "Thermal properties of high-power transistors," *IEEE Trans. Electron Devices*, vol. 14, pp. 260–263, May 1967.

[8] B. Heinemann, H. Rücker, R. Barth, F. Bärwolf, J. Drews, G. Fischer, A. Fox, O. Fursenko, T. Grabolla, F. Herzel, *et al.*, "Sige hbt with f_T/f_{max} of 505

GHz/720 GHz," in *Electron Devices Meeting (IEDM), 2016 IEEE International*, pp. 3–1, 2016.

[9] C. Jungemann, T. Grasser, B. Neinhuus, and B. Meinerzhagen, "Failure of moments-based transport models in nanoscale devices near equilibrium," *IEEE Trans. Electron Devices*, vol. 52, pp. 2404–2408, Nov. 2005.

[10] C. Jungemann and B. Meinerzhagen, *Hierarchical device simulation: the Monte-Carlo perspective*. Springer Science & Business Media, 2003.

[11] O. Madelung, *Introduction to solid-state theory*. Berlin: Springer, 1978.

[12] S.-M. Hong, A.-T. Pham, and C. Jungemann, *Deterministic solvers for the Boltzmann transport equation*. Vienna, Austria: Springer, 2011.

[13] C. Jacoboni and P. Lugli, *The Monte Carlo method for semiconductor device simulation*. Vienna: Springer, 1989.

[14] M. L. Cohen and J. R. Chelikowsky, *Electronic structure and optical properties of semiconductors*. Springer New York, 1989.

[15] M. M. Rieger and P. Vogl, "Electronic-band parameters in strained $\mathrm{Si}_{1-x}\mathrm{Ge}_x$ alloys on $\mathrm{Si}_{1-y}\mathrm{Ge}_y$ substrates," *Phys. Rev. B*, vol. 48, pp. 14276–14287, Nov. 1993.

[16] R. Brunetti, C. Jacoboni, F. Nava, L. Reggiani, G. Bosman, and R. Zijlstra, "Diffusion coefficient of electrons in silicon," *J. Appl. Phys.*, vol. 52, pp. 6713–6722, Nov. 1981.

[17] S.-M. Hong and C. Jungemann, "A fully coupled scheme for a Boltzmann-Poisson equation solver based on a spherical harmonics expansion," *J. Comput. Electron.*, vol. 8, pp. 225–241, Oct. 2009.

[18] C. Herring and E. Vogt, "Transport and deformation-potential theory for many-valley semiconductors with anisotropic scattering," *Phys. Rev.*, vol. 101, pp. 944–961, Feb. 1956.

[19] H. Kamrani, D. Jabs, V. d'Alessandro, N. Rinaldi, T. Jacquet, C. Maneux, T. Zimmer, K. Aufinger, and C. Jungemann, "Microscopic hot-carrier degra-

dation modeling of SiGe HBTs under stress conditions close to the SOA limit," *IEEE Trans. Electron Devices*, vol. 64, pp. 923–929, Mar. 2017.

[20] S.-M. Hong, G. Matz, and C. Jungemann, "A deterministic boltzmann equation solver based on a higher order spherical harmonics expansion with full-band effects," *IEEE Trans. Electron Devices*, vol. 57, pp. 2390–2397, Oct. 2010.

[21] F. Schäffler, "High-mobility Si and Ge structures," *Semicond. Sci. Technol.*, vol. 12, p. 1515, Aug. 1997.

[22] D. Klaassen, J. Slotboom, and H. De Graaff, "Unified apparent bandgap narrowing in n-and p-type silicon," *Solid State Electron.*, vol. 35, pp. 125–129, Feb. 1992.

[23] R. J. Hueting, J. W. Slotboom, A. Pruijmboom, W. B. de Boer, C. E. Timmering, and N. E. Cowern, "On the optimization of SiGe-base bipolar transistors," *IEEE Trans. Electron Devices*, vol. 43, pp. 1518–1524, Sep. 1996.

[24] C. Jungemann and B. Meinerzhagen, *Hierarchical device simulation: the Monte-Carlo perspective*. Springer Science & Business Media, 2012.

[25] H. Brooks and C. Herring, "Scattering by ionized impurities in semiconductors," *Phys. Rev.*, vol. 83, pp. 879–887, 1951.

[26] D. M. Caughey and R. E. Thomas, "Carrier mobilities in silicon empirically related to doping and field," *Proc. IEEE*, vol. 55, no. 12, pp. 2192–2193, 1967.

[27] J. Harrison and J. Hauser, "Alloy scattering in ternary III-V compounds," *Phys. Rev. B*, vol. 13, p. 5347, Jun. 1976.

[28] C. Jungemann, S. Keith, F. Bufler, and B. Meinerzhagen, "Effects of band structure and phonon models on hot electron transport in silicon," *Electr. Eng.*, vol. 79, pp. 99–101, Apr. 1996.

[29] G. Hurkx, D. Klaassen, and M. Knuvers, "A new recombination model for device simulation including tunneling," *IEEE Trans. Electron Devices*, vol. 39, pp. 331–338, Feb. 1992.

[30] Synopsys, Inc., Mountain View, CA, *Sentaurus Device User Guide*, Jun. 2015.

[31] K.-H. Kao, A. S. Verhulst, W. G. Vandenberghe, B. Soree, G. Groeseneken, and K. De Meyer, "Direct and indirect band-to-band tunneling in germanium-based TFETs," *IEEE Trans. Electron Devices*, vol. 59, pp. 292–301, Feb. 2012.

[32] C. Jungemann, A. Pham, B. Meinerzhagen, C. Ringhofer, and M. Bollhöfer, "Stable discretization of the Boltzmann equation based on spherical harmonics, box integration, and a maximum entropy dissipation principle," *J. Appl. Phys.*, vol. 100, p. 024502, May 2006.

[33] J. D. Jackson, *Classical Electrodynamics*. New York: John Wiley & Sons, 1975.

[34] R. S. Varga, *Matrix iterative analysis*. Series in Automatic Computation. Prentice-Hall, Englewood Cliffs, New Jersy, 1962.

[35] S.-M. Hong and C. Jungemann, "Inclusion of the Pauli principle in a deterministic Boltzmann equation solver for semiconductor devices," in *Proc. IEEE Int. Conf. Simulation Semiconductor Process. Devices (SISPAD)*, pp. 135–138, Sep. 2010.

[36] S.-M. Hong and C. Jungemann, "Inclusion of the Pauli principle in a deterministic Boltzmann equation solver based on a spherical harmonics expansion," *J. Comput. Electron.*, vol. 9, pp. 153–159, Dec. 2010.

[37] N. Nenadović, V. d'Alessandro, L. La Spina, N. Rinaldi, and L. K. Nanver, "Restabilizing mechanisms after the onset of thermal instability in bipolar transistors," *IEEE Trans. Electron Devices*, vol. 53, pp. 643–653, Apr. 2006.

[38] I. Marano, V. d'Alessandro, and N. Rinaldi, "Analytical modeling and numerical simulations of the thermal behavior of trench-isolated bipolar transistors," *Solid State Electron.*, vol. 53, pp. 297–307, Mar. 2009.

[39] V. d'Alessandro, G. Sasso, N. Rinaldi, and K. Aufinger, "Influence of scaling and emitter layout on the thermal behavior of toward-THz SiGe: C HBTs," *IEEE Trans. Electron Devices*, vol. 61, pp. 3386–3394, Oct. 2014.

[40] E. Pop, S. Sinha, and K. E. Goodson, "Heat generation and transport in nanometer-scale transistors," *Proc. IEEE*, vol. 94, pp. 1587–1601, Aug. 2006.

[41] V. d'Alessandro, A. Magnani, L. Codecasa, N. Rinaldi, and K. Aufinger, "Advanced thermal simulation of SiGe:C HBTs including back-end-of-line," *Microelectronics Reliability*, vol. 67, pp. 38–45, Dec. 2016.

[42] O. Muscato, V. Di Stefano, and C. Milazzo, "An improved hydrodynamic model describing heat generation and transport in submicron silicon devices," *J. Comput. Electron.*, vol. 7, pp. 142–145, Sep. 2008.

[43] E. Pop, "Energy dissipation and transport in nanoscale devices," *Nano Research*, vol. 3, pp. 147–169, Mar. 2010.

[44] M. Zebarjadi, A. Shakouri, and K. Esfarjani, "Thermoelectric transport perpendicular to thin-film heterostructures calculated using the Monte Carlo technique," *Phys. Rev. B*, vol. 74, pp. 195331-1–195331-6, Nov. 2006.

[45] T. Sadi and R. W. Kelsall, "Monte Carlo study of the electrothermal phenomenon in silicon-on-insulator and silicon-germanium-on-insulator metal-oxide field-effect transistors," *J. Appl. Phys.*, vol. 107, pp. 064506-1–064506-9, Mar. 2010.

[46] K. Raleva, D. Vasileska, S. M. Goodnick, and M. Nedjalkov, "Modeling thermal effects in nanodevices," *IEEE Trans. Electron Devices*, vol. 55, pp. 1306–1316, Jun. 2008.

[47] D. Vasileska, K. Raleva, and S. M. Goodnick, "Self-heating effects in nanoscale FD SOI devices: the role of the substrate, boundary conditions at various interfaces, and the dielectric material type for the box," *IEEE Trans. Electron Devices*, vol. 56, pp. 3064–3071, Dec. 2009.

[48] T. Thu Trang Nghiêm, J. Saint-Martin, and P. Dollfus, "New insights into self-heating in double-gate transistors by solving boltzmann transport equations," *J. Appl. Phys.*, vol. 116, pp. 074514-1–074514-9, Aug. 2014.

[49] A. Gnudi, D. Ventura, G. Baccarani, and F. Odeh, "Two-dimensional MOSFET simulation by means of a multidimensional spherical harmonics expansion of the Boltzmann transport equation," *Solid State Electron.*, vol. 36, pp. 575 – 581, Apr. 1993.

[50] M. Ramonas and C. Jungemann, "A deterministic approach to noise in a non-equilibrium electron-phonon system based on the Boltzmann equation," *J. Comput. Electron.*, vol. 14, pp. 43–50, Mar. 2015.

[51] Z. Wang and N. Mingo, "Diameter dependence of SiGe nanowire thermal conductivity," *Appl. Phys. Lett.*, vol. 97, pp. 101903-1–101903-3, Sep. 2010.

[52] R. Cheaito, J. C. Duda, T. E. Beechem, K. Hattar, J. F. Ihlefeld, D. L. Medlin, M. A. Rodriguez, M. J. Campion, E. S. Piekos, and P. E. Hopkins, "Experimental investigation of size effects on the thermal conductivity of silicon-germanium alloy thin films," *Phys. Rev. Lett.*, vol. 109, pp. 195901-1–195901-5, Nov. 2012.

[53] J. Coster and H. B. Hart, "A simple proof of the addition theorem for spherical harmonics," *Am. J. Phys.*, vol. 59, pp. 371–373, Apr. 1991.

[54] J. Lai and A. Majumdar, "Concurrent thermal and electrical modeling of sub-micrometer silicon devices," *J. Appl. Phys.*, vol. 79, pp. 7353–7361, May 1996.

[55] T. Thu Trang Nghiêm, J. Saint-Martin, and P. Dollfus, "Electro-thermal simulation based on coupled boltzmann transport equations for electrons and phonons," *J. Comput. Electron.*, vol. 15, pp. 3–15, Mar. 2016.

[56] D. Vasileska, A. Hossain, K. Raleva, and S. Goodnick, "The role of the source and drain contacts on self-heating effect in nanowire transistors," *J. Comput. Electron.*, vol. 9, pp. 180–186, Dec. 2010.

[57] V. Palankovski and R. Quay, *Analysis and simulation of heterostructure devices*. Vienna, Austria: Springer-Verlag, 2004.

[58] Y. Lee and G. S. Hwang, "Mechanism of thermal conductivity suppression in doped silicon studied with nonequilibrium molecular dynamics," *Physical Review B*, vol. 86, pp. 075202-1–075202-6, Aug. 2012.

[59] D. Vasileska, K. Raleva, and S. M. Goodnick, "Electrothermal studies of FD SOI devices that utilize a new theoretical model for the temperature and thickness dependence of the thermal conductivity," *IEEE Trans. Electron Devices*, vol. 57, pp. 726–728, Mar. 2010.

[60] V. d'Alessandro and N. Rinaldi, "A critical review of thermal models for electro-thermal simulation," *Solid State Electron.*, vol. 46, pp. 487–496, Apr. 2002.

[61] H. Kamrani, T. Kochubey, D. Jabs, and C. Jungemann, "Electrothermal simulation of SiGe HBTs and investigation of experimental extraction methods for junction temperature," in *Proc. IEEE Int. Conf. Simulation Semiconductor Process. Devices (SISPAD)*, pp. 108–111, Sep. 2015.

[62] N. Nenadovic, V. d'Alessandro, L. Nanver, N. Rinaldi, H. Schellevis, and J. Slotboom, "Analytical formulation and electrical measurements of self-heating in silicon BJT's," in *Bipolar/BiCMOS Circuits and Technology Meeting, 2002. Proceedings of the 2002*, pp. 24–27, Oct. 2002.

[63] M. Schröter, T. Rosenbaum, P. Chevalier, B. Heinemann, S. P. Voinigescu, E. Preisler, J. Böck, and A. Mukherjee, "SiGe HBT technology: Future trends and TCAD-based roadmap," *Proc. IEEE*, vol. PP, pp. 1–19, Jan. 2016.

[64] T. Grasser, *Hot Carrier Degradation in Semiconductor Devices*. Springer.

[65] G. G. Fischer and G. Sasso, "Ageing and thermal recovery of advanced SiGe heterojunction bipolar transistors under long-term mixed-mode and reverse stress conditions," *Microelectron. Reliab.*, vol. 55, pp. 498–507, Mar. 2015.

[66] J.-S. Rieh, K. M. Watson, F. Guarin, Z. Yang, P.-C. Wang, A. J. Joseph, G. Freeman, and S. Subbanna, "Reliability of high-speed SiGe heterojunction bipolar transistors under very high forward current density," *IEEE Trans. Device Mater. Rel*, vol. 3, pp. 31–38, Jun. 2003.

[67] U. Gogineni, J. D. Cressler, G. Niu, and D. L. Harame, "Hot electron and hot hole degradation of UHV/CVD SiGe HBT's," *IEEE Trans. Electron Devices*, vol. 47, pp. 1440–1448, Jul. 2000.

[68] G. Zhang, J. D. Cressler, G. Niu, and A. J. Joseph, "A new "mixed-mode" reliability degradation mechanism in advanced Si and SiGe bipolar transistors," *IEEE Trans. Electron Devices*, vol. 49, pp. 2151–2156, Dec. 2002.

[69] J. D. Cressler, "Emerging SiGe HBT reliability issues for mixed-signal circuit applications," *IEEE Trans. Device Mater. Rel*, vol. 4, pp. 222–236, Jun. 2004.

[70] H. Kamrani, D. Jabs, V. d'Alessandro, N. Rinaldi, and C. Jungemann, "Physics-based hot-carrier degradation model for SiGe HBTs," in *Proc. Int. Conf. Simulation Semiconductor Process. Devices (SISPAD)*, pp. 341–344, 2016.

[71] T. Grasser, K. Rott, H. Reisinger, M. Waltl, F. Schanovsky, and B. Kaczer, "NBTI in nanoscale MOSFETs-the ultimate modeling benchmark," *IEEE Trans. Electron Devices*, vol. 61, pp. 3586–3593, Nov. 2014.

[72] C. Zhu, Q. Liang, R. A. Al-Huq, J. D. Cressler, Y. Lu, T. Chen, A. J. Joseph, and G. Niu, "Damage mechanisms in impact-ionization-induced mixed-mode reliability degradation of SiGe HBTs," *IEEE Trans. Device Mater. Rel*, vol. 5, no. 1, pp. 142–149, 2005.

[73] P. Cheng, C. M. Grens, and J. D. Cressler, "Reliability of SiGe HBTs for power amplifiers-Part II: Underlying physics and damage modeling," *IEEE Trans. Electron Devices*, vol. 9, pp. 440–448, Sep. 2009.

[74] K. A. Moen, P. S. Chakraborty, U. S. Raghunathan, J. D. Cressler, and H. Yasuda, "Predictive physics-based TCAD modeling of the mixed-mode degradation mechanism in SiGe HBTs," *IEEE Trans. Electron Devices*, vol. 59, pp. 2895–2901, Nov. 2012.

[75] B. R. Wier, K. Green, J. Kim, D. T. Zweidinger, and J. D. Cressler, "A physics-based circuit aging model for mixed-mode degradation in SiGe HBTs," *IEEE Trans. Electron Devices*, vol. 63, pp. 2987–2993, Aug. 2016.

[76] D. J. DiMaria and J. W. Stasiak, "Trap creation in silicon dioxide produced by hot electrons," *J. Appl. Phys.*, vol. 65, pp. 2342–2356, Mar. 1989.

[77] D. J. DiMaria and J. H. Stathis, "Anode hole injection, defect generation, and breakdown in ultrathin silicon dioxide films," *J. Appl. Phys.*, vol. 89, pp. 5015–5024, May 2001.

[78] I. Starkov, H. Enichlmair, S. Tyaginov, and T. Grasser, "Charge-pumping extraction techniques for hot-carrier induced interface and oxide trap spatial distributions in MOSFETs," in *Physical and Failure Analysis of Integrated Circuits (IPFA)*, pp. 1–6, Jul. 2012.

[79] I. Starkov, S. Tyaginov, H. Enichlmair, J. Cervenka, C. Jungemann, S. Carniello, J. M. Park, H. Ceric, and T. Grasser, "Hot-carrier degradation caused interface state profile-simulation versus experiment," *J. Vac. Sci. Technol., B*, vol. 29, pp. 01AB091–01AB098, Jan. 2011.

[80] M. Bina, S. Tyaginov, J. Franco, K. Rupp, Y. Wimmer, D. Osintsev, B. Kaczer, and T. Grasser, "Predictive hot-carrier modeling of n-channel MOSFETs," *IEEE Trans. Electron Devices*, vol. 61, pp. 3103–3110, Sep. 2014.

[81] P. Sharma, S. Tyaginov, Y. Wimmer, F. Rudolf, K. Rupp, M. Bina, H. Enichlmair, J.-M. Park, R. Minixhofer, H. Ceric, *et al.*, "Modeling of hot-carrier degradation in nLDMOS devices: different approaches to the solution of the Boltzmann transport equation," *IEEE Trans. Electron Devices*, vol. 62, pp. 1811–1818, Jun. 2015.

[82] S. Tyaginov, M. Jech, J. Franco, P. Sharma, B. Kaczer, and T. Grasser, "Understanding and modeling the temperature behavior of hot-carrier degradation in SiON n-MOSFETs," *IEEE Electron Device Lett.*, vol. 37, pp. 84–87, Jan. 2016.

[83] K. Stokbro, C. Thirstrup, M. Sakurai, U. Quaade, B. Y. Hu, F. Perez-Murano, and F. Grey, "STM-induced hydrogen desorption via a hole resonance," *Phys. Rev. Lett.*, vol. 80, pp. 2618–2621, Mar. 1998.

[84] K. O. Jeppson and C. M. Svensson, "Negative bias stress of MOS devices at high electric fields and degradation of MNOS devices," *J. Appl. Phys.*, vol. 48, pp. 2004–2014, May 1977.

[85] V. Huard, M. Denais, F. Perrier, N. Revil, C. Parthasarathy, A. Bravaix, and E. Vincent, "A thorough investigation of MOSFETs NBTI degradation," *Microelectron. Reliab.*, vol. 45, pp. 83–98, Jan. 2005.

[86] P. Chevalier, T. F. Meister, B. Heinemann, S. V. Huylenbroeck, W. Liebl, A. Fox, A. Sibaja-Hernandez, and A. Chantre, "Towards THz SiGe HBTs," in *Proc. IEEE Bipolar/BiCMOS Circuits and Technology Meeting (BCTM)*, pp. 57–65, Oct. 2011.

[87] T. Vanhoucke, G. Hurkx, D. Panko, R. Campos, A. Piontek, P. Palestri, and L. Selmi, "Physical description of the mixed-mode degradation mechanism for

high performance bipolar transistors," in *Proc. IEEE Bipolar/BiCMOS Circuits Technol. Meeting*, pp. 25–28, 2006.

[88] A. Stesmans, "Revision of H2 passivation of pb interface defects in standard (111) Si/SiO2," *Appl. Phys. Lett.*, vol. 68, pp. 2723–2725, Feb. 1996.

[89] G. Pobegen, S. Tyaginov, M. Nelhiebel, and T. Grasser, "Observation of normally distributed energies for interface trap recovery after hot-carrier degradation," *IEEE Electron Device Lett.*, vol. 34, pp. 939–941, Aug. 2013.

[90] H. Kufluoglu and M. A. Alam, "A generalized reaction-diffusion model with explicit H-H_2 dynamics for negative-bias temperature-instability (NBTI) degradation," *IEEE Trans. Electron Devices*, vol. 54, pp. 1101–1107, May 2007.

[91] A. Neugroschel, C.-T. Sah, and M. Carroll, "Degradation of bipolar transistor current gain by hot holes during reverse emitter-base bias stress," *IEEE Trans. Electron Devices*, vol. 43, pp. 1286–1290, Aug. 1996.